INVESTIGATION OF SHEAR BAND MECHANISM IN REINFORCED SOIL RETAINING WALL USING PULLOUT TESTS

by

Şevket İmamoğlu

B.S., Civil Engineering, Boğaziçi University, 2012

Submitted to the Institute for Graduate Studies in
Science and Engineering in partial fulfillment of
the requirements for the degree of
Master of Science

Graduate Program in Civil Engineering

Boğaziçi University

2017

ACKNOWLEDGEMENTS

I would like to express my sincere gratitude to my thesis supervisor, Prof. Erol Güler for his guidance and support throughout the preparation of this thesis.

I would like to thank to Prof. Jorge G. Zornberg for his encouragement and support during the research, especially giving me opportunity to run experiments at the University of Texas at Austin. Without Zornberg's encouragement, I could not have conducted the research and run my experiments.

I would also like to acknowledge my friends Amr Morsy, Jose Martinez, Xin Peng, Calvin Blake and Federico Castro for their extensive support in running the experiments.

Special thanks to my manager Özger İnal and my company ENKA for their understanding during my study.

Last but not least, I would like to express my greatest gratitude to my parents for their endless support my entire life.

ABSTRACT

INVESTIGATION OF SHEAR BAND MECHANISM IN REINFORCED SOIL RETAINING WALL USING PULLOUT TESTS

Geosynthetic Reinforced Soil in essence is the use of polymeric reinforcements into soil body to strengthen mechanical properties of the soil. Innovative applications of geosynthetic reinforced soil have significantly increased in last decades. Geosynthetic Reinforced Soil-Integrated Bridge System (GRS-IBS) is a new concept integrating roadway approaching slabs of the bridge and superstructure on geosynthetic reinforced soil. Design and construction guidelines are being adapted to recent innovative concepts. In order to propose a complete guideline, serviceability and failure mechanism should be thoroughly. Shear bands are localized shear deformations causing the failure of reinforced soil. In this research, pullout test is selected to observe shear band mechanism under different parameters. A modified small pullout test setup were developed which allows direct displacement measurements of the particles with image analysis, and were utilized to observe shear band mechanism. Digital Image Correlation technique has been utilized to determine displacement of soil particles. Tests were performed under different overburden pressure, average soil particle size and reinforcement geometry. The shear band mechanism observed with the modified setup and measurement technique is consistent with the literature, confirming the suitability of the applied testing method.

ÖZET

DONATILI ZEMİN İSTİNAT DUVARLARINDA KAYMA BANTI MEKANİZMASININ ÇEKME TESTLERİ KULLANILARAK İNCELENMESİ

Geosentetik Donatılı Zeminler polimer donatıların zeminin mekanik özelliklerini güçlendirme amacıyla zemn kütlesinde kullanımıdır. Geosentetik donatılı zeminlerin yenilikçi uygulamaları son yıllarda muazzam miktarda artış göstermiştir. Geosentetik Donatılı Zemin-Entegre Köprü Sistemi köprü yaklaşım yol döşemesi ile geosentetik donate üzerine oturan üstyapıyı entegre eden yeni bir konsepttir. Yakın zamanda yapılan bu yenilikçi uygulamalar, tasarım ve inşaat şartnamelerine adapte edilmektedir. Eksiksiz bir şartname sunabilmek için kullanılabilirlik ve yıkım mekanizmaları tamamen anlaşılmış olmalıdır. Kayma bantları donatılı zeminin yıkımına sebep olan lokalize kayma deformasyonlarıdır. Bu araştırmada, farklı parametreler altında kayma bandı mekanizmasını gözlemlemek için çekme deneyi seçilmiştir. Görüntü analizi yöntemi ile deplasman ölçümü yapmaya olanak sağlayacak şekilde modifiye edilmiş küçük çekme deney düzeneği geliştirilmiş ve kayma bandı mekanizması gözlemi için kullanılmıştır. Dijital Görüntü Korealsyonu tekniği ile zemin tanelerinin deplasman ölçümleri yapılmıştır. Testler farklı örtü basınçları, ortalama zemin tane büyüklüğü ve donatı geometrisi altında yapılmıştır. Önerilen düzenek ve ölçüm teknikleri altında, kayma banda mekanizması gözlemleri literatürle uyumludur ve bu gözlemler uygulanan test metodunun elverişliliğinini doğrulamaktadır.

TABLE OF CONTENTS

LIST OF FIGURES

LIST OF TABLES

LIST OF SYMBOLS

B	Thickness of bearing member
c	Cohesion
d_{50}	Average particle size of the soil
F	Resultant Thrust
F_o	Front pullout force
ft	Feet
H	Height of the Wall
K_a	Active Earth pressure coefficient
kN	Kilonewton
K_o	At rest Earth pressure coefficient
K_p	Passive Earth pressure coefficient
kPA	Kilopascal
K_{SGI}	Coefficient of Soil-Geosynthetic Interaction
L	Reinforcement length
lb	Pound
L_E	Passive reinforcement length
L_O	Reinforcement overwrapped length
L_R	Active reinforcement length
m	Meter
mm	Millimeter
P_a	Active Earth Pressure
P_p	Passive Earth Pressure
P_R	Maximum pullout resistance of geogrid
P_{RB}	Bearing resistance of geogrid
P_{RS}	Frictional resistance of geogrid
S	Spacing of geogrid bearing members
s	Second
S_v	Spacing of reinforcement

t	Thickness of shear band
W	Weight
z	Depth from ground surface
α_A	Inclination angle of the critical failure surface
α_B	Frontal area of geogrid
β	Inclination angle of the backfill
γ	Unit Weight
δ	Soil-Wall Interface Friction Angle
ΔL_a	Horizontal displacement (tilt) of the wall due to active earth pressure
ΔL_p	Horizontal displacement (tilt) of the wall due to passive earth pressure
ε	Strain
θ	Wall batter angle
μ	Coefficient of friction
σ	Effective Normal Stress
σ_h	Horizontal Normal Stress
σ_n	Normal effective stress
σ_s	Solid geogrid surface area fraction
σ_v	Vertical Normal Stress
τ_f	Shear Strength of Soil
ϕ	Internal Friction Angle of the Soil

LIST OF ACRONYMS/ABBREVIATIONS

AASHTO	The American Association of State Highway and Transportation Officials
ASTM	American Society for Testing Materials
CPE	Chlorinated Polyethylene
CSPE	Chlorosulfonated Polyethylene
DIC	Digital Image Correlation
EPS	Expanded Polystyrene
ERS	Earth Retaining Structure
FHWA	the U.S. Department of Transportation - Federal Highway Administration
GDP	Gross Domestic Product
GRS	Geosynthetic Reinforced Soil
HDPE	High Density Polyethylene
IBS	Integrated Bridge System
LLDPE	Linear Low Density Polyethylene
LVDT	Linear Variable Differential Transformers
MDPE	Medium Density Polyethylene
OECD	Organisation for Economic Co-operation and Development
PA	Polyamide
PE	Polyester
PET	Polyethylene Terephthalate
PP	Polypropylene
PVC	Polyvinyl Chloride
SCDOT	South Carolina Department of Transportation
USCS	Unified Soil Classification System
UV	Ultraviolet
VLDPE	Very Low Density Polyethylene

1. INTRODUCTION

1.1. General

Civil engineering applications are based on economically and technically efficient design concepts. Land transportation is the most common means of connecting people and nations. Investments on land transportation infrastructure constitutes big portion of nations' budgets, and bridges comprise crucial parts of land transportation systems. Table 1.1 shows the percentage of infrastructure investment on land transportation over Gross Domestic Product (GDP) of countries in 2010 through 2013.

Table 1.1. Infrastructure Investment over GDP% (OECD, 2016).

	2010	2011	2012	2013
Australia	1.5	1.8	1.9	1.6
Canada	1.3	1.2	1.1	1
Germany	0.6	0.6	0.6	0.6
India	0.9	0.8	0.8	0.8
Italy	0.5	0.5	0.5	0.5
Japan	1.1	1.1	1.1	1.1
Mexico	0.6	0.5	0.5	0.5
Turkey	1.3	1.2	1	1.2
United Kingdom	0.7	0.6	0.6	0.6
United States	0.6	0.6	0.6	0.6

Construction time and cost of bridges are significantly higher than the construction of motorways or railroads per unit area. Engineers work on innovative concepts of bridges which lead to more efficient construction methods.

French engineer Henry Vidal introduced Reinforced Earth concept in 1960s. Metal reinforcements extended from facing into the backfill soil composed reinforced

earth mass. This reinforcement concept is called Mechanically Stabilized Earth (MSE) walls and lead to advancements through geosynthetic reinforcements.

Geosynthetics are polymeric materials that can be used as reinforcements, especially in mechanically stabilized earth walls. Over the last 5 decades applications of geosynthetics in geotechnical fields have been widening extensively. Instead of conventional methods, use of innovative solutions such as geosynthetic reinforcement has contributed to both designers and contractors.

Construction of abutment of conventional bridges has following disadvantages (Tatsuoka *et al.*, 2009) which are illustrated in following Figure 1.1

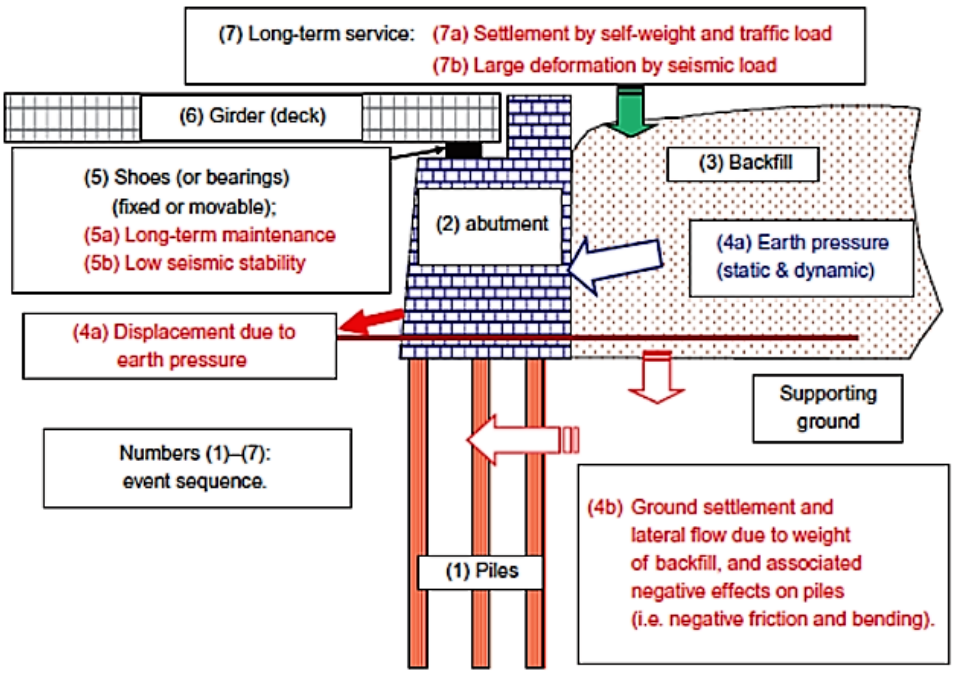

Figure 1.1. Technical Problems with Conventional Bridge Abutments (Tatsuoka *et al.*, 2009).

- Earth pressure developed at the backfill and moment at the bottom corner of the abutment requires massive abutment foundation and piling unless the ground is very strong. In case of soft ground conditions large number of piles is required.
- Construction and maintenance of elastomeric bearings are costly and comprises the weak part of the entire bridge system.

- Differential settlement between the girder (beam) and approaching slab is very likely to be formed.
- Seismic behavior of abutment and the backfill would be weak and different when subject to seismic loads. Therefore, a bump is expected to be formed behind the abutment in case of major earthquake.
- Unreinforced backfill of the abutment has very low resistance against flooding.

Geosynthetic Reinforced Soil-Integrated Bridge System (GRS-IBS) is a new concept that integrates bridge roadway approaching slabs and superstructure on geosynthetic - reinforced fill (Adams *et al.*, 2011). GRS-IBS offers an alternative technique to bridge abutments to reduce both cost and time of bridge construction. It also reduces the differential settlement problem between the bridge superstructures and approaching road slabs. Application of new construction techniques and new materials brings up new challenges that require associated research. Innovative construction and design methodologies should be adopted into guidelines. To do so, serviceability and failure mechanisms of proposed systems should be completely understood.

One of the failure mechanisms observed in geosynthetic reinforced soil is the propagation of shear strains through localized shear deformations in the soil body, in other words shear bands. Extensive researches have been carried out to derive shear band thickness theoretically and experiments were setup to measure shear band thickness.

Most of the studies were focused on the behavior of the unreinforced soil. So far in the literature there is not standardized measurement technique for shear band formation in the reinforced soil. Complete understanding of formation and propagation mechanisms of shear bands are extremely important to propose safe and economic design and construction guidelines for geosynthetic reinforced soil.

This research's main objective is to have a better understanding of the shear band mechanism, especially for determination of reinforcement spacing, and to propose a test configuration that could investigate shear bands in reinforced soil under varying main

parameters: type of geosynthetics, type of backfill soil, and confining pressure.

All tests in this research were conducted at geotechnical laboratory of the University of Texas at Austin. The small-pull out test set-up at the University of Texas at Austin was modified in order to make necessary measurements as per the objective of this research.

This research study is summarized in five chapters:

- Chapter 1: Introduction, which explains the motivation and objective of the study.
- Chapter 2: Literature review, which summarizes technical literature focused on the geogrid-soil interaction and previous studies conducted on observation and quantification of shear band mechanism. In literature review Digital Image Correlation is also explained briefly since its one of the main evaluation tools that is used in this research to process the data.
- Chapter 3: Methodology, which provides a detailed description of the configuration of experimental setup and techniques to evaluate the results.
- Chapter 4: Results and discussions, which includes pullout test results and image analysis and discussions on the results.
- Chapter 5: Conclusion, which briefly summarizes the results and come up with the suggestions for further studies.

2. LITERATURE REVIEW

2.1. Geosynthetics

ASTM D4439 defines geosynthetics as planar products manufactured from polymeric material which are used with soil, rock, or other geotechnical engineering material as an integral part of a man-made project, structure, or system. In other words geosynthetics are synthetic polymeric materials that are specifically manufactured to be used in geotechnical and geoenvironmental applications

Geosynthetics are composed of polymeric chains which are macromolecular structures having specific chemical configuration. Most common polymers used in manufacturing geosynthetics are polyethylene (PE), polypropylene (PP), polyvinyl chloride (PVC), polyester (PE), polyamide (PA), polystyrene (PS). There are several types of geosynthetic products depending on the type of the polymers and manufacturing technique used. Most common types of geosynthetics are: geotextile, geogrids, geomembranes, geocomposites, geonets, geocells, geofoams, geopipes, geosynthetic clay liners. Below Figure 2.1 shows several types of geosynthetic products.

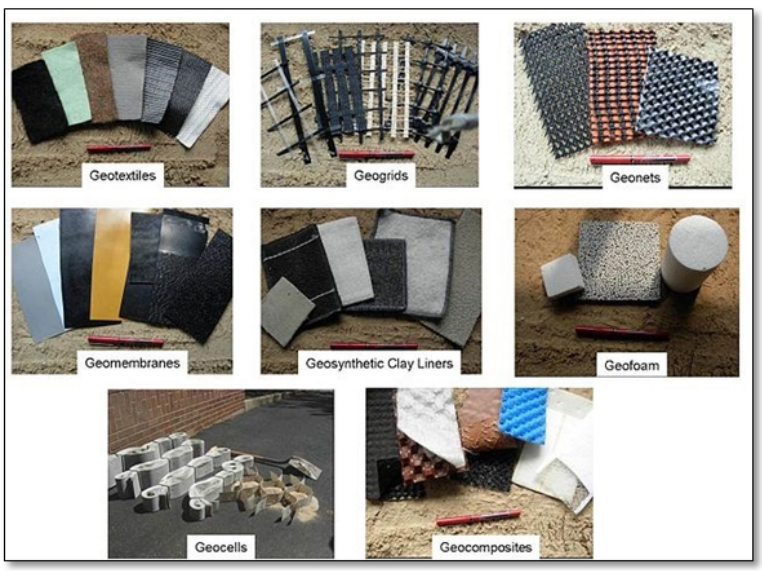

Figure 2.1. Geosynthetic Products (courtesy of Wikipedia).

Geotextiles are planer form polymeric products that are classified as woven and non-woven. Woven geotextiles are manufactured by weaving of yarns, whereas non-woven geotextiles are manufactured by bonding of fibers through needle punching, chemical binding or other methods. Geogrids are grid form polymeric products having that integrally connected at the junctions through extrusion, bonding or interlacing. Tensile resisting elements of geogrids are called ribs. Uniaxial geogrids have higher tensile strength in longitudinal direction that transverse direction whereas biaxial geogrids have uniform tensile strength in both directions and triaxial geogrids have uniform tensile strength in all directions. Geomembranes are planar geosynthetic products having low permeability and mainly used as barriers. Common polymers used for manufacturing are summarized in Table 2.3 and manufacturing process is illustrated in Figure 2.2.

Table 2.1. Geosynthetics and Polymers for Their Manufacture (Shukla and Yin, 2006).

Geosynthetics	Polymers used for manufacturing
Geotextiles	PP, PET, PE, PA
Geogrids	PET, PP, HDPE
Geonets	MDPE, HDPE
Geomembranes	HDPE, LLDPE, VLDPE, PVC, CPE, CSPE, PP
Geofoams	EPS
Geopipes	HDPE, PVC, PP

Pure polymers are not suitable for geosynthetics production; therefore primary resins are formulated with additives or agents such as:

- Catalysts to increase the speed of polymerization,
- Phosphatic compounds to reduce thermal degradation during processing the granular in the molten stage,
- Special stabilization to increase UV resistance,
- Pigments to color the molecular.

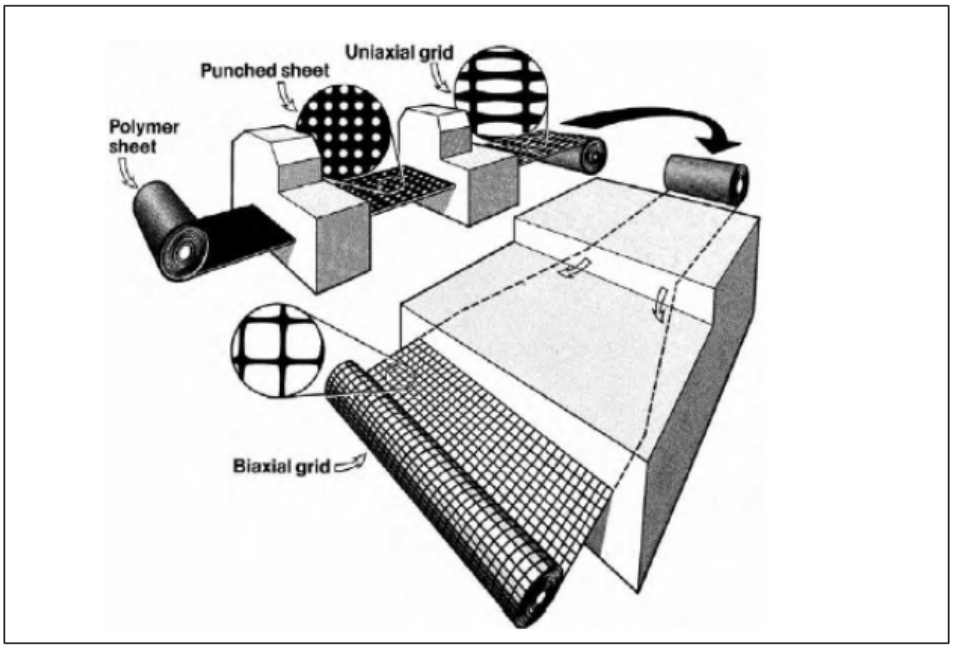

Figure 2.2. Geogrid Manufacturing Process, Fundamentals of Geosynthetic Engineering (courtesy of Netlon Limited).

Geosynthetics have five main functions: separation, filtration, drainage, reinforcement and containment. Function and type of geosynthetics are tabulated in Table 2.2.

Table 2.2. Main Function vs Type of Geosynthetic (Koerner, 2012).

Type of Geosynthetic	Primary Function				
	Separation	Reinforcement	Filtration	Drainage	Containment
Geotextile	X	X	X	X	
Geogrid		X			
Geonet				X	
Geomembrane					X
Geosynthetic Clay Liner					X
Geofoam	X				
Geocomposite	X	X	X	X	X

Geosynthetics are engineered products that are being used in various parts of construction industry, mainly for the purpose of reinforcing the soil. They are most effectively used to overcome engineering challenged in transportation, hydraulics, geo-environmental, mining and geotechnical applications. Since the first application of geosynthetic products in the construction industry, extensive research has been carried out in order to better understand the mechanism of geosynthetics-soil behavior the and to improve the use of geosynthetics in various related fields. Historical development of geosynthetics is summarized in the below Table 2.4:

Table 2.3. Historical Developments of Geosynthetics (Shukla and Yin, 2005).

Decades	Developments
Early decades	The first use of fabrics in reinforcing roads was attempted by the South Carolina Highway Department in 1926 (Beckham and Mills, 1935). Polymers which form the bulk of geosynthetics did not come into commercial production until thirty years later starting with polyvinyl chloride (PVC) in 1933, low density polyethylene (LDPE) and polyamide (PA) (a.k.a. nylon) in 1939, expanded polystyrene (EPS) in 1950, polyester (PET) in 1953, and high density polyethylene (HDPE) and polypropylene (PP) in 1955 (Hall, 1981).The US Bureau of Reclamation has been using geomembranes in water conveyance canals since the 1950s (Staff, 1984)
Late 1950s	A range of fabrics was manufactured for use as separation and filter layers between 1950s granular fills and weak subsoils. Woven fabrics (nowadays called geotextiles) played critical filtration functions in coastal projects in The Netherlands and in the USA.
1960s	Rhone-Poulenc Textiles in France began working with nonwoven needle-punched geotextiles for quite different applications. Geotextiles found a role as beds for highway and railway track support systems. Chlorosulfonated polyethylene (CSPE) was developed around 1965.

Table 2.4. Historical Developments of Geosynthetics (Shukla and Yin, 2005).

Decades	Developments
1970s	The first geotextile used in a dam, in 1970, was a needle-punched nonwoven geotextile used as a filter for the aggregate downstream drain in the Valcross Dam (17 m high), France (Giroud, 1992). Geotextiles were incorporated as reinforcement in retaining walls, steep slopes, etc. The beginning of the ongoing process of standards development started with the formation of the ASTM D-13-18 joint committee on geosynthetics and the formation of industry task forces. The first samples of Tensar grid were made in the Blackburn laboratories of Netlon Ltd, UK, in July 1978.The first conference on geosynthetics was held in Paris in 1977.The geofoam was originally applied as a lightweight fill in Norway in 1972.
1980s	The beginning of the use of geosynthetics occurred in the construction of safe containment of environmentally hazardous wastes. Soil confinement systems based on cellular geotextile nets were first developed and evaluated in France during 1980. Netlon developed a similar concept, but on a larger scale, with the introduction of the Tensar Geocell Mattress in 1982. The first known environmental application of geonet was in 1984 for leak detection in a double-lined hazardous liquid-waste impoundment in Hopewell,Virginia. Koerner and Welsh wrote the first book on geosynthetics in 1980. The International Geosynthetics Society was established in 1983.The first volume of international journal entitled Geotextiles and Geomembranes was published in 1984.
1990s	Many standards on geosynthetics were published by the American Society of Testing Materials (ASTM), USA; the International Organization for Standardization

Development of geosynthetics materials as reinforcement for earth structures is still progressing and improvements are being made in the way they are designed and constructed. The construction technique and flexibility of reinforced soil structures make the technology very attractive. According to independent researches' forecast on geosynthetics global demand; geosynthetics global market is expected to grow at annual growth rate of 10-11%.

Geosynthetic have many advantages compared to conventional methods, including but not limited to:

- Easiness of transportation,
- Easiness of installation,
- Speed of construction,
- Economical & design flexibility,
- Aesthetics & environment friendly.

2.2. Soil Reinforcement

There have always been difficulties to handle with soils on earth. People throughout the history developed different techniques to reinforce soil in order the construct the structures one. Soil could bare high compressive loads but tensile strength of soil is very low or negligible in most cases. Purpose of reinforcing soil is to increase the tensile strength and shear resistance of the soil. Terzaghi (1939) stated that "In engineering practice, difficulties with soils are almost exclusively due not to the soils themselves but to the water contained in their voids. On a planet without any water there would be no need for soil mechanics". Ziggurats are the first know applications of the reinforced soil concept in the world, which can be considered as fiber reinforced soil bricks.

"Mark Twain said, The ancients have stolen all our best ideas. Reinforced soil technology is not modern. The ancients used native material such as straw, tree branches, and plant material to reinforce the earth. The reinforcement provides tensile resistance to soil that is weak in tension but relatively strong in compression and shear. Through soil reinforcement interface bonding, the reinforcement restrains lateral deformation of the surrounding soil, increases its confinement, reduces its tendency for dilation, and consequently, increases the stiffness and strength of the soil mass. In ancient Babylonia, the technology was used to construct the Aqar Quf ziggurat in Iraq around 1440 B.C. The stepped pyramid was built using compacted layers of plant material and soil blocks. The Great Wall of China also used reinforced earth to construct some sections. The fact that these structures are still visible today is a tribute to the

durability of reinforced soil technology (Adams *et al.*, 2011)".

Soil reinforcements may be of several types such as anchors, geosynthetics and metallic strips. Performance of reinforced soil mass is determined by the composition, geometry, stiffness of the reinforcement and characteristics of the soil (particle size, grading etc.). Typical soil reinforcement mechanism illustrated in Figure 2.3.

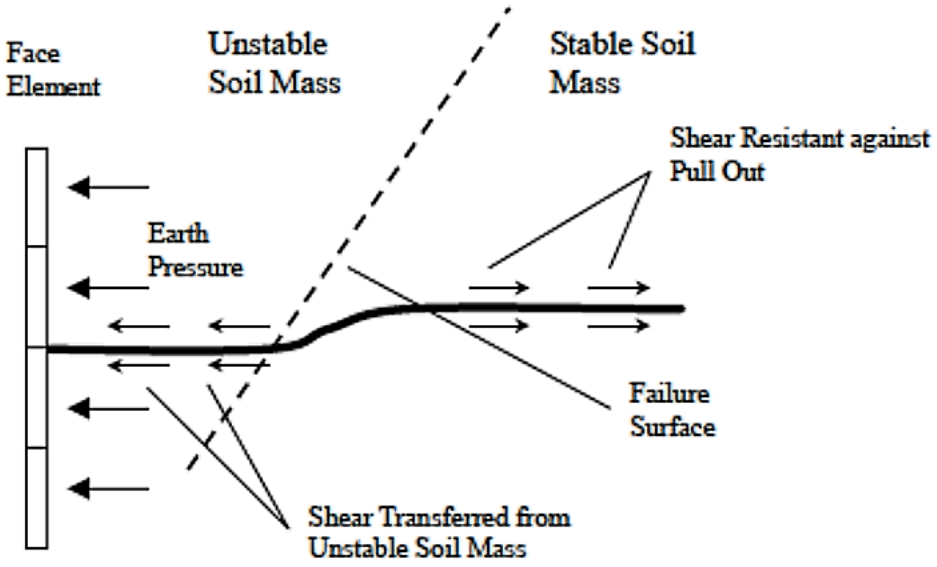

Figure 2.3. Soil Reinforcement Mechanism (Hausmann, 1990).

Design of earth retaining structures is considered in two limit states: serviceability limit state and ultimate limit state. There are several design guidelines being used in the practice, some of which are:

- FHWA-NHI-10-024 (the U.S.A.),
- EN 1997-1:2004 (Europe),
- Nordic Guidelines for Reinforced Soils and Fills 2004 (Scandinavia),
- BS 8006-1:2010 (the U.K.),
- EBGEO 2010 (Germany),
- CUR 2016 (the Netherlands),
- ASIRI 2012 (France),
- Liikennevirasto 2012 (Finland),

- IRC:SP:102-2014 (India),
- AS 4678-2002 (Australia).

Ultimate limit states are associated with collapse or other similar forms of structural failure. Margins of safety, against attaining the limit state considered are provided by the use of partial material factors, partial load factors and partial resistance factors. Serviceability limit sates are attained if the magnitudes of deformation occurring within the design life exceed prescribed limits or if the serviceability of the structures is otherwise impaired (BS 8006-1:2010).

As a minimum the following limit states shall be considered for all types of retaining structure (EN 1997-1:2004):

- Loss of overall stability;
- Failure of a structural element such as a wall, anchorage, wale or strut or failure of the connection between such elements;
- Combined failure in the ground and in the structural element;
- Failure by hydraulic heave and piping;
- Movement of the retaining structure, which may cause collapse or affect the appearance or efficient use of the structure or nearby structures or services, which rely on it;
- Unacceptable leakage through or beneath the wall;
- Unacceptable transport of soil particles through or beneath the wall;
- Unacceptable change in the ground-water regime.

For serviceability limit state design, calculated displacements should not be exceeding allowable displacements designated in the code for the proposed earth retaining structure. In addition to soil failure, structural failure of the reinforced structures should always be checked.

2.3. Earth Retaining Structures (ERS)

Earth retaining structures provide lateral support to hold back earth that would otherwise collapse. Earth retaining structures can offer great extent of economic, schedule and constructability benefits. ERSs are typically used in highway construction for the following applications:

- New or widened highways in developed areas,
- New or widened highways at mountains or steep slopes,
- Grade separations,
- Bridge abutments, wing walls and approach embankments,
- Culvert walls,
- Tunnel portals and approaches,
- Flood walls, bulkheads and waterfront structures,
- Cofferdams for construction of bridge foundations,
- Stabilization of new or existing slopes and protection against rockfalls,
- Groundwater cut-off barriers for excavations or depressed roadways (South Carolina Department of Transportation (SCDOT), 2010).

2.3.1. Lateral Earth Pressure

Self-weight of the soil, loads acting on the backfill and additional forces such as seepage, swelling, frost etc. induce lateral earth pressure. Earth pressure establishes in three conditions as seen in Figure 2.4.

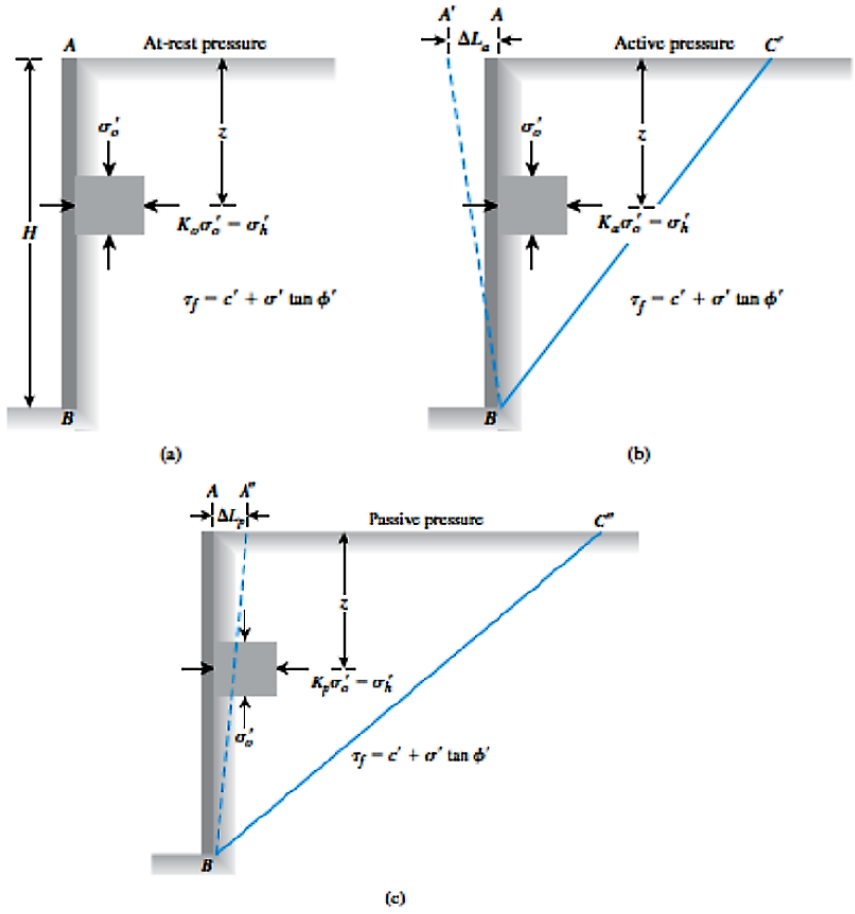

Figure 2.4. Lateral Earth Pressures (a) At Rest (b) Active (c) Passive (Das, 2009).

At rest pressure establishes in case there is no lateral movement of the retaining wall.

Active pressure tends to move the wall away from the backfill. In order for active pressure to be developed, wall movement should be mobilized in other words wall should rotate about its base and away from the backfill. Passive pressure tends to move the wall into to the backfill. In order for active pressure to be developed, wall movement should be mobilized in other words wall should rotate about its base and into the backfill.

Some rotation is required in order to mobilize active and passive conditions, as seen in Figure 2.5.

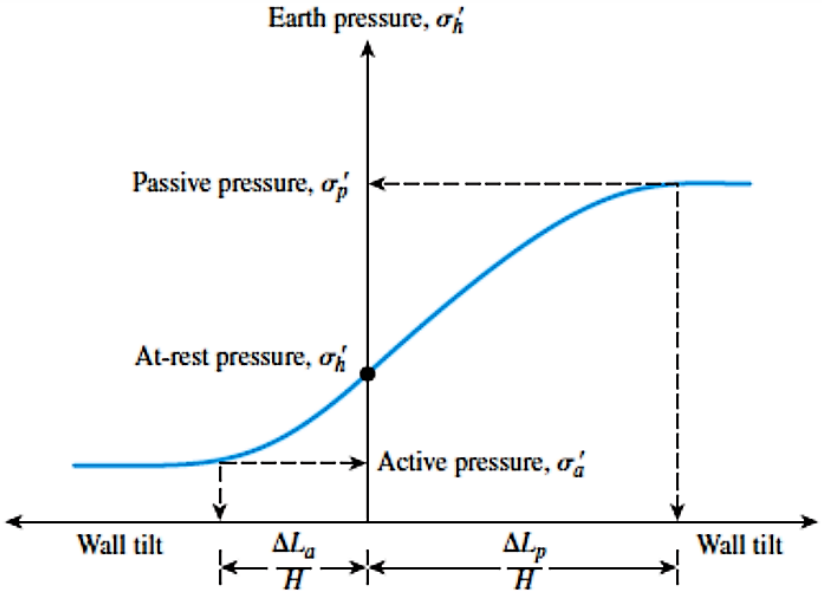

Figure 2.5. Mobilization of Lateral Pressure (Das, 2009).

Amount of rotation required to mobilize active and passive conditions are summarized in the below Table 2.5. Larger rotation is required for passive case.

Table 2.5. Typical Values of Lateral Earth Pressure Mobilization.

Soil Type	L_a/H	L_p/H
Loose sand	0.001-0.002	0.01
Dense sand	0.0005-0.001	0.005
Soft clay	0.02	0.04
Stiff clay	0.01	0.02

At rest condition K_o for normally consolidated cohesive or granular soils is approximately:

$$K_0 = 1 - \sin \emptyset \tag{2.1}$$

There are two common widely used earth pressure theories to estimate coefficients active and passive cases: Coulomb's Earth Pressure Theory (1776) and Rankine's

Earth Pressure Theory (1857).

2.3.1.1. Coulomb Theory. Coulomb earth pressure for theory was developed in 1776. Theory was developed considering cohesionless backfill. The failure surface is a assumed to be planar, and the soil friction between wall and backfill δ is assumed to be in between $\phi/2$ and $2\phi/3$. Coulomb considered limit equilibrium for the force acting on the failure wedge and wall surface, as seen in Figure 2.6.

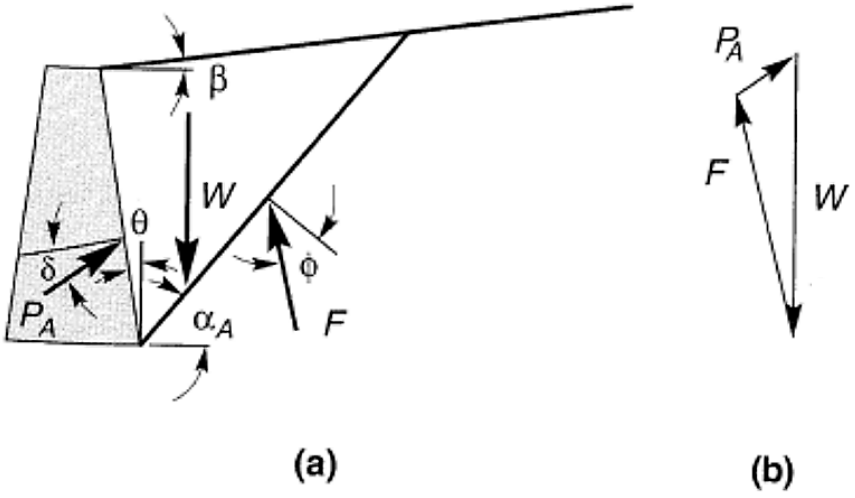

Figure 2.6. Coulomb's Active Wedge (Kramer, 1996).

For active case Coulomb's earth pressure coefficient calculated as:

$$P_a = \frac{1}{2} K_a \gamma H^2 \tag{2.2}$$

and

$$K_a = \frac{\cos^2(\emptyset - \theta)}{\cos^2\theta \cos(\delta + \theta)\left[1 + \sqrt{\frac{\sin(\emptyset+\delta)\sin(\emptyset+\beta)}{\cos\delta+\theta\cos\beta-\theta}}\right]^2} \tag{2.3}$$

Taking Was the weight of the soil wedge, forces acting on the soil wedge can be calculated as seen in Figure 2.7. For passive case Coulomb's earth pressure coefficient

calculated as:

$$P_p = \frac{1}{2} K_P \gamma H^2 \tag{2.4}$$

and

$$K_p = \frac{\cos^2(\emptyset + \theta)}{\cos^2\theta \cos(\delta - \theta)\left[1 + \sqrt{\frac{\sin(\emptyset+\delta)\sin(\emptyset+\beta)}{\cos\delta - \theta\cos\beta - \theta}}\right]^2} \tag{2.5}$$

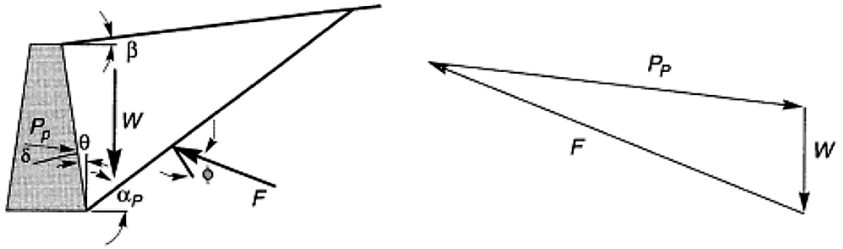

Figure 2.7. Coulomb's Active Wedge (Kramer, 1996).

Coulomb Theory can be used to calculate soil thrusts on walls with irregular backfill slopes, concentrated loads on the backfill surface an seepage forces. By considering the soil above a potential failure plane as a free body and including forces due to concentrated loads, water pressures, and so on, the magnitude of the resultant thrust (PA, PP) can easily be computed (Kramer, 1996).

2.3.1.2. Rankine Theory. Rankine earth pressure theory was developed in 1857. Rankine simplified the Coulomb theory and assumed that:

- There is no friction between soil and the wall.
- Soil is homogenous and isotropic.
- Soil fails by shear as Coulomb's theory is satisfied in any plane.
- Failure surface are straight planes.
- Resultant force is parallel to backfill slope.

Rankine active and passive conditions are illustrated in below Figure 2.8.

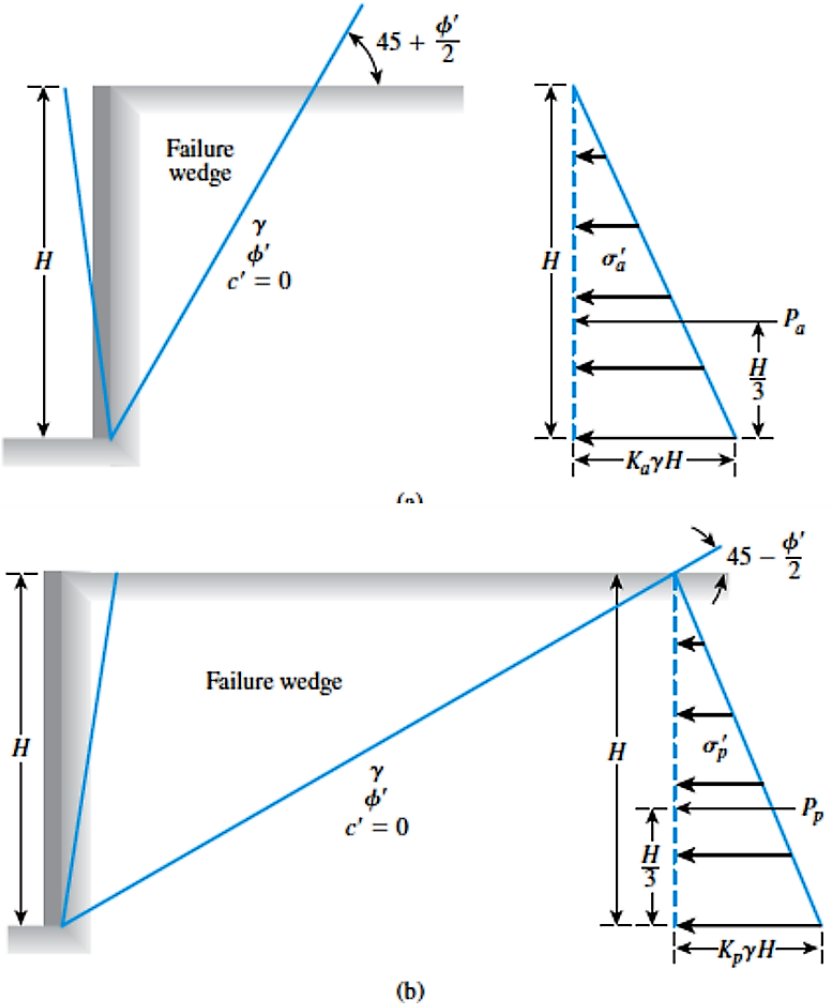

Figure 2.8. Rankine Passive and Active Pressure (Das, 2009).

Coefficients according to Rankine's theory are:

For active case Rankine's earth pressure coefficient calculated as:

$$P_a = \frac{1}{2} K_a \gamma H^2 \tag{2.6}$$

and

$$K_a = \tan^2(45 - \frac{\emptyset}{2}) \tag{2.7}$$

For passive case Rankine's earth pressure coefficient calculated as:

$$P_p = \frac{1}{2} K_P \gamma H^2 \tag{2.8}$$

and

$$K_p = \tan^2(45 + \frac{\emptyset}{2}) \tag{2.9}$$

For the design of geosynthetics reinforced soil walls the U.S. Department of Transportation Federal Highway Administration (FHWA) considers a Rankine failure surface for internal stability checks and assumes Coulomb's method for lateral earth pressure distribution.

2.3.2. Types of Retaining Walls

Earth retaining structures can be designed with different shapes and materials. There are several types of earth retaining structures. Some of which are:

2.3.2.1. Gravity Walls. Gravity walls are the oldest type of earth retaining structures. Lateral forces from backfill are resisted by the weight of the wall itself. Gravity walls may be concrete, stone or masonry.

2.3.2.2. Reinforced Concrete Walls. Reinforced concrete walls could be of several types such as cantilever, counterfort, and RC retaining wall with relieving platforms are seen in Figure 2.9. Anchors may be used in order to meet required F.S.

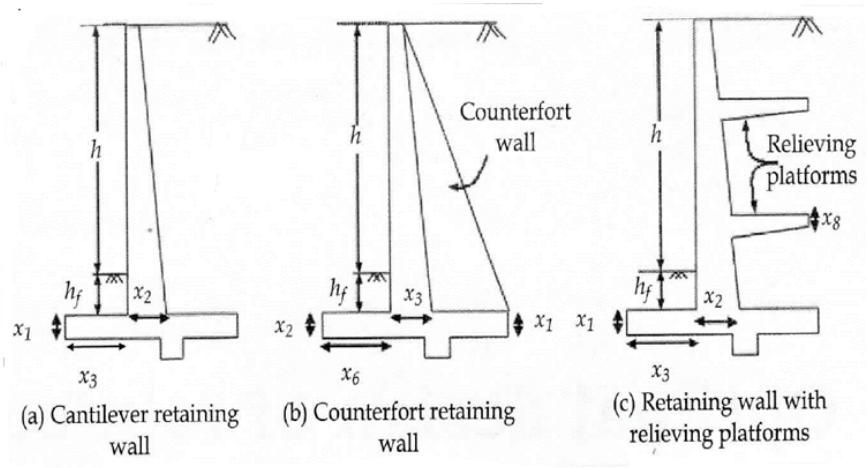

Figure 2.9. Reinforced Concrete Walls (Donkada and Menon, 2012).

2.3.2.3. Reinforced Concrete Pile Walls. Bored cast-in situ piles of either small or large diameter are utilized to avoid excessive bulk excavation and help to control ground movements. Bored pile walls are suitable for the provision of the deep basements, underground structures and motorway cuttings where working space is limited.

2.3.2.4. Crib Walls. Crib walls are interlocking individual boxes made from timber or precast concrete. The boxes are filled with crushed stone or other coarse granular materials to create a free draining structure.

2.3.2.5. Gabion Walls. Gabions are multi-celled, welded wire or rectangular wire mesh boxes, which are rock filled. Gabion walls are mainly used for construction of erosion control structures and to stabilize steep slopes.

2.3.2.6. Sheet Pile Walls. Sheet piles are steel sheet sections with interlocking edges that are widely used to build continuous walls for waterfront structures and/or for temporary construction.

Optimization which is fulfilling quality, time, and budget criteria of the project is the upmost objective of the engineer. Several criteria should be considered to select the most effective solution of the engineering problems.

For earth retaining structures the major considerations for the selection are:

- Ground type,
- Ground water level,
- Constructability,
- Speed of construction,
- Right of way,
- Aesthetics
- Environmental concerns,
- Durability and maintenance,
- Tradition,
- Local contracting practices.

2.4. Geosynthetic Reinforced Soil Walls

Geosynthetic Reinforced Soil (GRS) walls composed of geosynthetic reinforced soil body and wall facing. Geosynthetics provides a reinforcement function by developing tensile forces which contribute to the stability of geosynthetics - soil composite in other words reinforced soil structure. In the first place stability problem tries to be overcome only using geosynthetics. If the capacity of the geosynthetics itself is not sufficient, geosynthetics reinforced earth retaining walls are used.

Typical uses of geosynthetic reinforced walls are illustrated in Figure 2.10 below.

External, internal and global stability checks for geosynthetic reinforced soil should be conducted, considering failure modes shown in Figure 2.11.

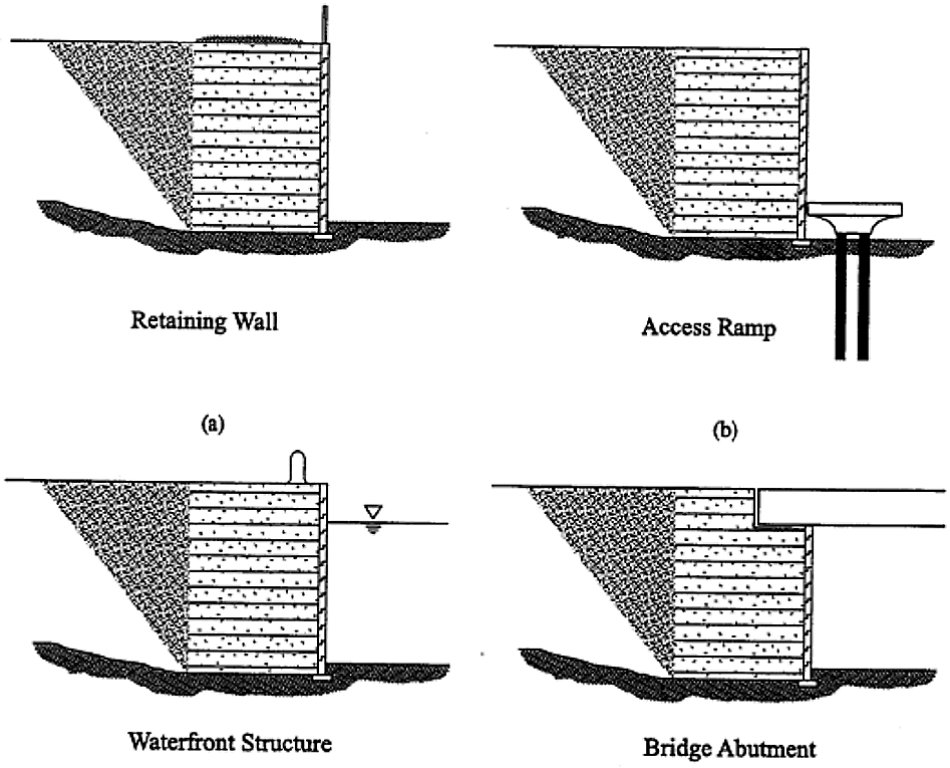

Figure 2.10. Reinforced Wall Applications (Berg *et al.*, 2009).

For External stability geosynthetic reinforced soil wall is considered as coherent mass and checked against;

- Base sliding,
- Overturning,
- Bearing capacity.

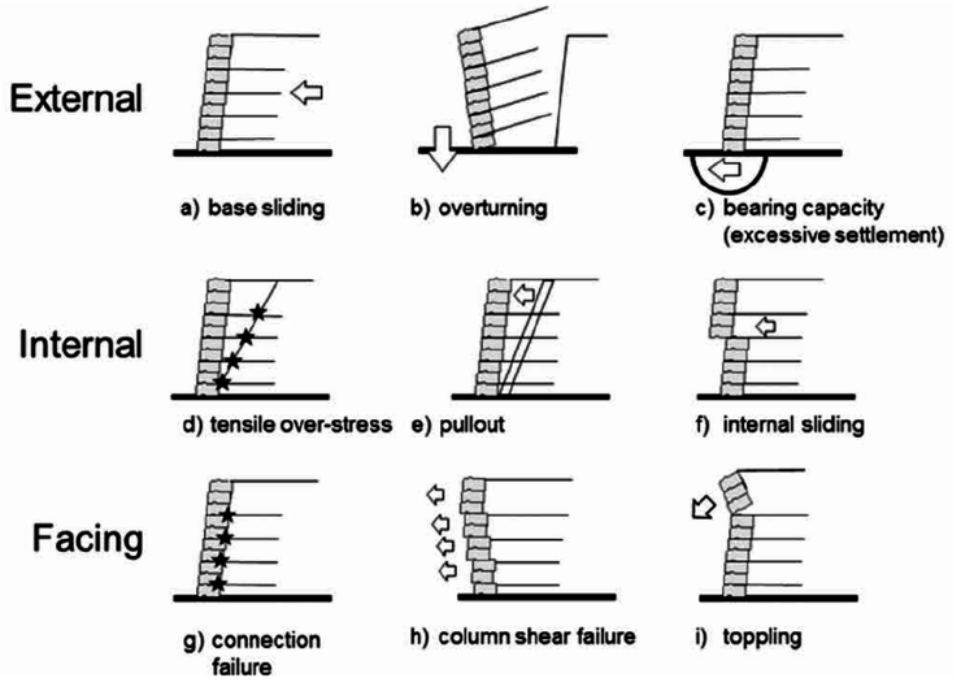

Figure 2.11. Failure Modes of GRS Walls (Bathurst, 2014).

Internal stability is checked to assure structural integrity of the system against;

- Tensile over stress,
- Pullout,
- Internal sliding.

Finally facing and connections should be check for the global stability of the system against;

- Connection failure,
- Column shear failure,
- Overturning.

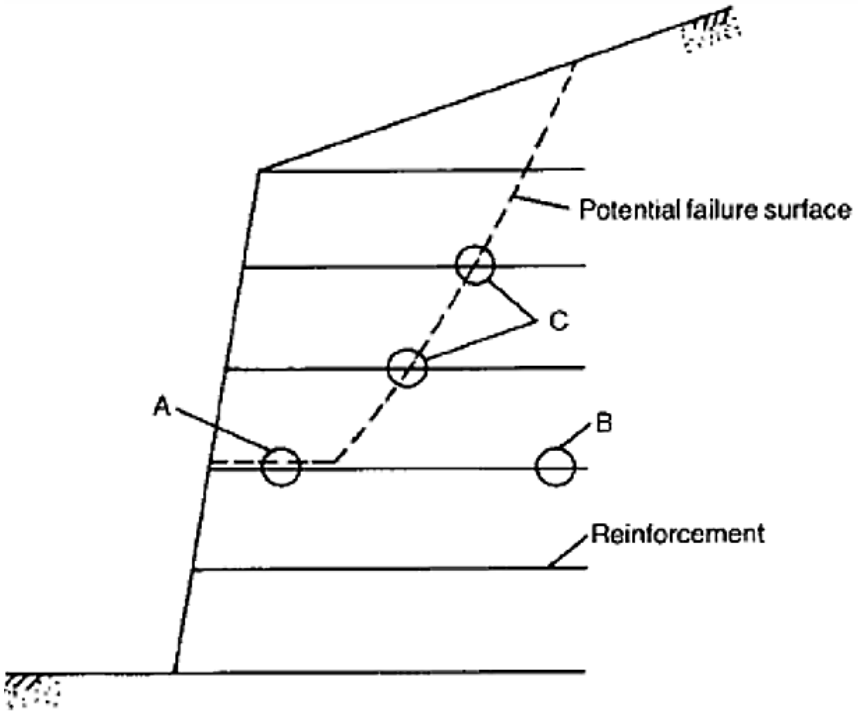

Figure 2.12. Interaction Mechanism in Reinforced Soil (Palmeria and Milligan, 1989).

Palmeria and Milligan (1989) explained critical reinforcement-soil interaction mechanisms in reinforced soil as shown in Figure 2.13.

Shear failure is the dominating failure mode at point A which could be demonstrated by the direct shear test. Pullout failure is profound at Point B which could be demonstrated by the pullout test. At point C combined mechanism is observed.

In the guidelines pullout is checked to have adequate embedment of the reinforcement reinforced which resists driving force of lateral earth thrust along the critical slip plane. Pullout resistance is provided by soil-reinforcement interface friction.

The capacity of a GRS is related to the effects of confinement reinforcement spacing, strength and stiffness, shape and location of the failure surface, stress strain behavior of the soil, and degree of mobilization of shear resistance along an assumed failure plane (Wu and Ooi, 2015).

Advancement in geosynthetics technology and a better understanding of reinforced soil structure behavior has allowed design engineers to use geosynthetics products in several applications. One of the new applications of geosynthetic technology is Geosynthetic Reinforced Soil-Integrated Bridge Systems (GRS-IBS) as shown in Figure 2.14. Geosynthetic Reinforced Soil is an engineered fill of closely spaced (< 12") alternating layers of compacted granular fill material and geosynthetic reinforcement and Integrated Bridge System is a fast, cost-effective method of bridge support that blends the roadway into the superstructure using Geosynthetic Reinforced Soil technology (Adams *et al.*, 2011).

In addition to significant cost advantage, differential settlement between the approaching slab and beam seat is minimized in GRS-IBS systems.

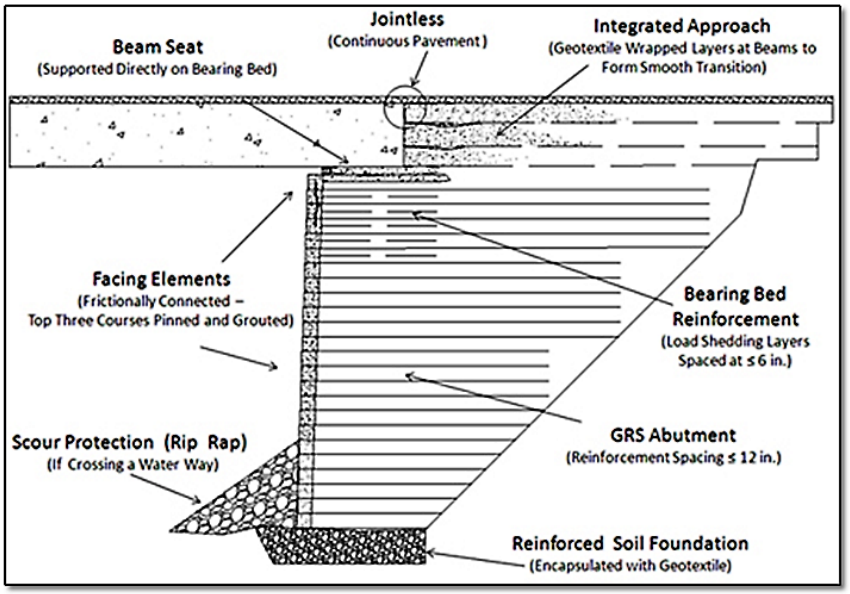

Figure 2.13. GRS-IBS System Cross Section (Adams *et al.*, 2011).

2.5. Soil-Geogrid Interface

Resistance of geogrids is developed in two mechanisms: bearing capacity of transverse ribs and frictional resistance mobilized on surface areas of geogrid. Main interactions mechanisms between geogrid and soil are illustrated in Figure 2.14:

- Pullout behavior (Lateral Restraint),
- Membrane effect (Tensioned Membrane Effect),
- Constraining effect (Improved Bearing Capacity).

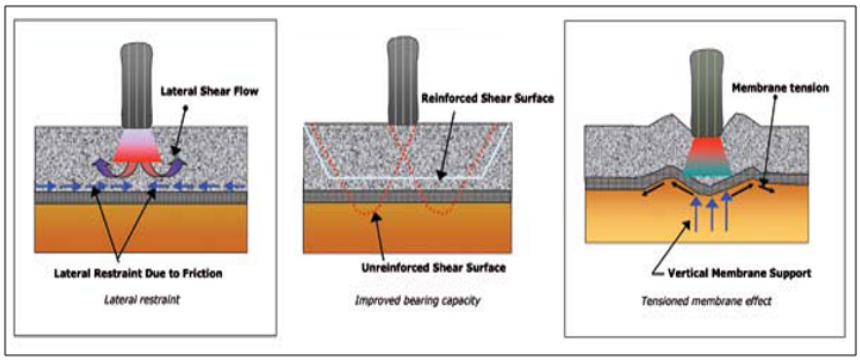

Figure 2.14. Geogrid-Soil Main Interaction Mechanism (Archer, 2008).

Moraci and Gioffre (2006) proposed following equation to theoretically estimate the maximum pullout resistance of geogrid:

$$P_R = P_{RS} + P_{RB} \tag{2.10}$$

where P_R is the maximum pullout resistance, P_{RS} is frictional resistance and P_{RB} is bearing resistance.

P_{RB} can be evaluated from expression proposed by Jewell (1990):

$$P_{RB} = \frac{L_R}{S}\alpha_B \sigma_b B \tag{2.11}$$

where L_R is embedded length of geogrid, S is spacing of geogrid bearing members, α_B is total frontal area of geogrid, B is thickness of the bearing member, σ_B is effective bearing stress as shown in Figure 2.15.

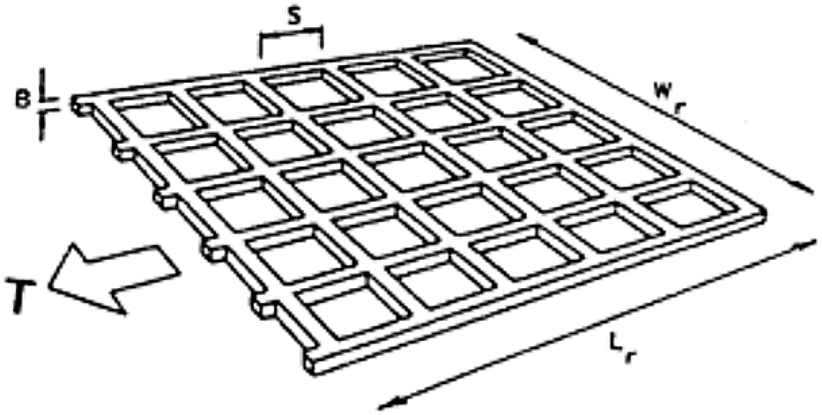

Figure 2.15. Bearing Resistance Members (Jewell, 1990).

and frictional resistance can be calculated from following Moraci and Gioffre (2006) expression:

$$P_{RS} = 2\alpha_S L_R \sigma_n \tan\delta \tag{2.12}$$

where α_S is solid geogrid surface area fraction, L_R is embedded length of geogrid, σ_n is normal effective stress , $tan\delta$ is skin friction angle between at interface.

Strength, as physical characteristics, of geogrids is dependent on the constituted polymer type. Stiffness of junctions is dependent on the polymer type and manufacturing method of the geogrids. Geometry of the geogrids, as shown in Figure 2.16, is defined by the aperture size, thickness and width of the ribs, distance between transverse and longitudinal ribs. Geometry of the geogrids affects the soil-geogrid interaction in many ways.

Interface behavior of geogrids is mainly affected by characteristics of the soil, stiffness of the geosynthetic, geometry of geosynthetics, and effective vertical stress (i.e. overburden pressure).

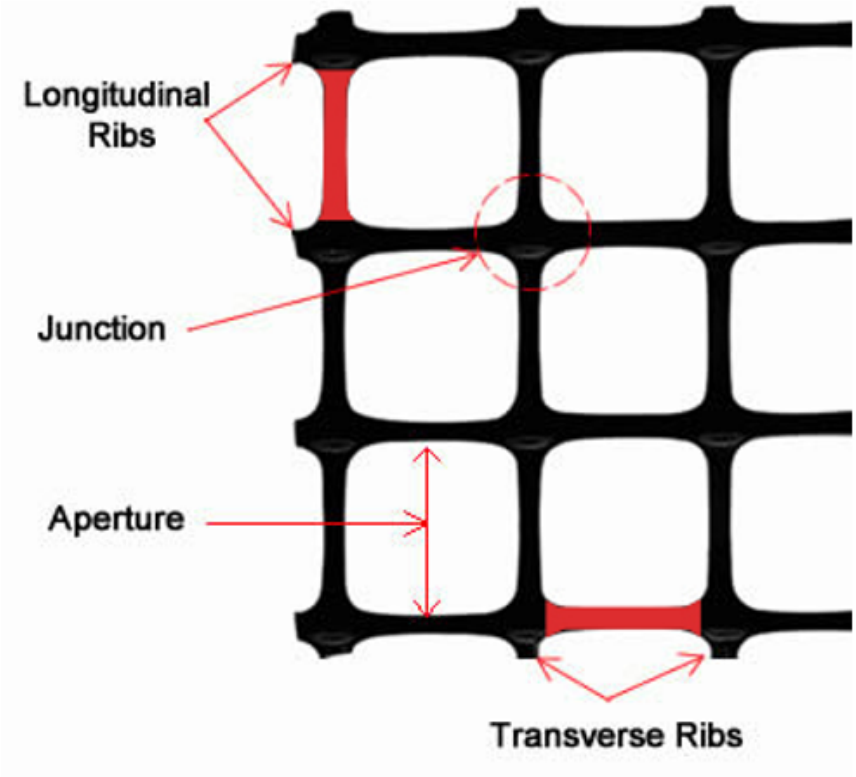

Figure 2.16. Geogrid Ribs, Aperture and Junctions (Courtesy of Tigergrid Geosynthetics).

The pullout resistance of the reinforcement is mobilized through one or a combination of the two basic soil-reinforcement interaction mechanisms, interface friction and passive soil resistance against transverse elements of reinforcements such as bar mats, wire meshes, or geogrids. The load transfer mechanisms mobilized by a specific reinforcement depends primarily upon its structural geometry (i.e., composite reinforcement such as grids, versus linear or planar elements, thickness of transverse elements, and aperture dimension). The soil-to-reinforcement relative movement required to mobilize the design tensile force depends mainly upon the load transfer mechanism, the extensibility of the reinforcement material, the soil type, and the confining pressure. (Berg *et al.*, 2009). Frictional stress transfer mechanism is illustrated in Figure 2.17.

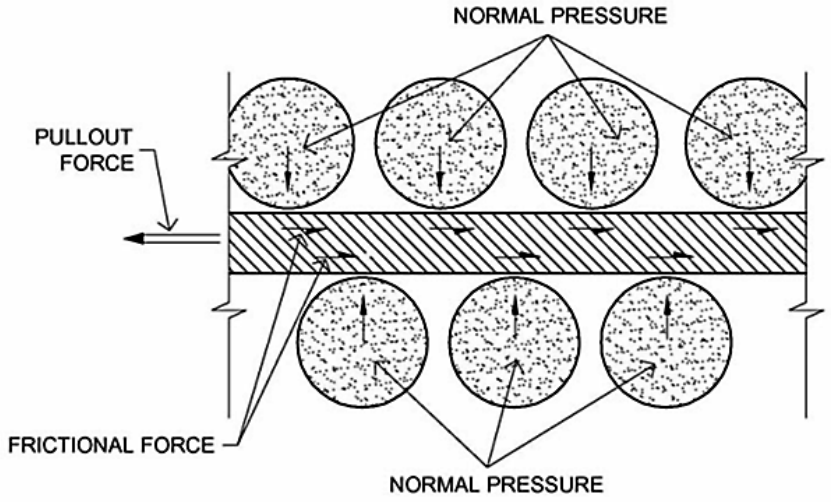

Figure 2.17. Frictional Stress Transfer Between Soil and Reinforcement (Berg *et al.*, 2009).

2.6. Shear Band

Failure of frictional materials is often characterized by bifurcation and spontaneous localization of deformations into rupture zones called "shear bands" that have certain thicknesses and patterns (Alshibli and Sture, 1999). Shear bands for soils referred to the zones of localized shear deformations in the soil body. Shear bands can be characterized by the thickness and the geometry of the band. In shear band zone two soil bodies shift in opposite directions as shown in Figure 2.18.

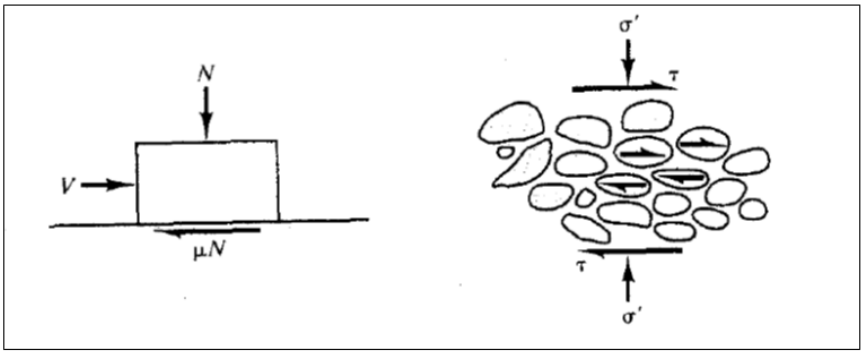

Figure 2.18. Analogy of Frictional Strength and Sliding Block (Coduto, 2001).

Thickness of the shear band is proportional to the magnitude of the shear strain. Propagation of the shear bands leads to the failure of the soil. Shear banding occurs in many geological and industrial situations such as snow avalanches, collapse of geotechnical structures, chute flow and hopper flow. It has been the subject of various experimental, theoretical and numerical studies in the past decades and still poses challenges for theoretical descriptions. For a granular material, once a shear band is formed, further deformation is mostly accommodated by the material within the shear band. Thus, it is critical to understand the nature of granular material behavior within the shear band so as to accurately characterize the physical behavior for large deformations (Liu *et al.*, 2012).

Shear strains in localized zones are generally plastic and are very closely related to the failure. Therefore it is critical to understand the mechanism of the shear band formation and propagation. Extensive research has been carried out to analyze and quantify the shear band mechanism in soils. And recently those techniques have been utilized to understand the soil geosynthetics interaction and shear band mechanism in geosynthetic reinforced soil. Shear bands will certainly appear in the zone adjacent to the contact surface between soil and geosynthetics when the shear strain reaches a certain extent (Zhou *et al.*, 2012).

Thickness of the shear band is dependent on several factors. Researchers carried out studies to derive shear band thickness theoretically and conducted experiments to measure shear band thickness.

Soil particle size is one of the major factors influencing the thickness of the shear band. By using Cosserat's continuum theory Muhlhaus and Vardoulakis (1987) theoretically derived that the shear band thickness is proportional to mean particle size (d_{50}). Alshibli and Sture (1999) conducted experimental studies on sand using digital image techniques to measure the shear band thickness and found out that the normalized shear band thickness (t/d_{50}) decreases as grain size increases. Bariether *et al.*, (2008) showed that not only particle size affects the interface friction but also particle roundness contributes to the soil-geosynthetics interface. Therefore, it is expected

that the thickness of the shear band will vary significantly in granular and coarse soil particles.

Alshibli and Sture (1999) also concluded that the shear band thickness is directly proportional to soil dilatancy angle. Due to soil dilatancy, which decreases with an increase in the confining vertical effective stress, two main effects develop: the first is due to the different work made to expand the dilatancy surface at different vertical effective confining stresses; the second effect is due to the restriction of the dilatancy connected to the nearby soil stiffness (constrained dilatancy), which produces a local increment of the effective confining stress (Moraci and Gioffre, 2006).

Restrained dilatancy effect is also explained by Lo (1998) as the volumetric dilation of the soil elements in the vicinity of the strap will be constrained by the surrounding soil. Lo (1998), ran pullout test at low overburden pressure with reinforced soil to explain the constrained dilatancy effect. Figure 20 illustrates the constrained dilatancy concept in reinforced soil.

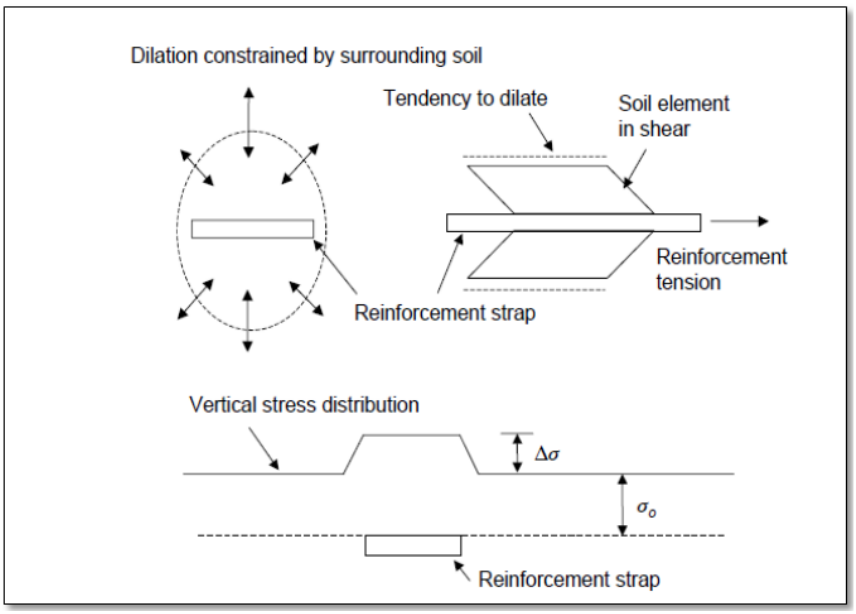

Figure 2.19. Constrained Dilatancy (Lo, 1998).

In order to analyze large scale triaxial test results, Ruiken and Ziegler (2009) used dilatancy angle as main parameter to predict the deformation of geogrid reinforced soil.

Guilloux *et al.*, (1979) observed restrained dilatancy effect under field conditions when the reinforcement is pulled out. Kitsabunnarat *et al.*, (2008) conducted finite element analysis of a GRS Retaining Wall and showed that when the reinforcement spacing is smaller, geosynthetic reinforcements were more effective to impede the shear band formation. Theoretical analyses and experimental results show that the restrained dilatancy contributes to the interface shear stress, therefore it is inversely proportional to the shear band thickness.

Since the width and thickness of the ribs contributes to the strength and stiffness of the soil-reinforcement interface geometry of the reinforcement also affects the shear band thickness. Fannin and Raju (1993) ran experiments with geosynthetic reinforced sand and showed that the textured geomembrane mobilizes greater interface bond that the smooth geomembrane. Ruiken *et al.*, (2012) compared the results of biaxial compression tests with geogrid reinforced soil and concluded that the rougher rib surfaces contributes to the load transfer between soil and geogrid.

2.7. Shear Band Measurement Techniques

Researchers have developed and utilized several techniques to make accurately measure deformations and monitor shear band mechanism. Alshibli and Sture (1999) ran triaxial tests with sand and used digitized latex membrane data to measure shear band thickness and orientation angle. Several researches (Wolf *et al.*, 2005, Lesniewska *et al.*, 2000, Sugimoto *et al.*, 2001, Pardi *et al.*, 1990, Ruiken *et al.*, 2011) utilized x-ray systems to identify and show shear band patterns.

Recently, Digital Image Correlation (DIC) which is based on the Particle Velocimetry Method (PIV) is extensively utilized to determine the displacements of the soil particles. White *et al.*, (2003) applied the principles of PIV to geotechnical engineering by using the texture of sands as the features that create a pattern to be recognized with the correlation function in replacement of the seeding particles in fluid. The texture of sands in the image is created by their grains of different colors and the shadows between adjacent grains created by illumination, creating a pattern of

different grey shades, or light intensity values, in the image. These values are recorded by each pixel that forms a 2D array of thousands of points in the image of resolution X x Y. For example, an image with a resolution of 5 Megapixels (MP) is generally composed by an array of 2,452 x 2,056 pixels (X x Y). The location of a pixel in the image is defined by the coordinates (x,y) (Ferreira, 2013).

In summary Digital Image Correlation is an Image Analysis tool to track the displacement and calculate the strain and stress from image sequences. The working principle of DIC is illustrated in Figure 2.20.

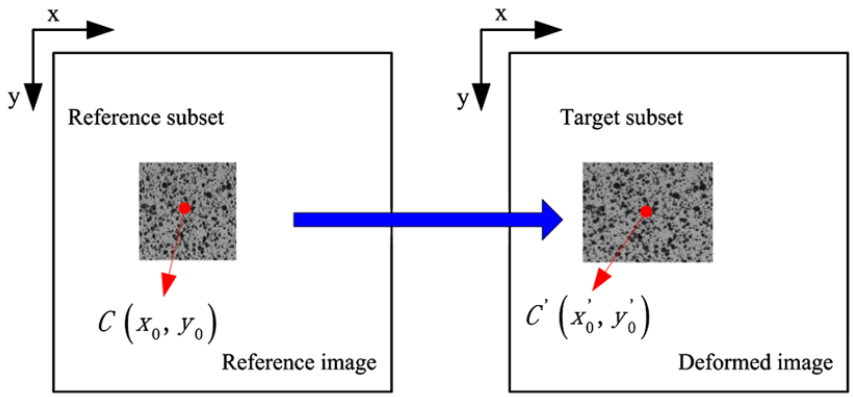

Figure 2.20. DIC Reference and Target Subsets (Tang *et al.*, 2012).

The method requires a series of digital pictures of the object, each taken from the same position within a certain time or displacement increment (Figure 2.21(a)). By means of DIC the displacements of small areas of the soil mass (interrogation windows) are determined and displayed in a vector plot (Figure 2.21(b)). On the basis of the vector field strains can be calculated (Figure 2.21(c)) (Wolf *et al.*, 2005).

There are 255 different intensities that can be digitally represented for 8 bit gray scale image: 0 for black and 255 for white (illustrated in Figure 2.22). Gray scale intensity values are the averaged values for red, green and blue intensities.

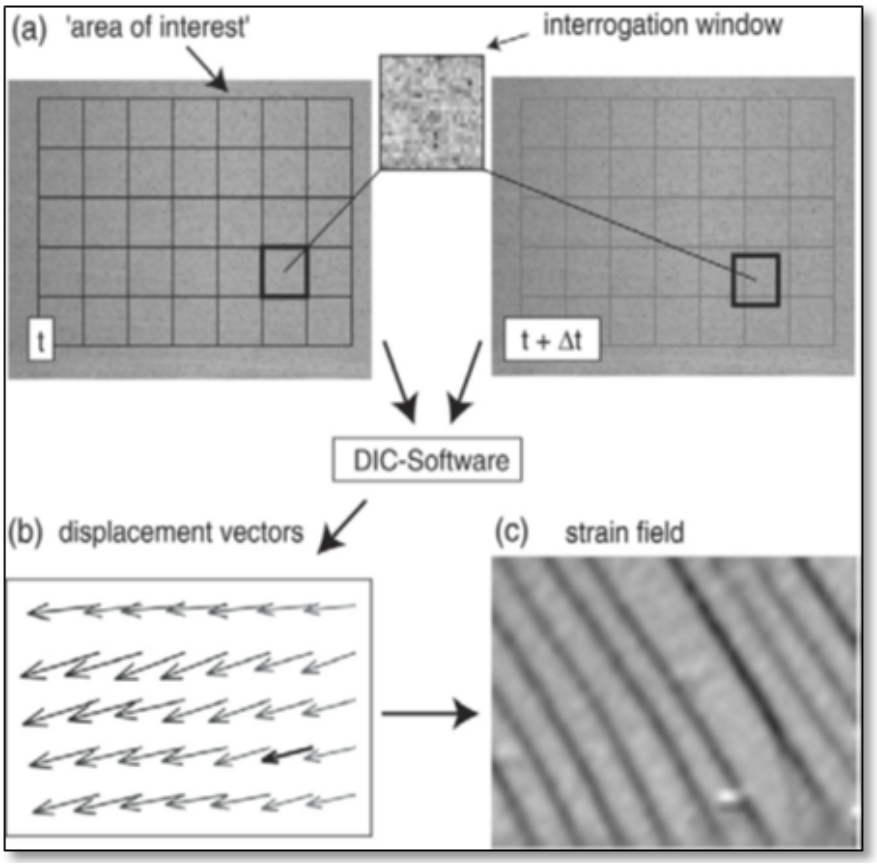

Figure 2.21. DIC Working Principles (Wolf *et al.*, 2005).

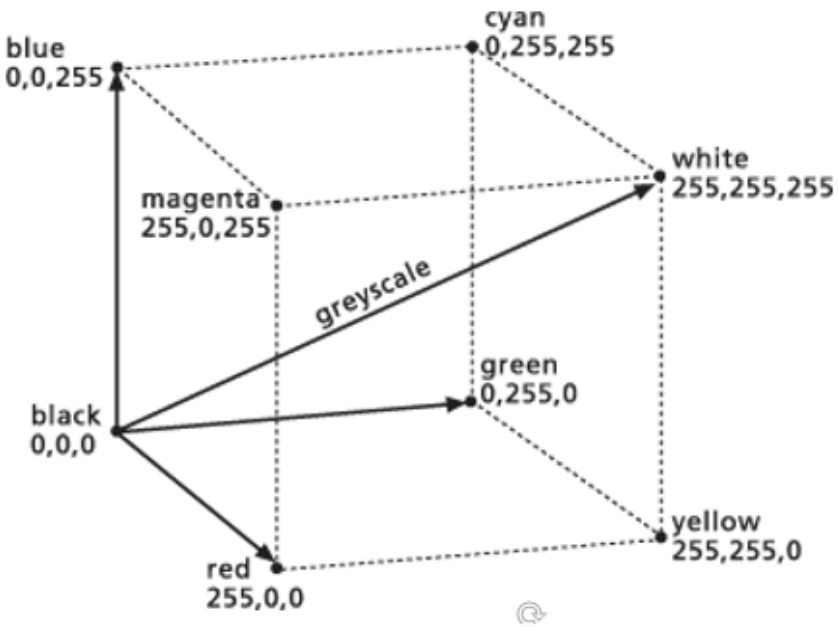

Figure 2.22. Color Intensity Cube (Courtesy of Arcgis).

Digital Image Correlation software calculates displacements in image space as pixels. Next step is converting pixels to millimeter/centimeter. Conversion should be done base on a scale factor which accurately correlates the pixels and real object of known dimensions. Analogy of the transformation from image-space coordinates to object-space coordinates are shown in below Figure 2.23.

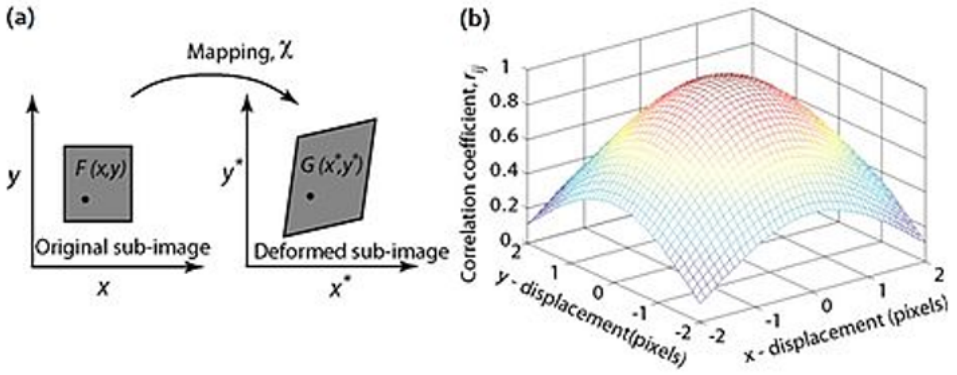

Figure 2.23. Digital Image Correlation Mapping (Courtesy of Wikipedia).

3. METHODOLOGY

3.1. Test Setup

To have a better understanding of soil-geosynthetics interaction, several experimental setups have been developed. Most widely used methods are direct shear tests and pull-out tests. Pullout is a performance which is intended to measure the resistance of a geosynthetic reinforcement layer to pullout from confined soil. In this method, the geosynthetic layer is embedded between two soil layers as shown in Figure 25. A horizontal force is applied to the geosynthetic layer axially. The force is can be applied at a constant displacement rate, constant force rate, stepped force rate (ASTM Standard D 6706 - 01, 2013). ASTM Standard D 6706 - 01 (2013) defines procedures for pullout testing.

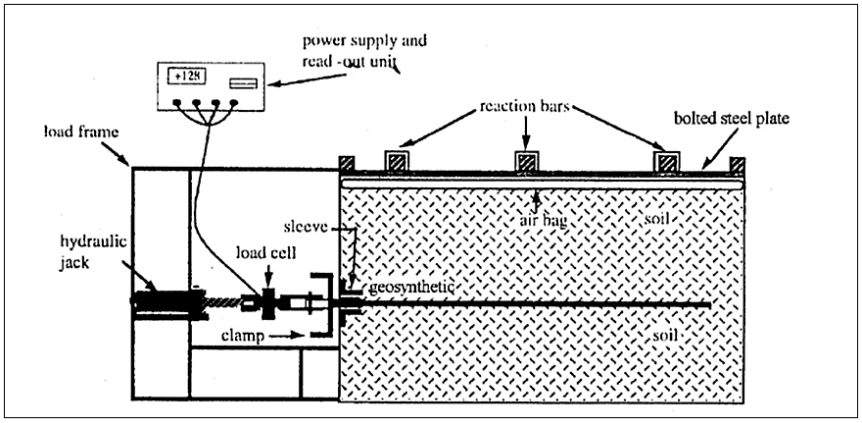

Figure 3.1. ASTM Pullout Test Setup (ASTM Standard D 6706 - 01, 2013).

Pullout setup used in this experimental research has the same fundamental components of traditional (ASTM Standard D 6706 - 01) pullout setup. Those variations in the setup add up to significant practical advantages of small pullout test setup compared to the traditional one. As the volume of soil to be tested is significantly smaller compared to traditional setup, easiness of compaction is much greater in small pullout setup.

Also, the setup and completion of the tests are extremely quicker compared to traditional pullout setup. In addition to practicality, small pullout setup is also advantageous in cost wise. Ferreira (2013) improved the test setup (shown in below Figures 26 and 27) and conducted 323 small pullout tests successfully under the research project 5-4829 with TxDOT (Zornberg *et al.*, 2013).

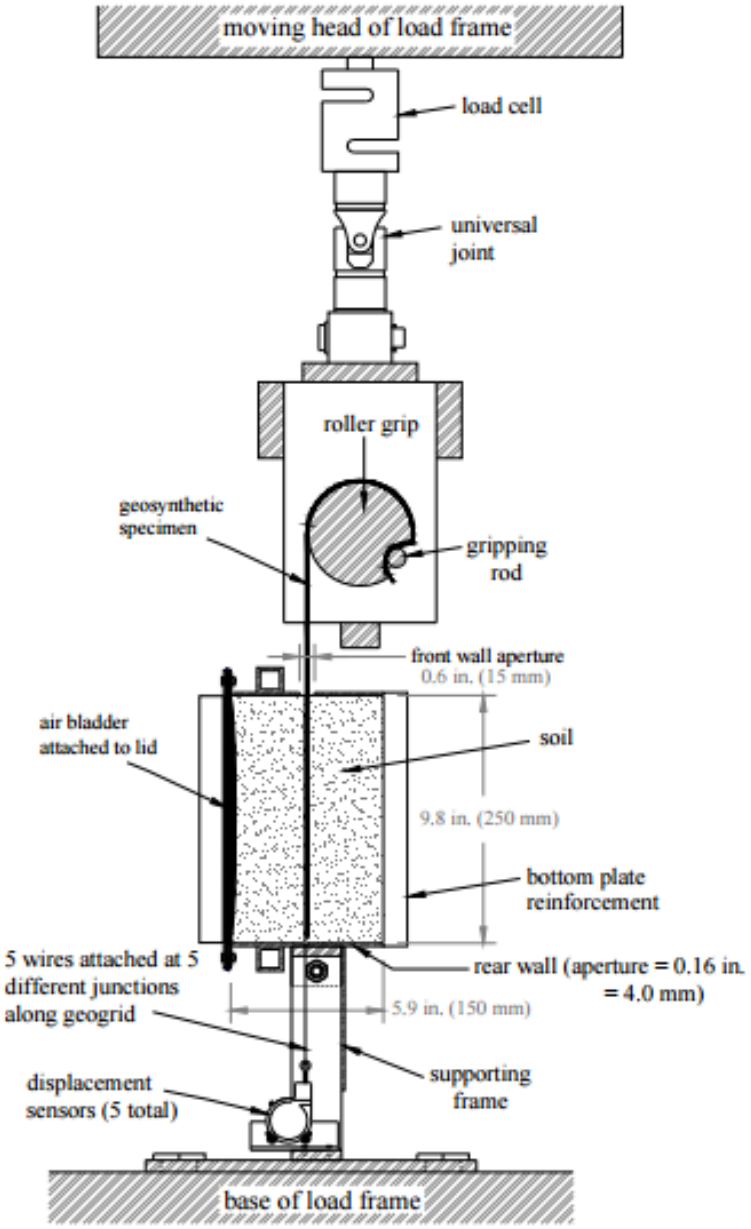

Figure 3.2. Cross Section of Small Pullout Test Device Setup at UT Austin (Zornberg *et al.*, 2013).

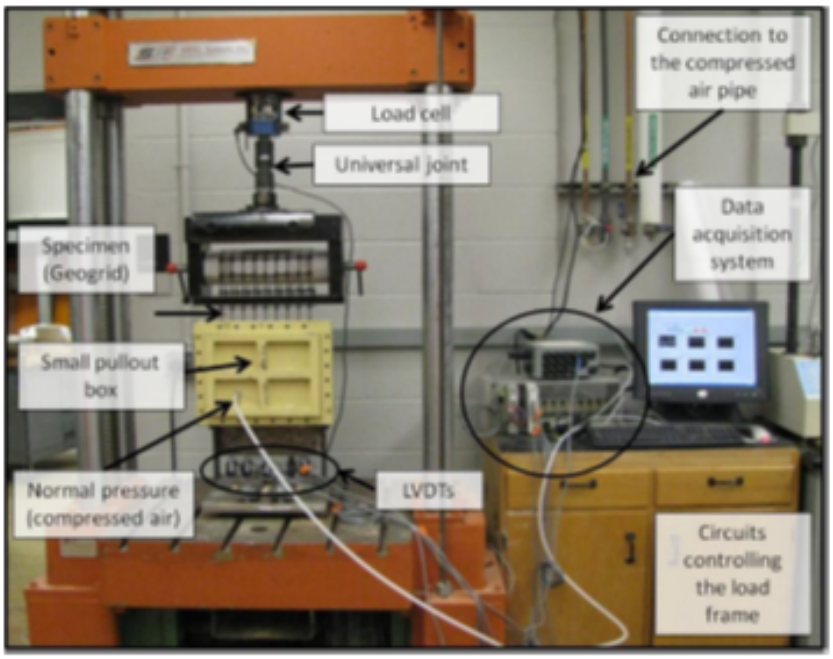

Figure 3.3. Load Frame and Small Pullout Box at UT Austin (Roodi, 2016).

Internal dimensions of steel small pullout box are 30.0 cm x 25.0 cm x 15.0 cm. Load frame also contain linear variable differential transformers (LVDTs). LVDTs are electrical transformers, which are used to measure axial displacements along the specimen via attached steel wires. 5 LVDTs were placed in different locations along the specimen. Load cell of the frame has a capacity of 22 kN, which measures the applied pullout load (lbf). Normal pressure (overburden) is applied via air bladder on the lid. Roodi (2016) evaluated comparison between small pullout test results and large scale pullout test results, and concluded that the small scale setup is suitable.

In this research same dimension steel box was modified to enhance the assessment of the shear band evolution. Specifically, one side of the box was replaced with acrylic to make it transparent and to be able to observe the soil-reinforcement interface shear band. Data acquisition system is National Instruments. Frequency of data acquisition for LVDT and load cell measurements is 0.2 second.

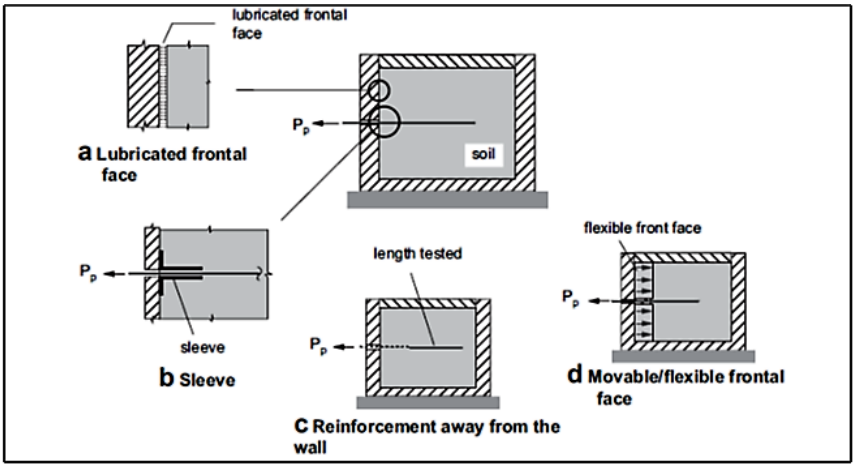

Figure 3.4. Typical Boundary Conditions of Pullout Tests (Palmeira, 2009).

3.2. Modification of the Box and Testing Setup

The most challenging part of this research was to set up a test configuration that would allow measurement of shear bands as accurate as possible. Ten trial tests were run in order to come up with a final configuration for the accurate data and image analysis.

In the first place one side wall of the box was modified in order to enable imaging during pullout test, as shown in Figure 29. The opening was covered with acrylic, which is transparent and mechanically sufficient for the testing.

Initially 2.54 cm x 2.54 cm (1.00"x1.00") gridded latex membrane used at the transparent side for testing with BSOIL 1 but after few trial tests it is observed that there are inconsistencies due to the slippage of the aggregate particles along the latex membrane. Also 2.54 cm x 2.54 cm grid found to be inaccurate for image analysis purposes, as shown in Figure 3.6.

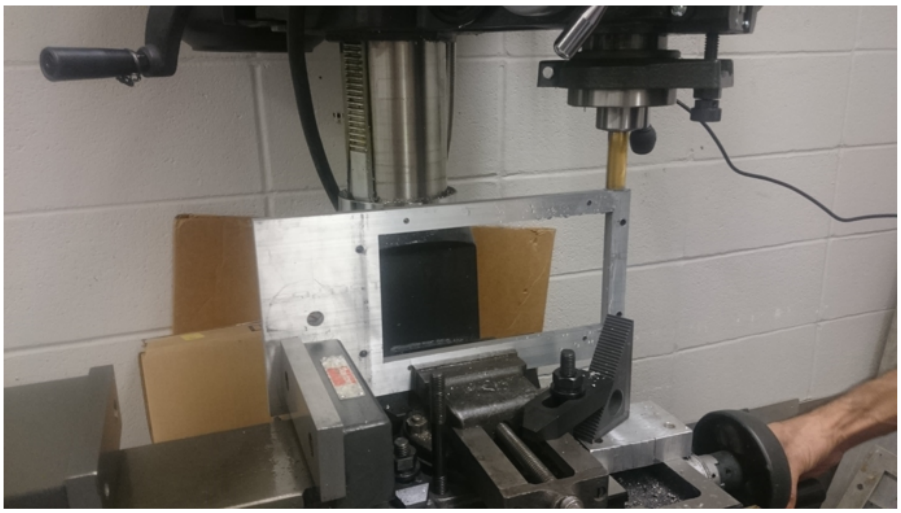

Figure 3.5. Side Wall with Opening.

Figure 3.6. Initial Grid 2.54 cm x 2.54 cm.

Due to the restrictions of the size sleeve is not used in this test program. But one trial test is conducted with sleeve and it is observed that the addition of the sleeve for this particular setup is not effective. 7.5 cm sleeve inserted into the side wall as shown in Figure 3.7.

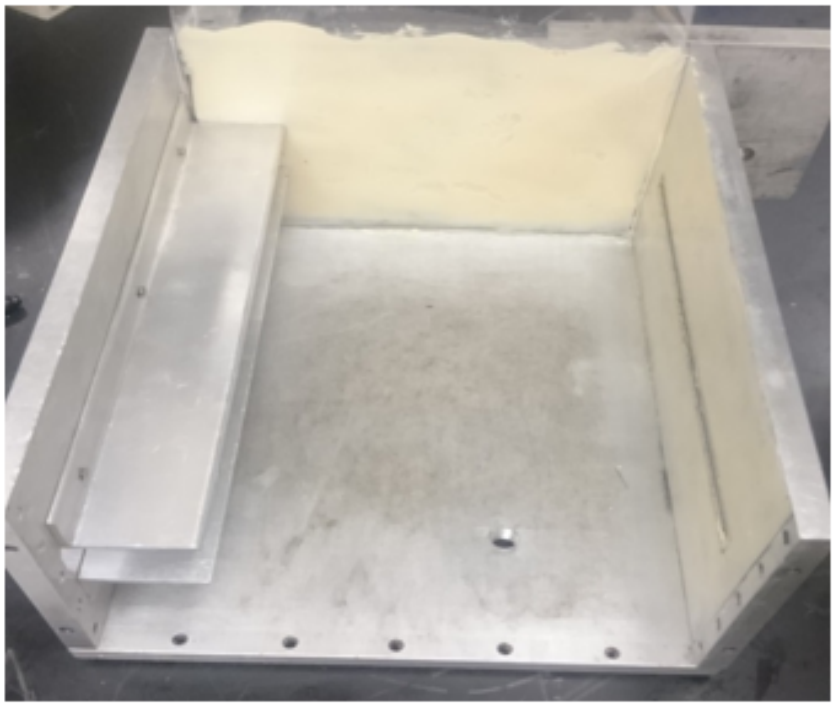

Figure 3.7. Pullout Box with Sleeve.

One trial test with two pressurized air bladders also conducted as shown in Figure 3.8.

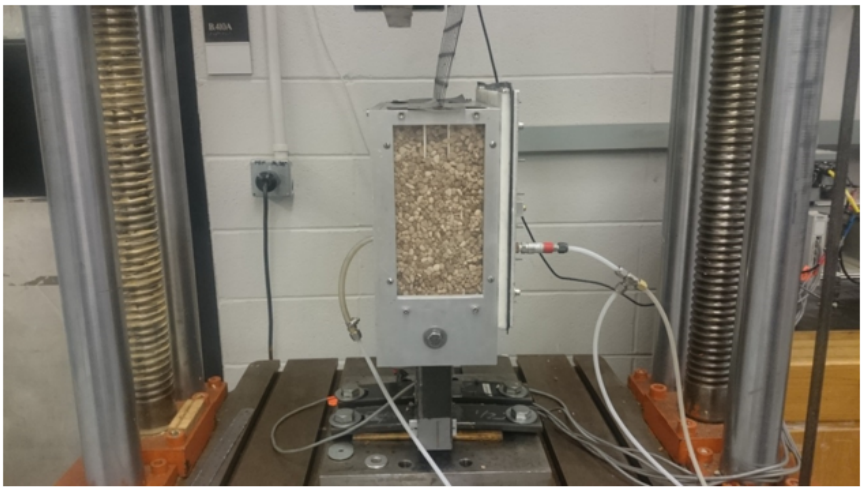

Figure 3.8. Trial Test with 2 Pressurized Air Bladders and 7.5 cm sleeve.

All test configurations are summarized in the following Table 3.1.

Table 3.1. All Test Configurations.

Test #	Backfill Soil	Geogrid Type & Width	Overburden Pressure	Latex Membrane	Sleeve	Remarks
160314	BSOIL 1	GG PP 30 cm	35 kPa	None	None	None
160316	BSOIL 1	GG PP 30 cm	21 kPa	None	None	None
160321	BSOIL 1	GG PP 30 cm	14 kPa	None	None	None
160408	BSOIL 2	GG PP 30 cm	14 kPa	2.54 cm x 2.54 cm grid	None	None
160413	BSOIL 2	GG PPTG 30 cm	21 kPa	0.64 cm x 0.64 cm grid	None	None
160421	BSOIL 1	GG PPTG 30 cm	21 kPa	None	None	None
TRIAL 151118	BSOIL 1	GG PP 30 cm	21 kPa	2.54 cm x 2.54 cm grid	None	Quality of the pictures are not accurate to run analysis
TRIAL 151125	BSOIL 1	GG PP 30 cm	35 kPa	2.54 cm x 2.54 cm grid	None	Quality of the pictures are not accurate to run analysis
TRIAL 160203	BSOIL 1	GG PP 30 cm	21 kPa	n/a	None	Box tilted during the test, pictures cannot be processed
TRIAL 160204	BSOIL 1	GG PP 30 cm	21 kPa	1.28 cm x 1.28 cm grid	None	None
TRIAL 160307	BSOIL 1	GG PP 28 cm	21 kPa	0.64 cm x 0.64 cm grid	2.5 cm	None
TRIAL 160309	BSOIL 1	GG PP 28 cm	21 kPa	0.64 cm x 0.64 cm grid	2.5 cm	None
TRIAL 160311	BSOIL 1	GG PP 30 cm	35 kPa	0.64 cm x 0.64 cm grid	None	Due to image acquisition problem, analysis cannot be run
TRIAL 160325	BSOIL 1	GG PP 30 cm	21 kPa	None	7.5 cm	None
TRIAL 160329	BSOIL 1	GG PP 30 cm	21 kPa	None	7.5 cm	None
TRIAL 160405	BSOIL 2	GG PP 30 cm	21 kPa	0.64 cm x 0.64 cm grid	None	Test with 2 compressed air bladder

Previous small pullout test setup being used at University of Texas at Austin and modified setup developed for this research are shown in below Figure 3.9 and Figure 3.10 respectively. Sizes of the box are the same; the difference is that the modified box has a transparent side (acrylic mounded side wall).

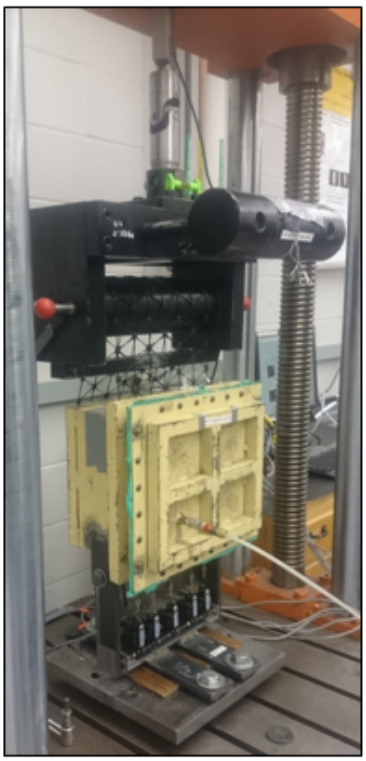

Figure 3.9. Small Pullout Test Setup.

Figure 3.10. Modified Small Pullout Test Setup.

3.3. Material Properties

3.3.1. Backfill Material

In this research two different soil types were used as backfill: Monterey Sand #30 (hereinafter BSOIL 2) and 3/8" Sieved Aggregate (hereinafter BSOIL 1).

BSOIL 1 meets the specifications of AASHTO #8 aggregate as per ASTM M43 (2005) tabulated in Table 3.3.1. BSOIL 1 contains particles passing through 3/8" (9.5mm) sieve up to Sieve #16 (1.18mm). Dry unit weight of the sand was measured 16.2 kN/m^3 after compaction and specific gravity is 2.61.

BSOIL 2 is classified as SP (Poorly Graded Sand) and BSOIL 1 aggregate is classified as GP (Poorly Graded Gravel) with regards to Unified Soil Classification System (USCS) (ASTM D 2487-11, 2011). Gradation curves for both soil types were shown in Figure 3.11.

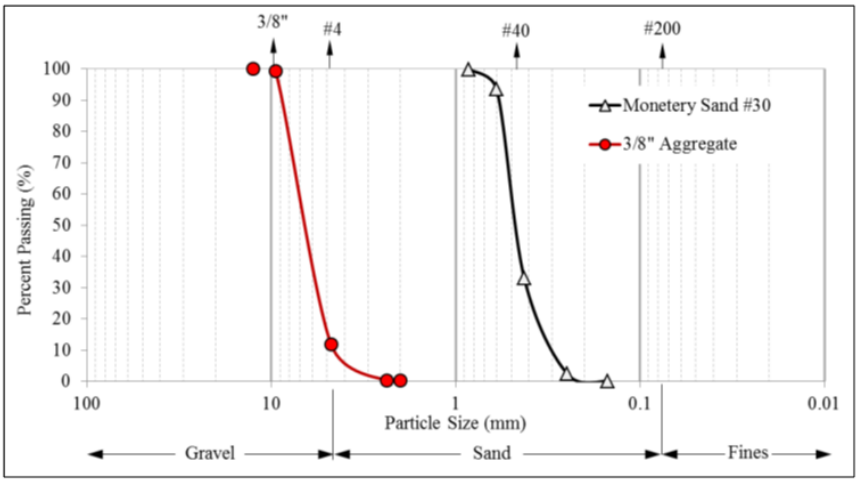

Figure 3.11. Gradation Curves for Backfill Materials (Roodi, 2016).

Table 3.2. Size of Course Aggregate (AASHTO M43, 2005).

Size No.	Nominal size square openings	Amounts finer than each laboratory sieve (square openings), percent by weight														
		4	3 1/2	3	2 1/2	2	1 1/2	1	4-Mar	42737	42802	No. 4	No. 8	No. 16	No. 50	No. 100
1	1/2 to 1 1/2	100	90 to 100		25 to 60		0 to 15		0 to 5							
2	2 1/2 to 1 1/2			100	90 to 100	35 to 70	0 to 15		0 to 5							
24	1/2 to 3/4			100	90 to 100		25 to 60		0 to 10	0 to 5						
3	2 to 1				100	90 to 100	35 to 70	0 to 15		0 to 5						
357	2 to No. 4				100	95 to 100		35 to 70		10 to 30		0 to 5				
4	1 1/2 to 3/4					100	90 to 100	20 to 55	0 to 15		0 to 5					
467	1 1/2 to No. 4					100	95 to 100		35 to 70		10 to 30	0 to 5				
5	1 to 1/2						100	90 to 100	20 to 55	0 to 10	0 to 5					
56	1 to 3/8						100	90 to 100	40 to 75	15 to 35	0 to 15	0 to 5				
57	1 to No. 4						100	95 to 100		25 to 60		0 to 10	0 to 5			
6	3/4 to 3/8							100	90 to 100	20 to 55	0 to 15	0 to 5				
67	3/4 to No. 4							100	90 to 100		20 to 55	0 to 10	0 to 5			
68	3/4 to No. 8							100	90 to 100		30 to 65	to 25	0 to 10	0 to 5		

Table 3.2. Size of Course Aggregate (AASHTO M43, 2005) (Cont.).

Size No.	Nominal size square openings	Amounts finer than each laboratory sieve (square openings), percent by weight														
		4	3 1/2	3	2 1/2	2	1 1/2	1	4-Mar	42737	42802	No. 4	No. 8	No. 16	No. 50	No. 100
78	1/2 to No. 8								100	90 to 100	40 to 75	to 25	0 to 10	0 to 5		
8	3/8 to No. 8									100	85 to 100	10 to 30	0 to 10	0 to 5		
89	3/8 to No. 16									100	90 to 100	20 to 55	to 30	0 to 10	0 to 5	
9	No. 4 to No. 16										100	85 to 100	10 to 40	0 to 10	0 to 5	
10	No. 4 to 0										100	85 to 100				10 to 30

3.3.2. Reinforcement Material

Two types of geogrids selected for testing. Properties of geosynthetic materials used in this research are summarized in the following Table 3.3.

Table 3.3. Properties of Test Materials.

	Tensar BX 1100 (GG PP) Biaxial Polypropylene Geogrid	Tensar Triax TX160 (GG PPTG) Triaxial Polypropylene Geogrid
Tensile Strength @ ε=0.5% (lbf/ft) as per ASTM D6637-01 and 4595-11		MD*: 102.9 CD**: 102.9
Tensile Strength @ ε=5% (lbf/ft) as per ASTM D6637-01 and 4595-11 Ultimate Tensile Strength (lbf/ft) as per ASTM D6637-01 and 4595-11	MD: 580 CD: 920 MD: 850 CD: 1300	
Junction Efficiency (%)	MD: 93 CD: 93	MD: 93 CD: 93
Junction Strength (lbf/ft)	MD: 791 CD: 1209	
Aperture Dimensions (inch)	MD: 1.0 CD: 1.3	MD: 1.6 CD: 1.6
Min Rib Thickness (inch)	MD: 0.03 CD: 0.03	MD: 0.06 CD: 0.06
Rib Width (inch)		MD: 0.04 CD: 0.05
*MD: Machine Direction		
**CD: Cross Machine Direction		

3.4. Testing Procedure

Distinct shape, color and size of BSOIL 1 are suitable for image analysis but for sand particles it was not possible to accurately run DIC software from direct images. So, extremely thin translucent latex membrane (0.15 mm thick) is used on the transparent side in order to run image analysis. Membrane is gridded with custom made stamp (0.64 cm x 0.64 cm) and dot patterned to accurately run the Digital Image Correlation. Load cell and LVDT data acquisition are controlled through LabView program. Software

used for camera is DigiCam.

Components of the modified small pullout box are shown in Figure 36:

- Strong small pullout box with stiffened base,
- Side wall with acrylic,
- Stiffened box lid,
- Pressurized-air bladder.

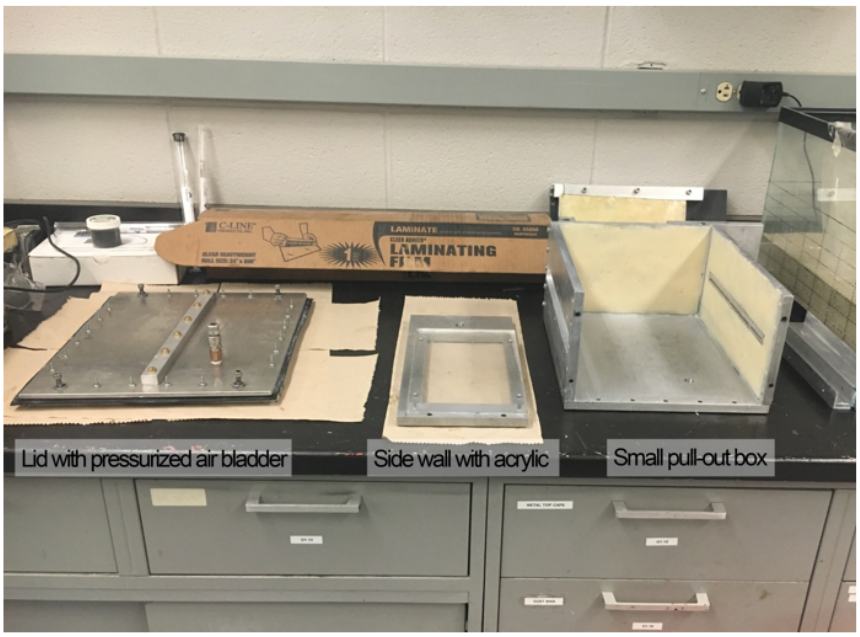

Figure 3.12. Modified Small Pullout Box Components with Acrylic Side Wall.

Final configuration of modified testing procedure is based on small pullout test procedure proposed by Zornberg *et al.*, (2013). Testing procedure is as following:

- Straight geosynthetics specimens are prepared as per the width of the box the day before the test. 30.0 cm wide specimens with 10 ribs used in the testing program.
- Steel wires are attached with hot glue gun to the geosynthetics specimen at five pre-determined junctions. Vertical distances between wires are measured and noted (Figure 3.12).

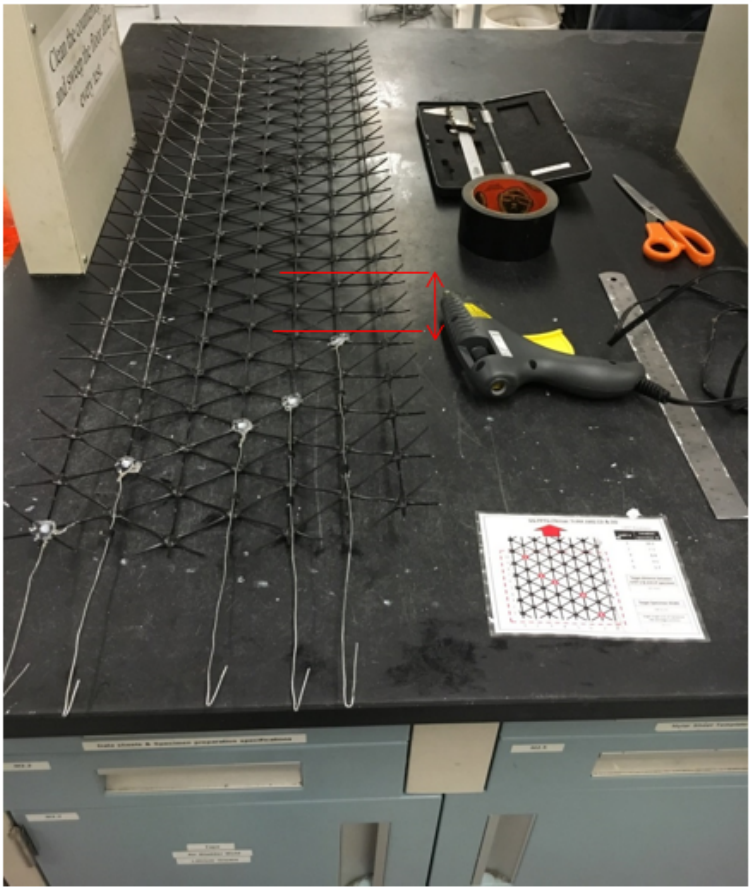

Figure 3.13. Pullout box internal walls.

- Internal side of acrylic is covered with one layer of polyester sheet and internal walls of the box are covered with 2 layers of polyester sheets to minimize the internal friction between the box and the soil as shown in Figure 3.13. Polyester sheets are lithium greased to the internal walls and each other, and sticky polyester sheet is used for acrylic.

- Membrane is prepared and gridded (For sand tests only). Grid is 0.64 cm x 0.64 cm. Thickness of the membrane is 0.15 mm. Grid is inked with custom made stamp. Then, dot pattern is plotted as shown in Figure 3.14. And gridded membrane is Dow Greased on acrylic.

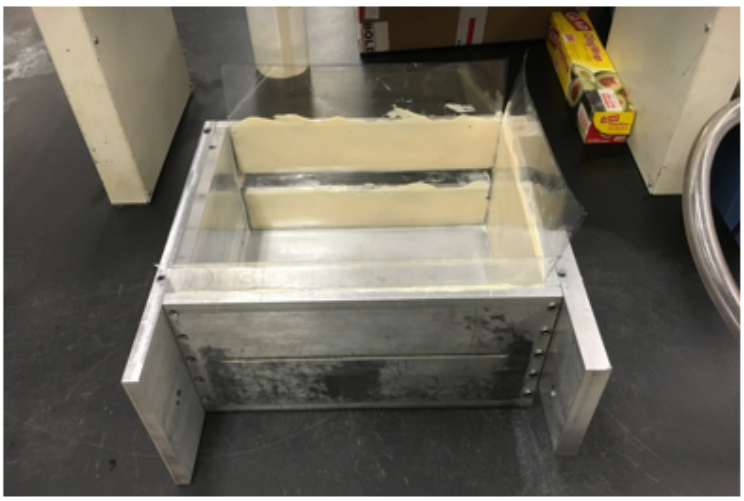

Figure 3.14. Gridded Latex Membrane 0.15 mm.

- Soil is compacted in four layers using Bosch GSH 11E pneumatic hammer pairing with a 15.2 x 15.2 cm. squared head. First two layers are below the geosynthetic specimen and upper two layers are compacted after inserting the geosynthetic specimen. Each layer has a pre-specified mass and height as per the target density, and the compaction is controlled by measuring height of the compacted layer. Compaction via pneumatic hammer in each lift is initially applied on a wooden plate on top of the soil surface. Second stage of compaction for each layer is applied without the wooden plate, one blow on each corner and to the center as shown in Figure 3.15. After each layer is compacted, soil surface is scarified using a blade. Geosynthetic specimen is carefully inserted on top of second compacted layer as shown in Figure 3.15. On top of the soil surface of top layer a nonwoven geotextile is placed in order to protect the air bladder. And the box is closed. BSOIL 2 is placed with moisture content of 1.72% and BSOIL 1 is placed dry. Sand is moistured to impede sand particles from spilling out of the box. Moisture content of sand is in line with Zornberg *et al.*, (2013) procedures: 1.5 $\pm$ 0.3%.

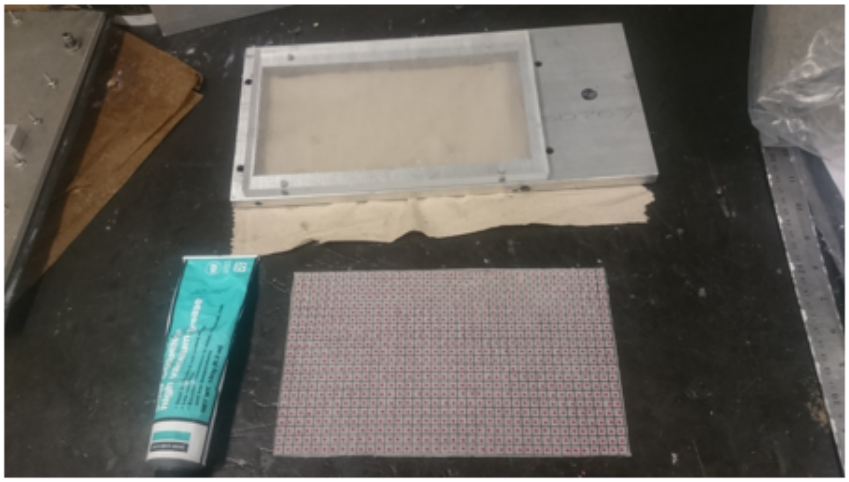

Figure 3.15. Compaction.

- Box is weighted to check the target density. For BSOIL 1, in line with Zornberg *et al.*, (2013), target dry density specified as 1.54 ± 0.04 g/cm^3.

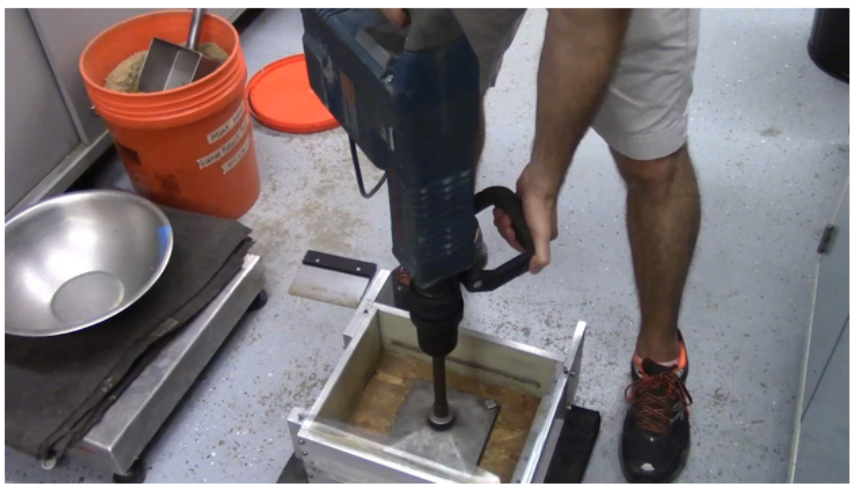

Figure 3.16. Geogrid Inserted through the Rear Wall.

- Overburden (confining) pressure is applied to the box through the air bladder attached to the lid. Pressure is controlled with a digital gauge as seen in Figure 3.17. Accuracy of the gauge is 0.5 kPa. 14kPa (2psi), 21kPa (3psi) and 35kPa (5psi) overburden pressures are applied in testing program. Zornberg *et al.*, (2013) specified 21 kPa confining pressure for small pullout setup as representative of field conditions for base course reinforcement.

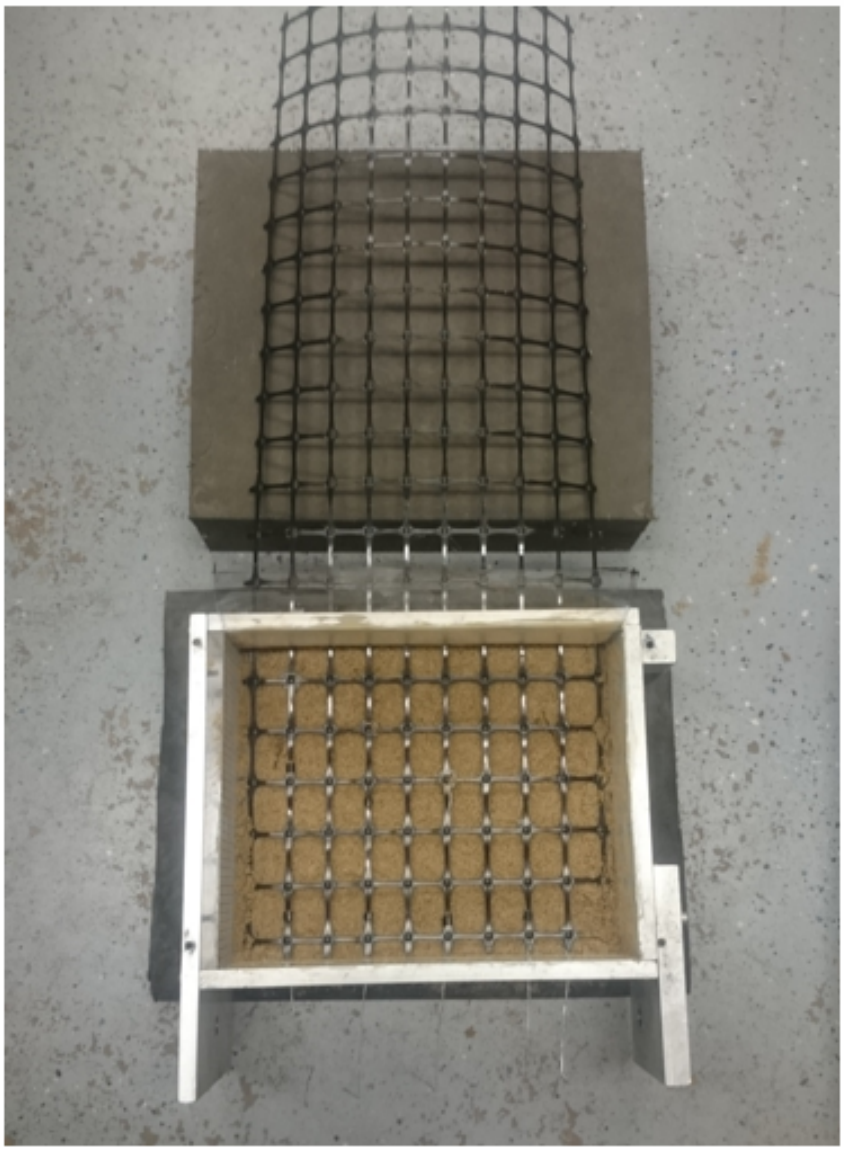

Figure 3.17. Air Pressure Gauge.

- After the overburden pressure is applied, the box is attached on the load frame as shown in Figure 3.18 and geosynthetic specimen is attached to the roller grip. Wires are attached to the LVDTs to measure the displacement along the geosynthetic specimen throughout the pullout test. Rear wall of the box has 4.00 mm wide slot at the middle of the box, allowing the use of wires.

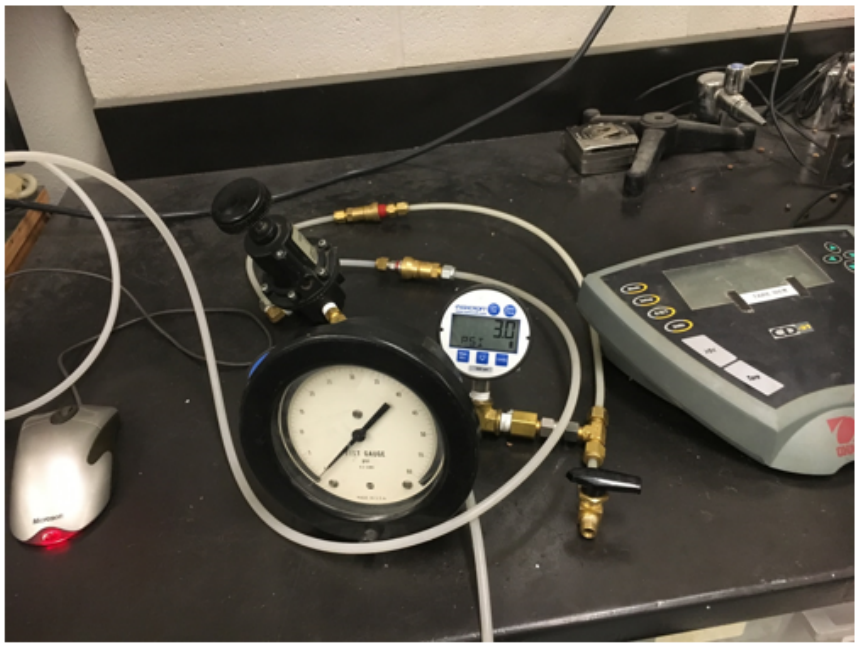

Figure 3.18. Box Mounted on the Frame and LVDTs attached.

- Camera is set upped and focus of the lens is fixed as seen in Figure 3.19. Frequency of image capturing is set at 1 image per minute. The images were captured with Nikon Digital SLR Camera D5200 camera.
- Preloading is applied about 30lbf (0.15kN) before running the test.
- Labview is checked and pullout test is started.
- Rate of the test is constant with a displacement of 1 mm/min (clamp speed).
- Test is run up to pullout failure observed.
- Both pullout data and image analysis data are acquired at the end of the test.

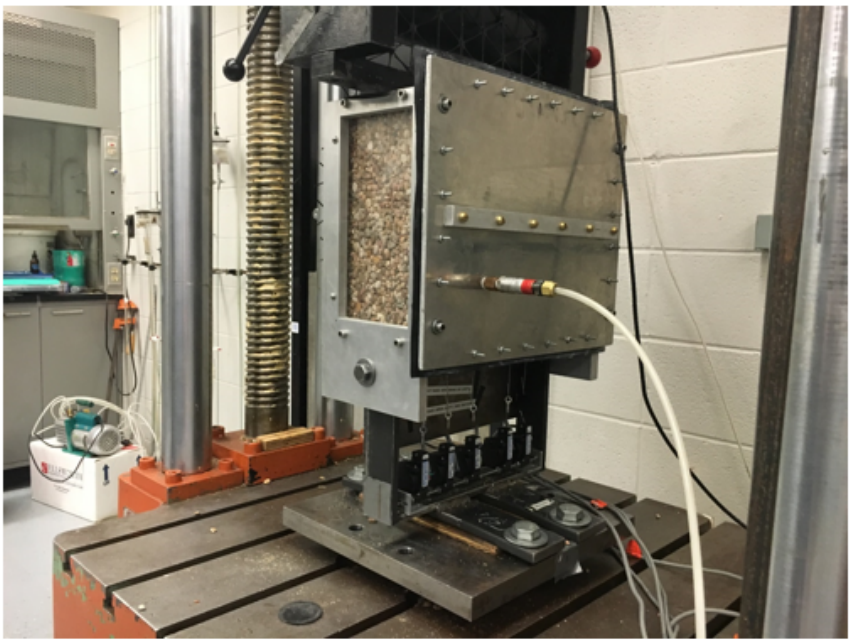

Figure 3.19. Small Pullout Test Final Setup.

3.5. Axial Displacements and K_{SGI} Calculations via LVDT Measurements

Voltages obtained from data acquisition system are converted and stored via LabView program. Coefficient of Soil - Geosynthetic Interaction (K_{SGI}) is calculated for each test. Zornberg *et al.*, (2012) procedure is followed for calculation of K_{SGI} which corresponds to one regression line obtained from LVDTs 2, 3 and 4 which eliminates the boundary affects and reflects the interface stiffness of the central portion. K_{SGI} is an index the slope of a linear relationship between reinforcement displacement and the square of the unit tension at along the active length.

3.6. Image Analysis Procedure

An open source Digital Image Correlation and Tracking with MATLAB code by Senn and Eberl (2016) is used in this research. Code tracks the intensity value of averaged pixels corresponding to markers. Image Analysis procedure applied in the calculations are as follows:

- Initially all the images are cropped from same reference points and converted into 8-bit greyscale tiff image via ImageJ as shown in Figure 45. For the easiness and consistency of the analysis, images are cropped from reference points dotted on the pullout box. Even though it doesn't fully represent the color image, 8-bit image is used for faster computation.

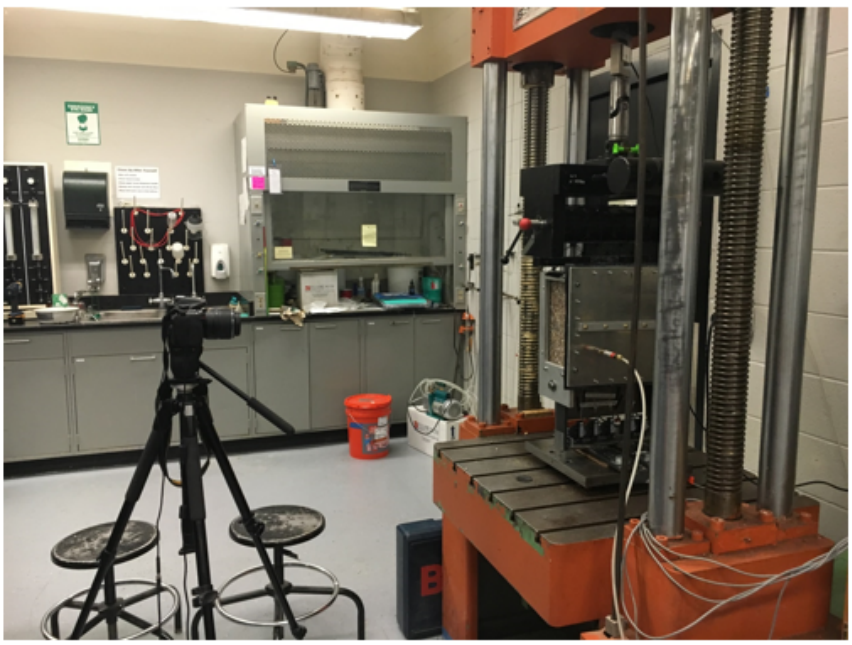

Figure 3.20. Cropping Image with Image.

Digital Image Correlation and Tracking algorithm has two methods to run image analysis. First method is called peak tracking which traces peculiar intensity components of the markers such as bright round spots on dark background. The other method is processing correlations for fixed grid of markers (grid nodes) defined at the initial stage of the analysis. In this study "process correlations" method is used. The outputs of the analysis are validx and validy data which contains positon of markers for each analyzed image. In order to run the algorithm images should be 8 bit greyscale tiff format. Algorithm of the software is depicted in Figure 3.21.

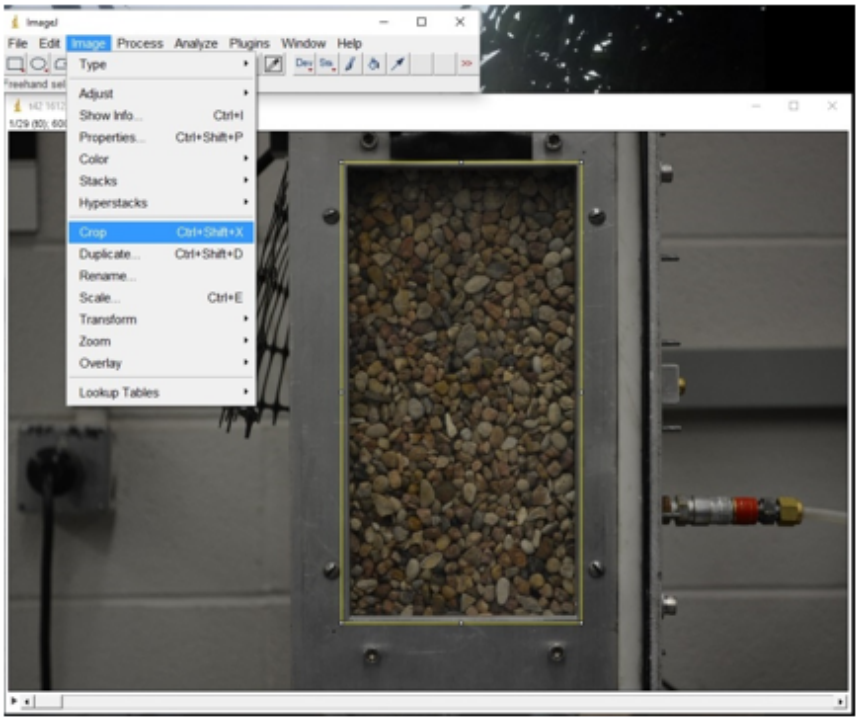

Figure 3.21. Digital Image Correlation ant Tracking Algorithm (Senn and Eberl, 2016).

- Digital Image Correlation is done via MatLab using commands of the main window as seen in Figure 3.22.

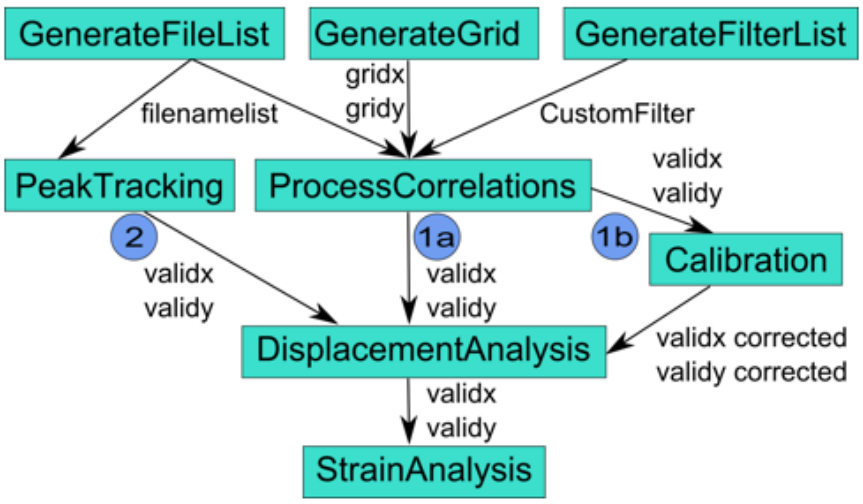

Figure 3.22. Digital Image Correlation and Tracking MatLab Main Window.

- Grid is defined as shown in Figure 3.22 with determined pixel resolution on the based image and the same grid applied to each and every image in the analysis .

The finer grid will give more accurate results.

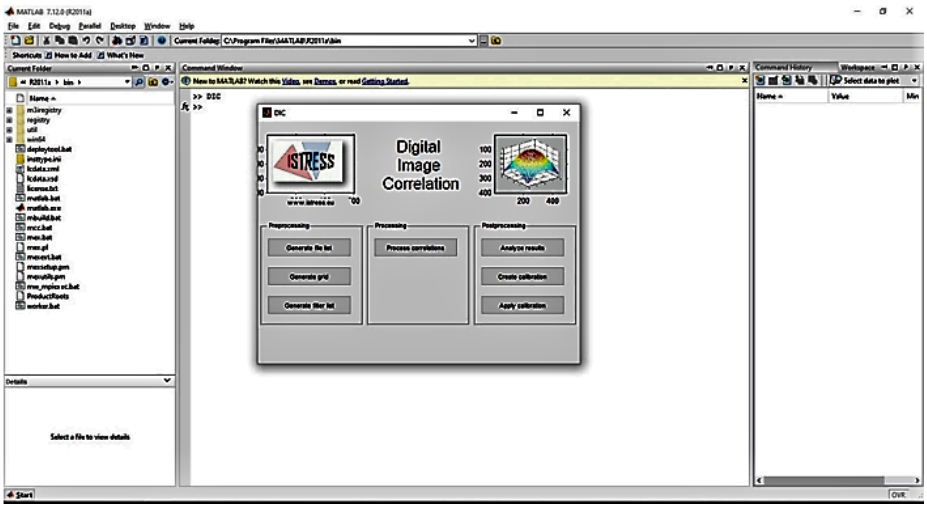

Figure 3.23. Gridding with 25 x 25 pixel resolution.

- Images are gridded as shown in Figure 3.24.

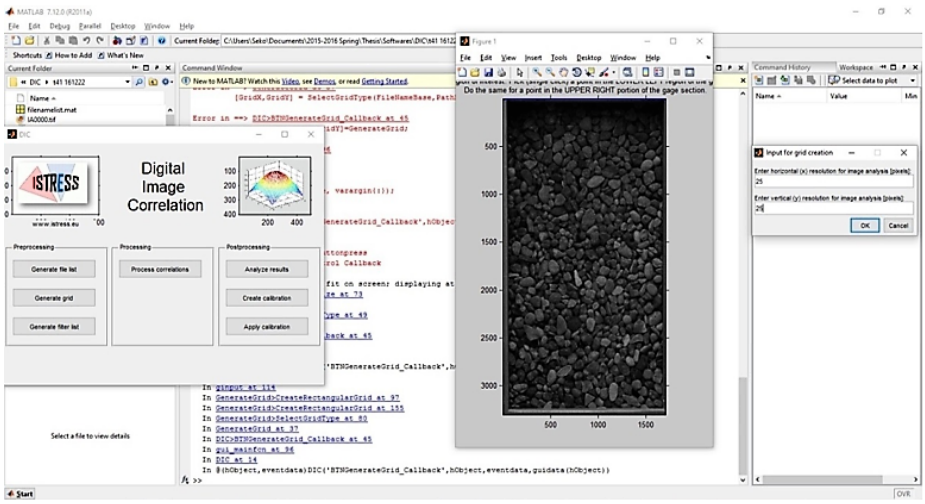

Figure 3.24. Gridded Image.

After the grid is defined, displacement analysis run and each and every image are processed. Correlation of all markers is calculated at this process. Markers of the base image are correlated with each image.

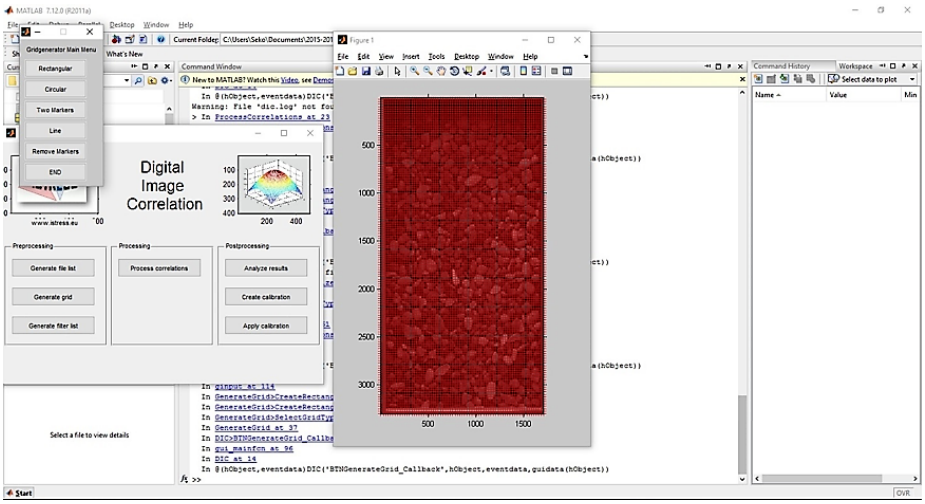

Figure 3.25. Processing Images.

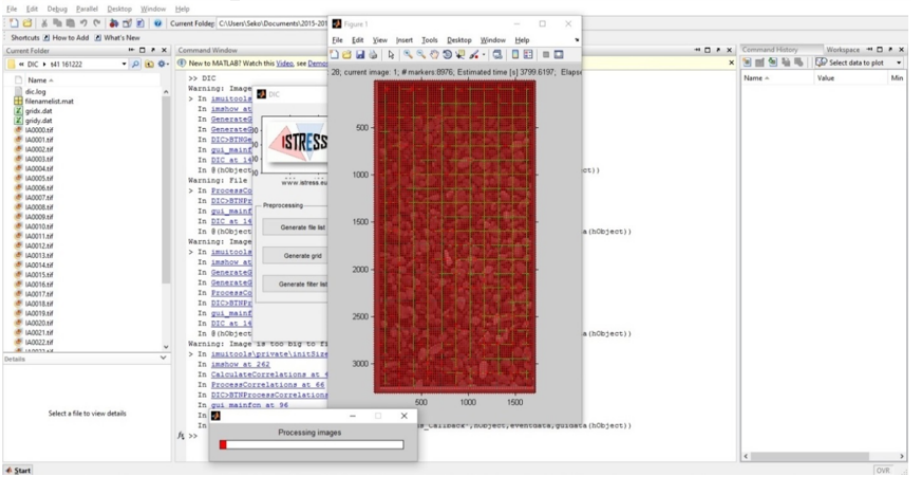

Figure 3.26. Markers on Image 1 Test # 160314.

- Markers are located on the image as per the grid. Figure 3.27 marker points on the first image being processed (Figure 3.25).
- Analyze screen helps to visualize the processed outputs in MatLab as shown in Figure 3.28). Also the x and y coordinates of each marker in every image is exported to excel.

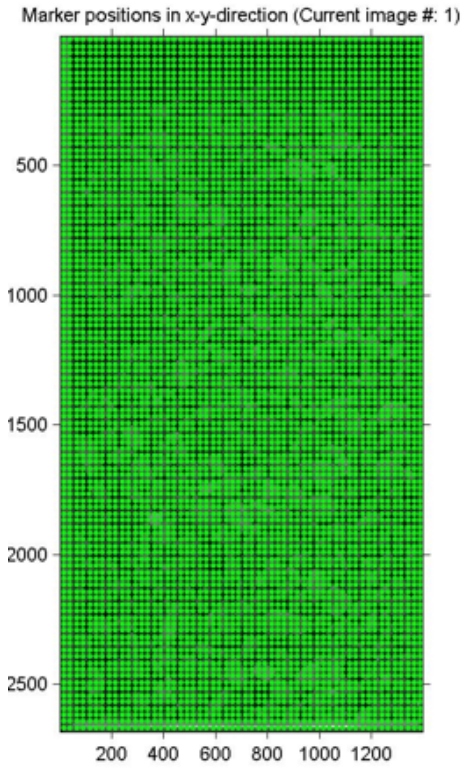

Figure 3.27. Markers on Image 18 at time LVDT3 @3mm #160314.

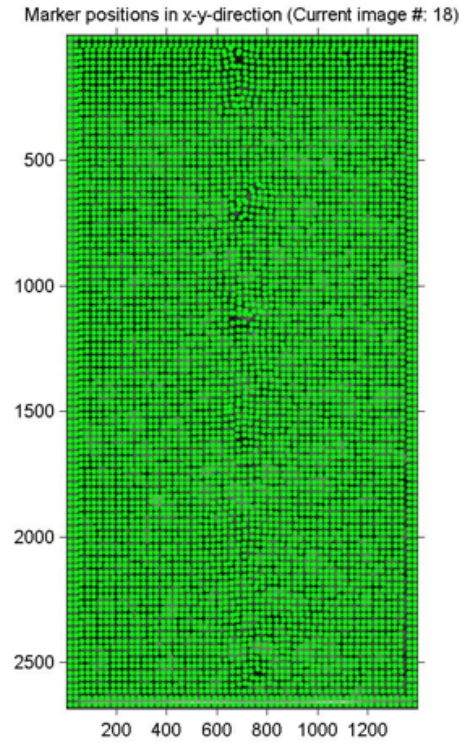

Figure 3.28. Markers on Image 18 at time LVDT3 @3mm #160314.

- Outputs of DIC Code are exported to excel and corresponding axial displacements in millimeters are calculated for each image analyzed. Conversion of pixels to millimeters is calculated with referencing the dimensions of the inner side wall of the acrylic side wall.
- Finally we get the matrix of axial displacement values for each image based on the initial image.
- Then image corresponding to nearest time to 1 mm, 2 mm, and 3 mm displacement of LVDT 3 is selected, as shown in Table 3.4, to represent the shear band thickness.

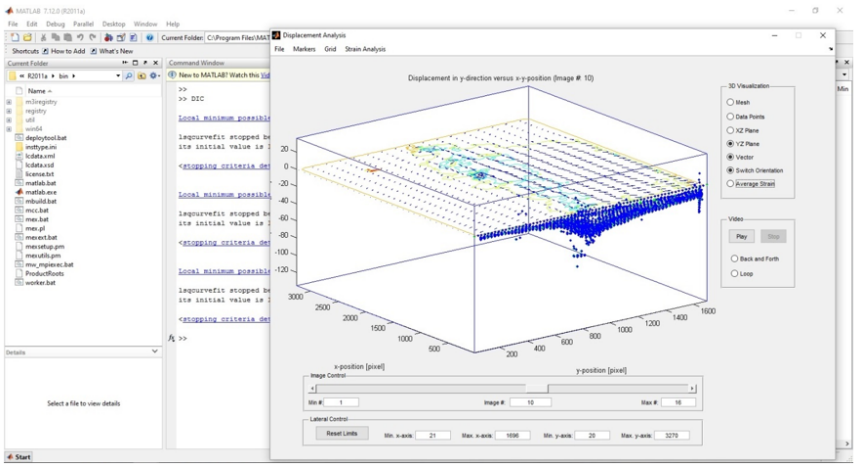

Figure 3.29. 3D Visualization of Displacements.

Table 3.4. Setup, Data Acquisition and Imaging.

Test Setup	LVDT & Pullout Load Data	Imaging
Preparation		
	Data acquisition starts	Imaging Starts
Start of the Test		Image 1
		Image 2
		Image 3
		.
		.
		.
	LVDT 3 reaches 1,2,3 mm displacement	Image n .
End of the Test		.
	Data acquisition ends	Imaging Ends

3.7. Testing Matrix

Main test parameters are as below Table 3.5:

Table 3.5. Final Test Configurations.

Test #	Backfill Soil	Geosynthetic	Geosynthetic Width	Pullout Direction	Overburden Pressure
160314	BSOIL 1	GG PP	30 cm	CD	35 kPa
160316	BSOIL 1	GG PP	30 cm	CD	21 kPa
160321	BSOIL 1	GG PP	30 cm	CD	14 kPa
160408	BSOIL 2	GG PP	30 cm	CD	14kPa
160413	BSOIL 2	GG PPTG	30 cm	CD	21kPa
160421	BSOIL 1	GG PPTG	30 cm	CD	21 kPa

4. RESULTS AND DISCUSSIONS

This chapter investigates firstly the results obtained from Data Acquisition system which correlates with pullout force and axial displacement of LVDTs. On top of pullout analysis, Image Analysis is conducted to capture the complete mechanism of shear bands. Results of pullout tests are consistent within the group of tests and are in line with theory. Image analysis results are complying with the literature review and forming the basis for qualitative analysis of the shear band mechanism under different parameters.

In first part of this Chapter (4.1); typical values obtained from pullout tests are presented to assure the credibility of the tests performed with modified small pullout box.

In the second part (4.2); to make a fair comparison of shear band thickness among different tests, pre-determined variables should be selected. These variables can be load at pullout failure, pre-determined pullout load, pre-determined frontal displacement or pre-determined displacement of an LVDT.

For this study axial displacement values of soil particles on transparent side measured via Image Analysis are compared at the time nearest to LVDT 3 showing 1.00, 2.00 and 3.00 mm displacements, as described in methodology. LVDT 3 is selected because it measures the axial displacement at central portion of the geosynthetic specimen. And three different axial displacement values are selected to have a better understanding of the propagation of shear band. Similar to Lesniewska *et al.*, (2012), mean value between maximum and minimum axial displacement is selected as threshold to define boundaries of shear band. Both, normalized (thresholding applied) and nominal axial displacement values are investigated.

4.1. Pullout Test Results

Pullout Test results are summarized in the below Table 4.1.

Table 4.1. Pullout Test Summary.

Test #	Max Pullout Load (kN)	75% Max Load (kN)	Load at LVDT3 1mm (kN)	Load at LVDT3 2mm (kN)	Load at LVDT3 3mm (kN)	K_{SGI} $(kN/m)^2$
160314	2.86	2.15	2.22	2.51	2.63	19.7
160421	2	1.5	1.45	1.66	1.85	8.9
160316	1.87	1.4	1.35	1.57	1.74	9.1
160413	1.57	1.18	1.44	1.64	1.65	6.5
160321	1.21	0.91	1.02	1.15	1.24	3.8
160408	1.01	0.76	1.03	1.05	1.1	2.5

Max pullout load (kN); is the exact load at which pullout failure is occurred in other words the largest load that geogrid specimen could bear without yielding.

Front Pullout Force (kN/m); is the force measured by dividing width of the specimen to the pullout load (measured by load cell attached to the front of the box).

75% max load (kN); is 75% of max pullout load Load at LVDT 3 at pre-determined displacement (kN); is the load at which the axial displacement of LVDT3 is reached a pre-determined displacement (mm).

K_{SGI} corresponds to one regression line obtained from LVDTs 2, 3 and 4 which eliminates the boundary affects and reflects the interface stiffness of the central portion.

Results of pullout test are investigated group by group below.

Table 4.2. Backfill Soil Type vs Max Pullout for GG PP.

Test #	Backfill Soil	Geosynthetic	Geosynthetic Width	Pullout Direction	Overburden Pressure	Max Pullout (kN)
160321	BSOIL 1	GG PP	30 cm	CD	14 kPa	1.21
160408	BSOIL 2	GG PP	30 cm	CD	14kPa	1.01

Test results presented in Table 4.2 are consistent with the theory; BSOIL 1 has higher interface shear resistance compared to BSOIL 2. Backfill soil type has a significant effect on pullout resistance as expected. The more the average particle size and friction angle of the backfill soil the higher the pullout resistance.

Table 4.3. Geosynthetic Type vs Max Pullout.

Test #	Backfill Soil	Geosynthetic	Geosynthetic Width	Pullout Direction	Overburden Pressure	Max Pullout (kN)
160421	BSOIL 1	GG PPTG	30 cm	CD	21 kPa	2
160413	BSOIL 2	GG PPTG	30 cm	CD	21kPa	1.57

Test results are presented in Table 4.4 are consistent with the theory, BSOIL 1 has higher interface shear resistance compared to BSOIL 2. Backfill soil type has a significant effect on pullout resistance as expected. The more the average particle size and friction angle of the backfill soil the higher the pullout resistance.

Table 4.4. Geosynthetic Type vs Max Pullout.

Test #	Geosynthetic	Backfill Soil	Geosynthetic Width	Pullout Direction	Overburden Pressure	Max Pullout (kN)
160316	GG PPTG	BSOIL 1	30 cm	CD	21 kPa	2
160421	GG PP	BSOIL 1	30 cm	CD	21 kPa	1.87

Tests results shown in Table 4.5 shows that GG PPTG has higher pullout resistance compared to GG PP under same test conditions, as expected. Both products are

polypropylene geogrids, but rib width and thickness are higher in GG PPTG leading to a larger surface area interaction between soil and geogrid.

Table 4.5. Overburden Pressure Type vs Max Pullout for GG PP.

Test #	Overburden Pressure	Backfill Soil	Geosynthetic	Geosynthetic Width	Pullout Direction	Max Pullout (kN)
160314	35 kPa	BSOIL 1	GG PP	30 cm	CD	2.86
160316	21 kPa	BSOIL 1	GG PP	30 cm	CD	1.87
160321	14 kPa	BSOIL 1	GG PP	30 cm	CD	1.21

Overburden pressure affects both frictional and bearing resistance of the soil-geogrid interface. Overburden (confining) pressure has significant impact on the pullout resistance as the normal effective and bearing effective stresses change under different overburden pressures. Results presented in Table 4.5 show that larger overburden pressure leads to a higher pullout resistance, as expected.

K_{SGI} and Frontal Pullout Force comparisons are complying with max pullout load comparisons, which:

- Frontal pullout force and K_{SGI} were higher at higher confining pressures due to change in normal effective stress and bearing effective stress.
- Frontal pullout force and K_{SGI} were higher at BSOIL 1 compared to BSOIL 2, because shear interaction is more intensive BSOIL 1 and the geogrid as compared to BSOIL 2 and the geogrid.
- Frontal pullout force and K_{SGI} were higher at GG PPTG compared to GG PP, because geometry of GG PPTG imposes stiffer structure.

These results were expected because knowing that all test run with same specimen width, behavior of K_{SGI} and Frontal Pullout Force would be same with pullout load. Displacement curves and K_{SGI} plots for each test are presented below.

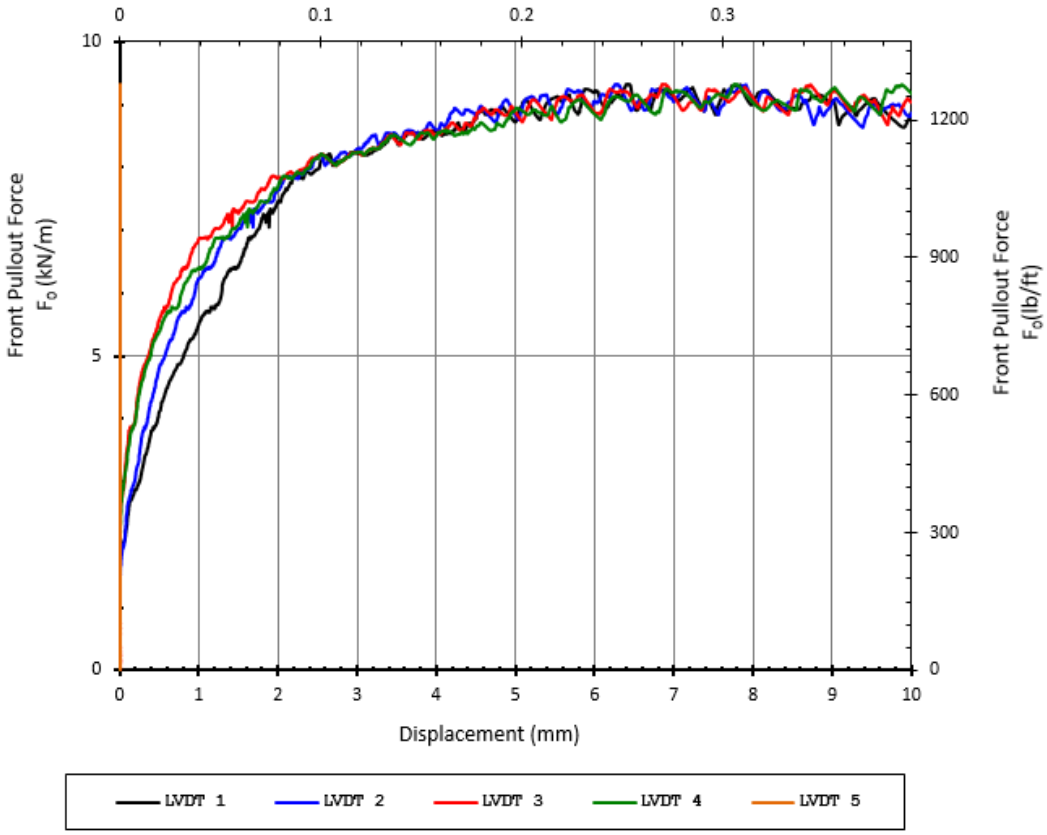

Figure 4.1. Pullout Force vs Displacement Curve for Test with BSOIL 1, GG PP, 35 kPa (#160314).

As seen in Figure 4.1, progressive mobilization of LVDTs was observed. LVDT 5 was mobilized first because it is nearest LVDT to the front side of the box whereas LVDT 1 was mobilized last which is located near bottom part of the box. Max front pullout force was measured as 9.3 kN/m.

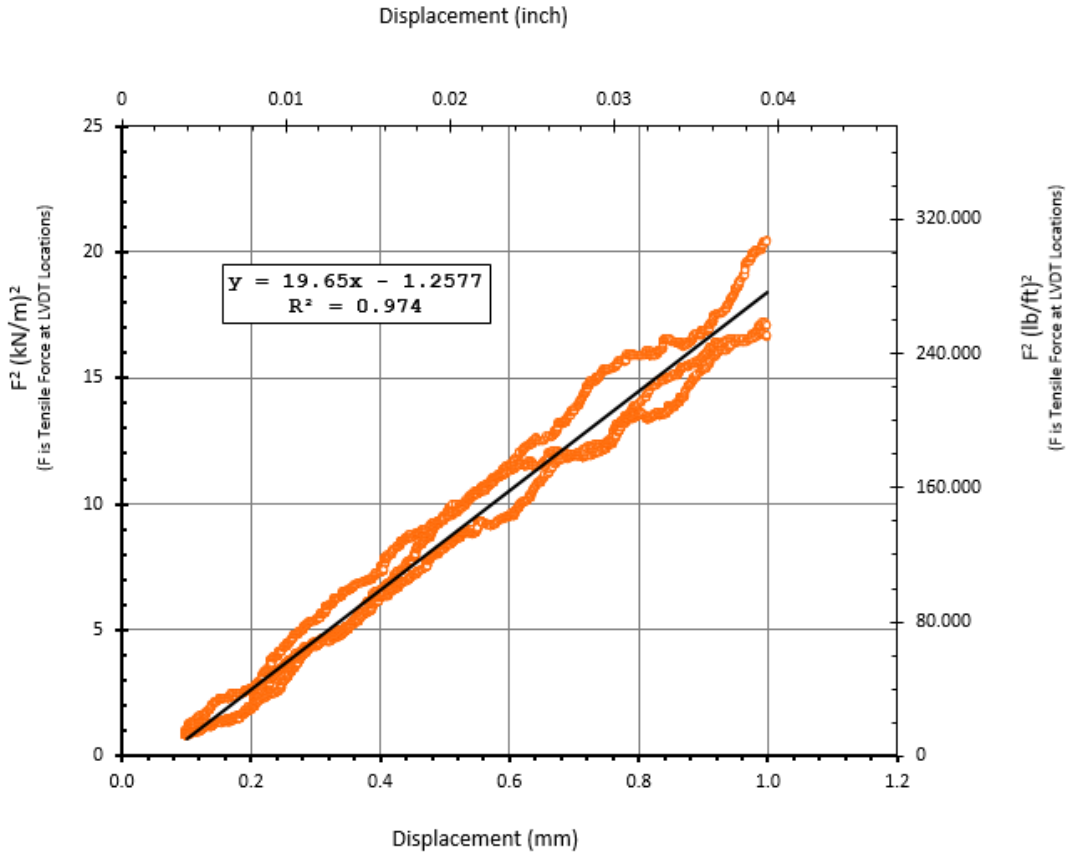

Figure 4.2. K_{SGI} Plot for Test with BSOIL 1, GG PP, 35 kPa (#160314).

As seen in Figure 4.2, K_{SGI} value of 19.65 kN^2/m^2, representing interface stiffness of the central portion, was calculated with 97.4% goodness of fit, using measurement values of LVDT 2, LVDT 3 and LVDT 4.

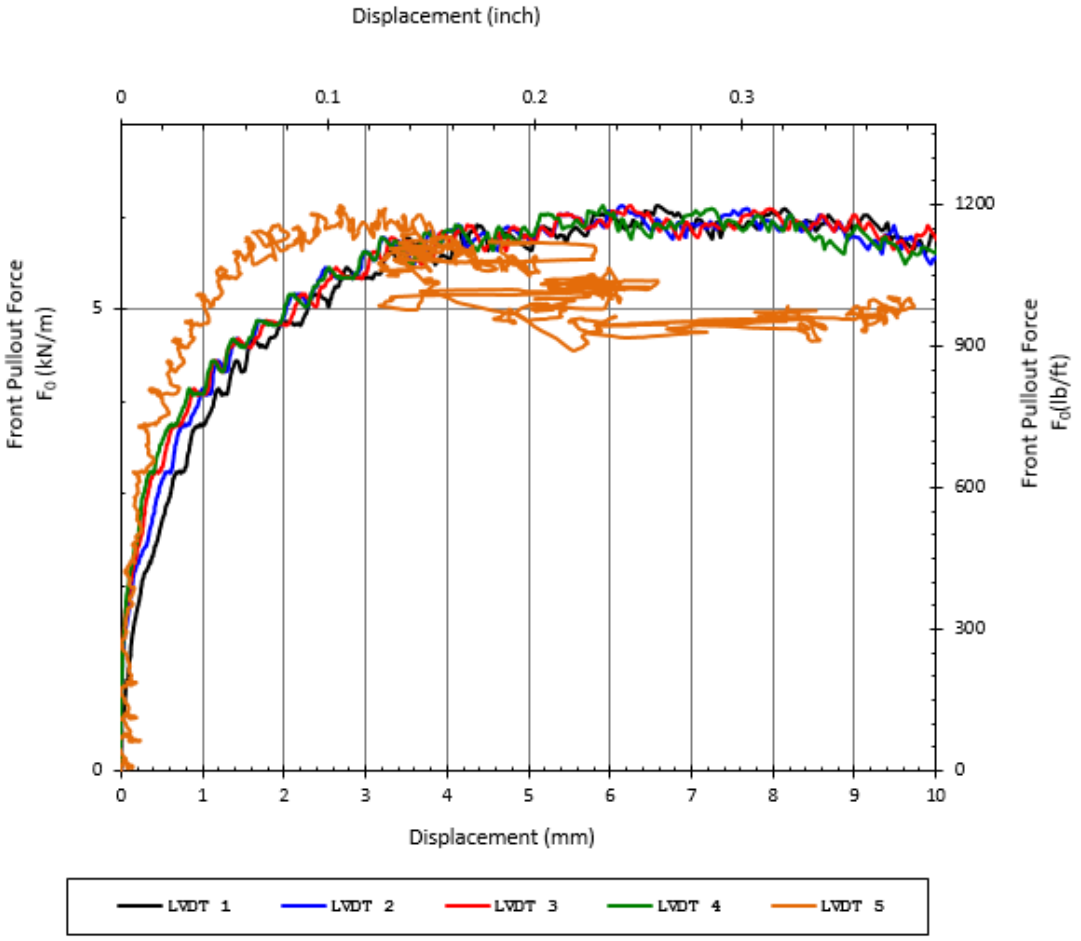

Figure 4.3. Pullout Force vs Displacement Curve for Test with BSOIL 1, GG PP, 21 kPa (#160316).

As seen in Figure 4.3, progressive mobilization of LVDTs was observed. LVDT 5 showed irregular pattern possibly due to misconnection of the wire to the LVDT. LVDT 1 was mobilized last which is located near bottom part of the box. Max front pullout force was measured as 6.1 kN/m.

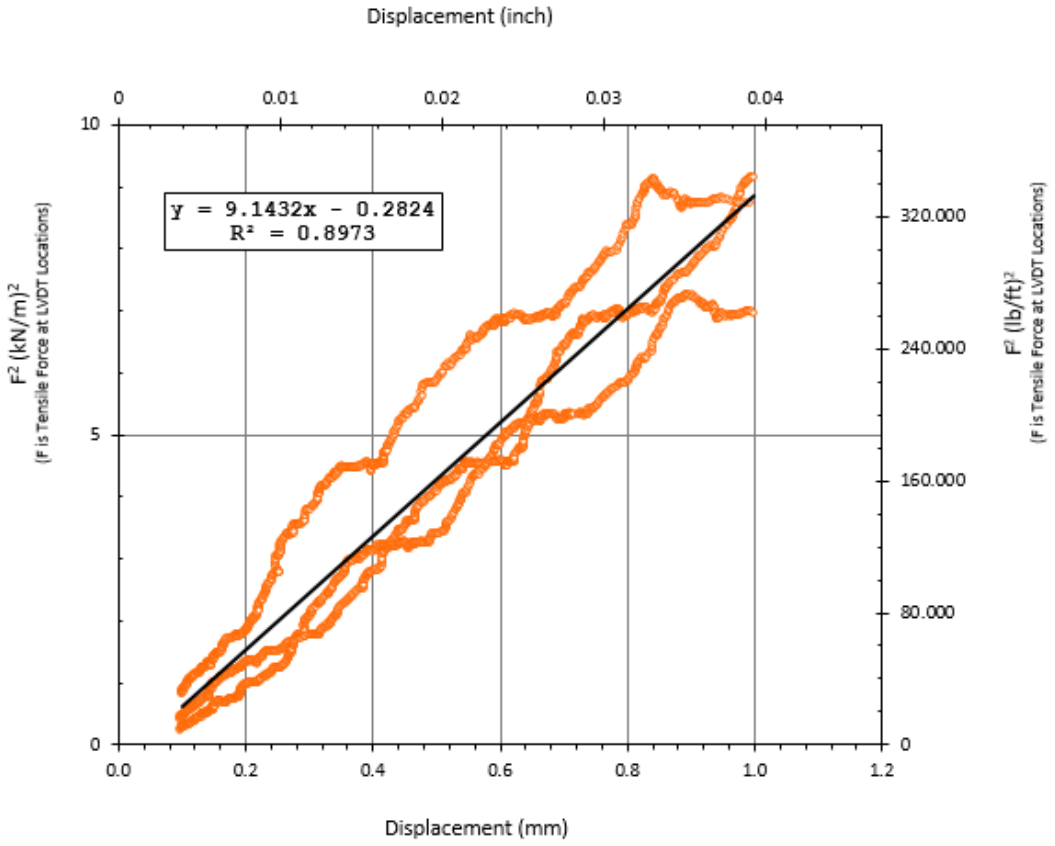

Figure 4.4. K_{SGI} Plot for Test with BSOIL 1, GG PP, 21 kPa (#160316).

As seen in Figure 4.4, K_{SGI} value of 9.14 kN^2/m^2, representing interface stiffness of the central portion, was calculated with 89.7% goodness of fit, using measurement values of LVDT 2, LVDT 3 and LVDT 4.

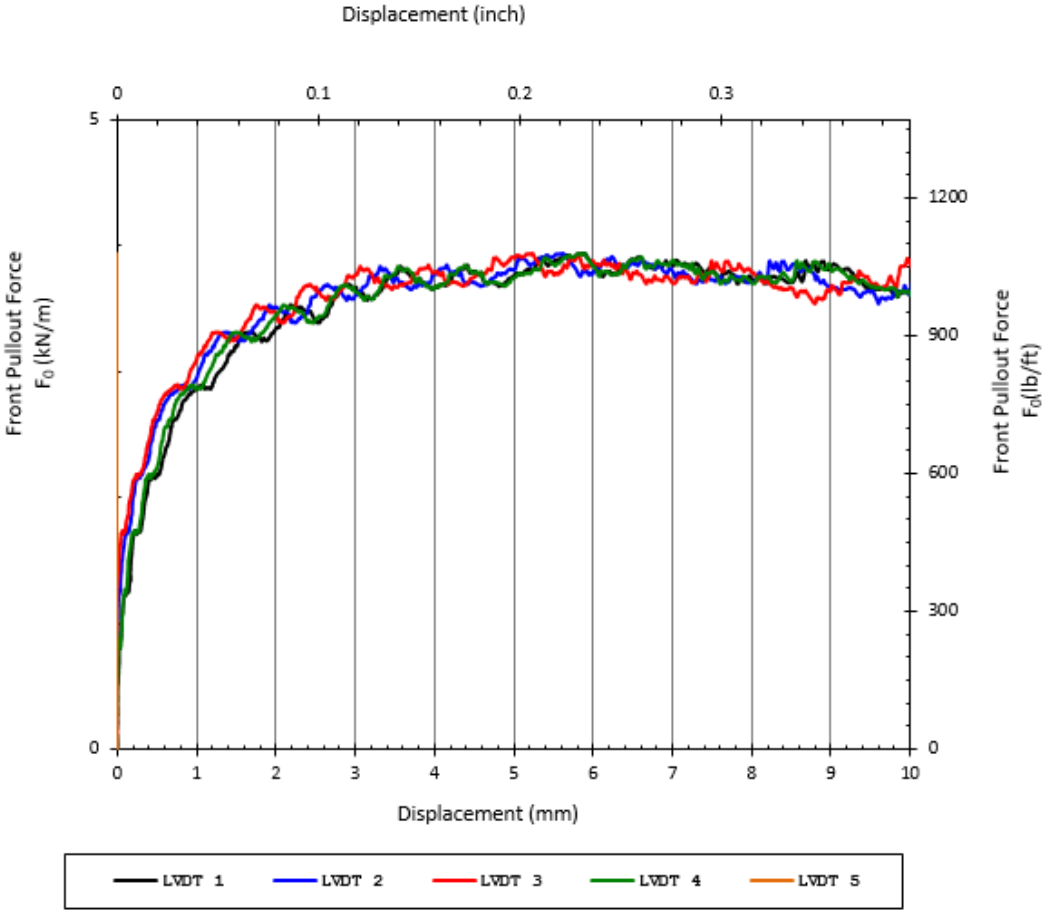

Figure 4.5. Pullout Force vs Displacement Curve for Test with BSOIL 1, GG PP, 14 kPa (#160321).

As seen in Figure 4.5, progressive mobilization of LVDTs was observed. LVDT 5 was mobilized first because it is nearest LVDT to the front side of the box whereas LVDT 1 was mobilized last which is located near bottom part of the box. Max front pullout force was measured as 3.9 kN/m.

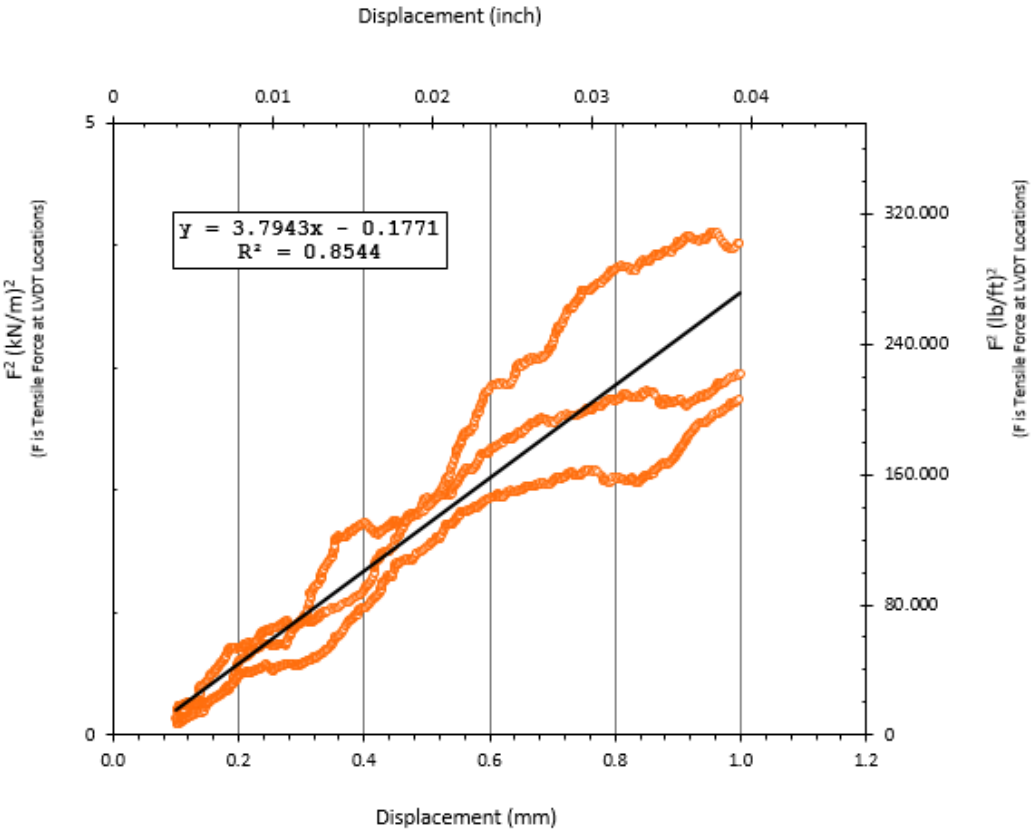

Figure 4.6. K_{SGI} Plot for Test with BSOIL 1, GG PP, 14 kPa (#160321).

As seen in Figure 4.6, K_{SGI} value of 3.79 kN^2/m^2, representing interface stiffness of the central portion, was calculated with 85.4% goodness of fit, using measurement values of LVDT 2, LVDT 3 and LVDT 4.

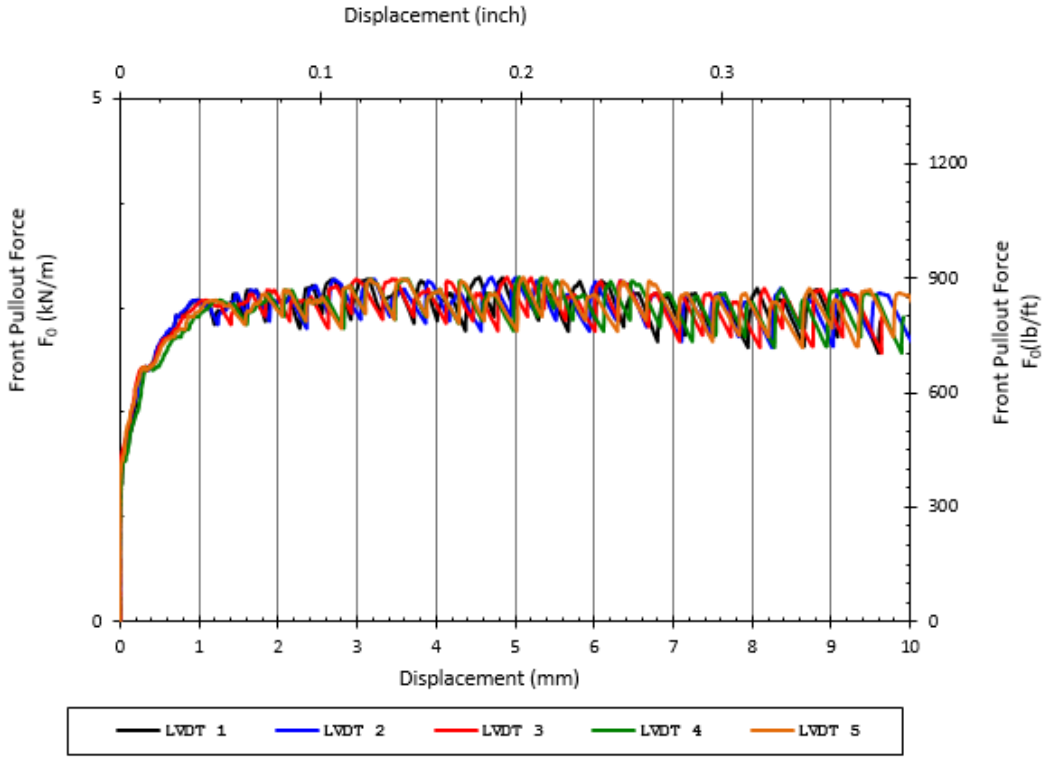

Figure 4.7. Pullout Force vs Displacement Curve for Test with BSOIL 2, GG PP, 14kPa (#160408).

As seen in Figure 4.7, progressive mobilization of LVDTs was observed. LVDT 5 was mobilized first because it is nearest LVDT to the front side of the box whereas LVDT 1 was mobilized last which is located near bottom part of the box. Max front pullout force was measured as 3.3 kN/m.

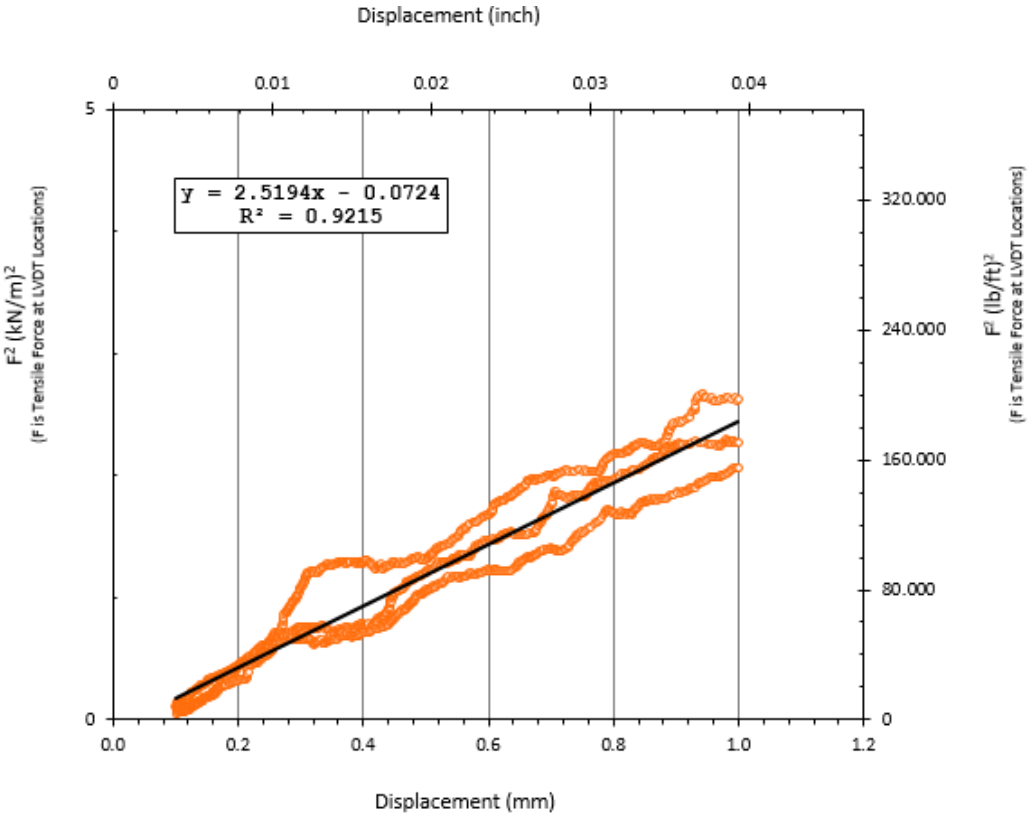

Figure 4.8. K_{SGI} Plot for Test with BSOIL 2, GG PP, 14kPa (#160408).

As seen in Figure 4.8, K_{SGI} value of 2.51 kN^2/m^2, representing interface stiffness of the central portion, was calculated with 92.1% goodness of fit, using measurement values of LVDT 2, LVDT 3 and LVDT 4.

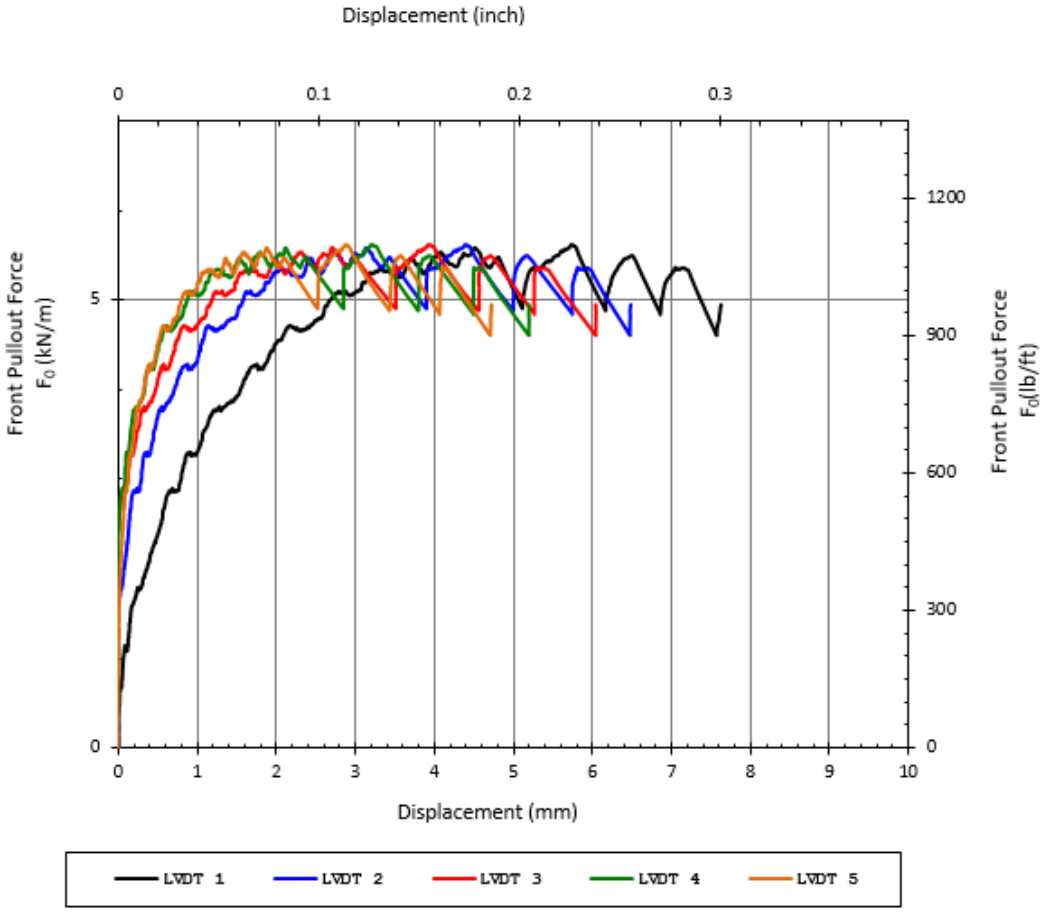

Figure 4.9. Pullout Force vs Displacement Curve for Test with BSOIL 2, GG PPTG, 21kPa (#160413).

As seen in Figure 4.9, progressive mobilization of LVDTs was observed. LVDT 5 was mobilized first because it is nearest LVDT to the front side of the box whereas LVDT 1 was mobilized last which is located near bottom part of the box. Max front pullout force was measured as 5.6 kN/m.

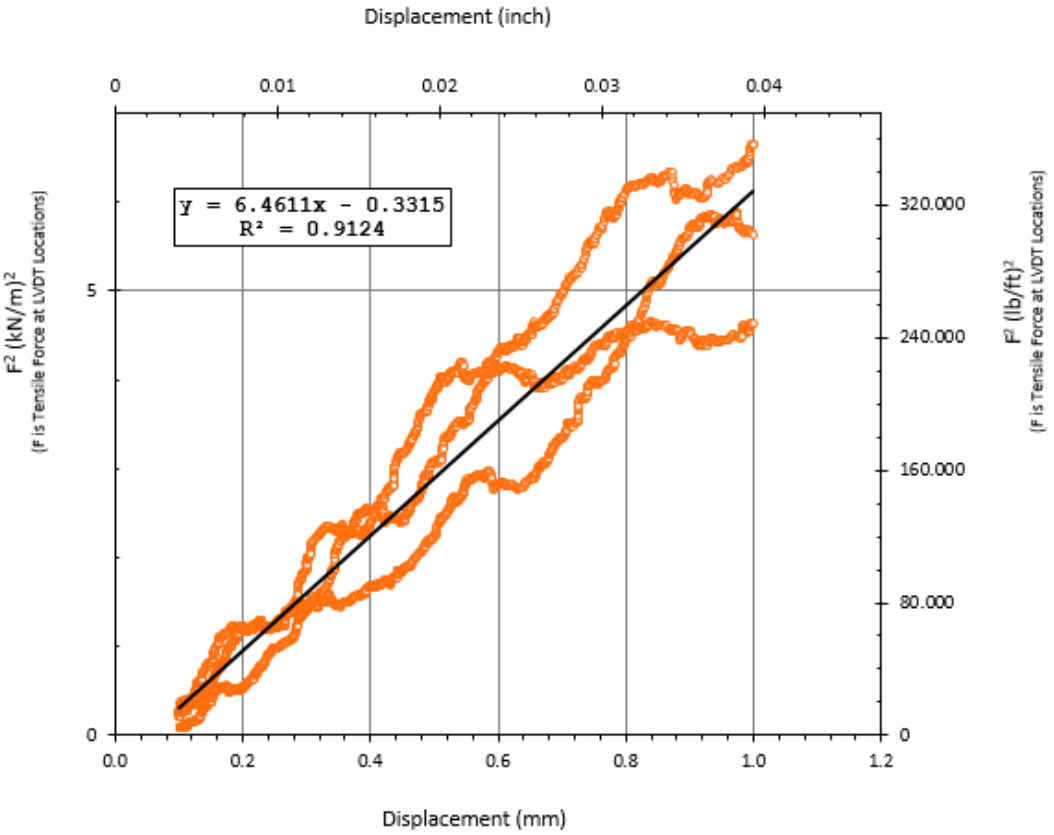

Figure 4.10. K_{SGI} Plot for Test with BSOIL 2, GG PPTG, 21kPa (#160413).

As seen in Figure 4.10, K_{SGI} value of 6.46 kN^2/m^2, representing interface stiffness of the central portion, was calculated with 91.2% goodness of fit, using measurement values of LVDT 2, LVDT 3 and LVDT 4.

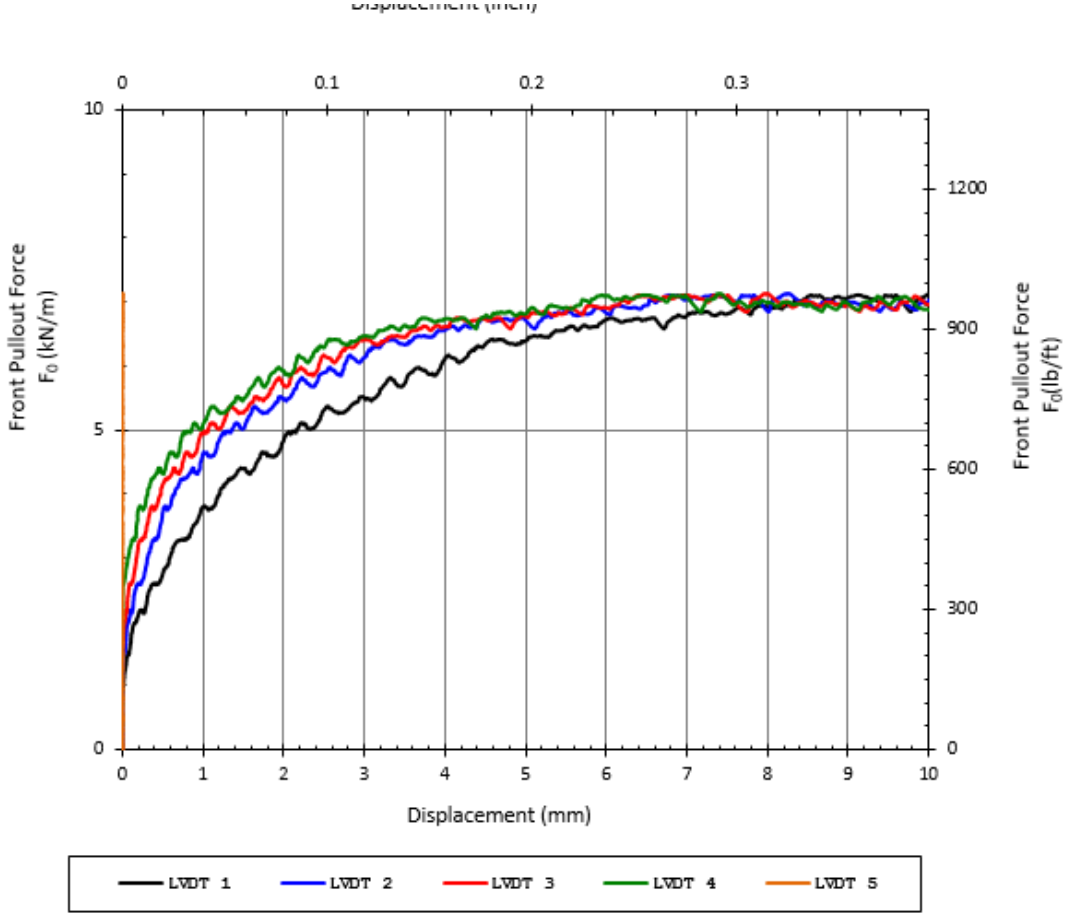

Figure 4.11. Pullout Force vs Displacement Curve for Test with BSOIL 1, GG PPTG, 21 kPa (#160421).

As seen inFigure 4.11, progressive mobilization of LVDTs was observed. LVDT 5 was mobilized first because it is nearest LVDT to the front side of the box whereas LVDT 1 was mobilized last which is located near bottom part of the box. Max front pullout force was measured as 7.1 kN/m.

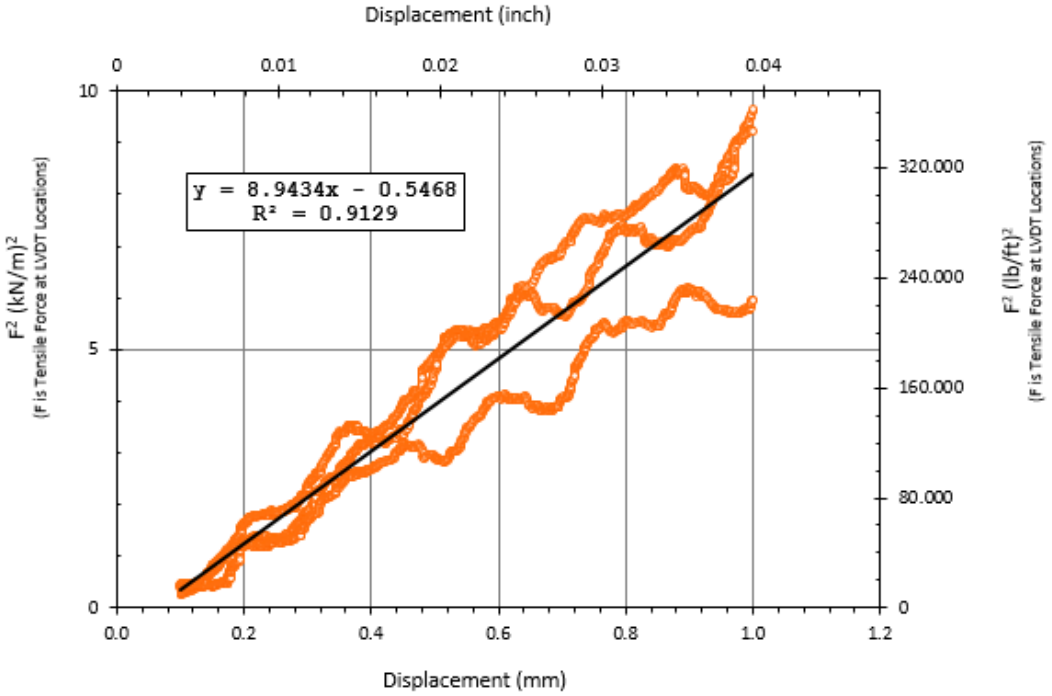

Figure 4.12. K_{SGI} Plot for Test with BSOIL 1, GG PPTG, 21 kPa (#160421).

As seen in Figure 4.12, K_{SGI} value of 8.94 kN^2/m^2, representing interface stiffness of the central portion, was calculated with 91.2% goodness of fit, using measurement values of LVDT 2, LVDT 3 and LVDT 4.

4.2. Image Analysis Results

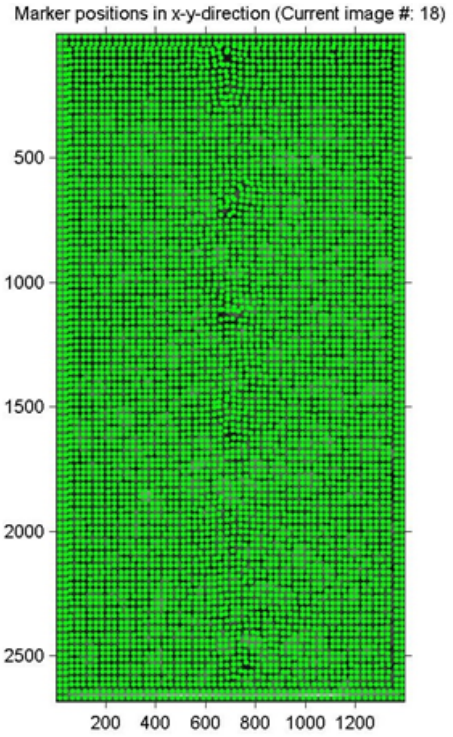

Figure 4.13. Test with BSOIL 1, GG PP, 35 kPa (#160314) LVDT3 at 3mm.

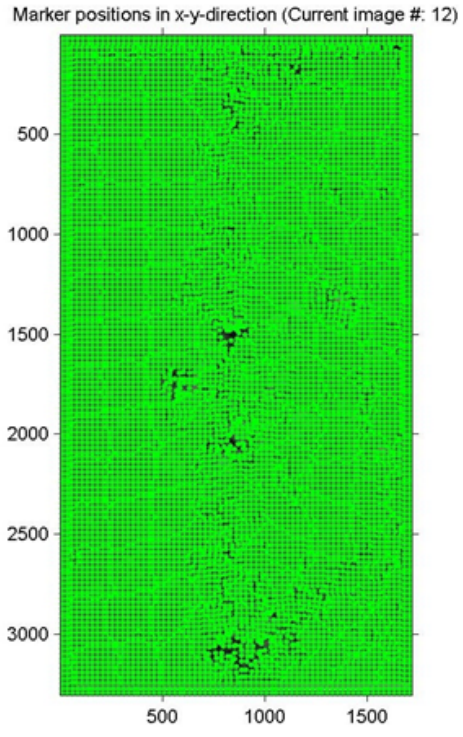

Figure 4.14. Test with BSOIL 1, GG PP, 21 kPa (#160316) LVDT3 at 3mm.

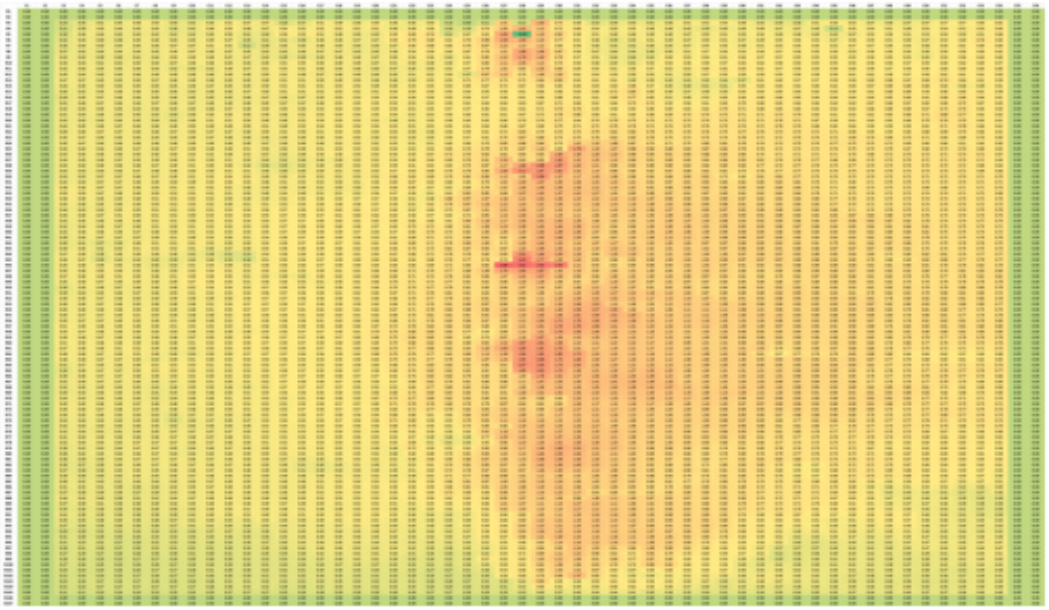

Figure 4.15. Excel Spreadsheet of Axial Displacement Values with Color Scale Conditional Formatting.

Figure 4.13 and Figure 4.15 are output of the same image analyzed in different software, Excel and Matlab respectively. From excel spreadsheet it is easier to see where the maximum axial displacement has placed. For every image processed, excel spreadsheet is prepared which includes axial displacement values for each marker on the grid. Red colored cells in Figure 4.15 spreadsheet corresponds to maximum value within the cells in the matrix, and green color represents lowest value (zero). So the green colored cells in Figure 4.15 corresponds markers on the walls of the transparent side of the box. As seen from excel spreadsheet and processed images, maximum axial displacement is observed on the upper central portion of the side wall.

Magnitude of shear band is considered to be directly proportional to axial displacements of soil particles measured on the transparent side. Shear band comparison among tests conducted at three different stages before pullout failure: nearest time at which LVDT 3 reached 1 mm, 2 mm, and 3 mm displacement.

4.2.1. Shear Band Comparison at LVDT 3 at 1 mm Displacement

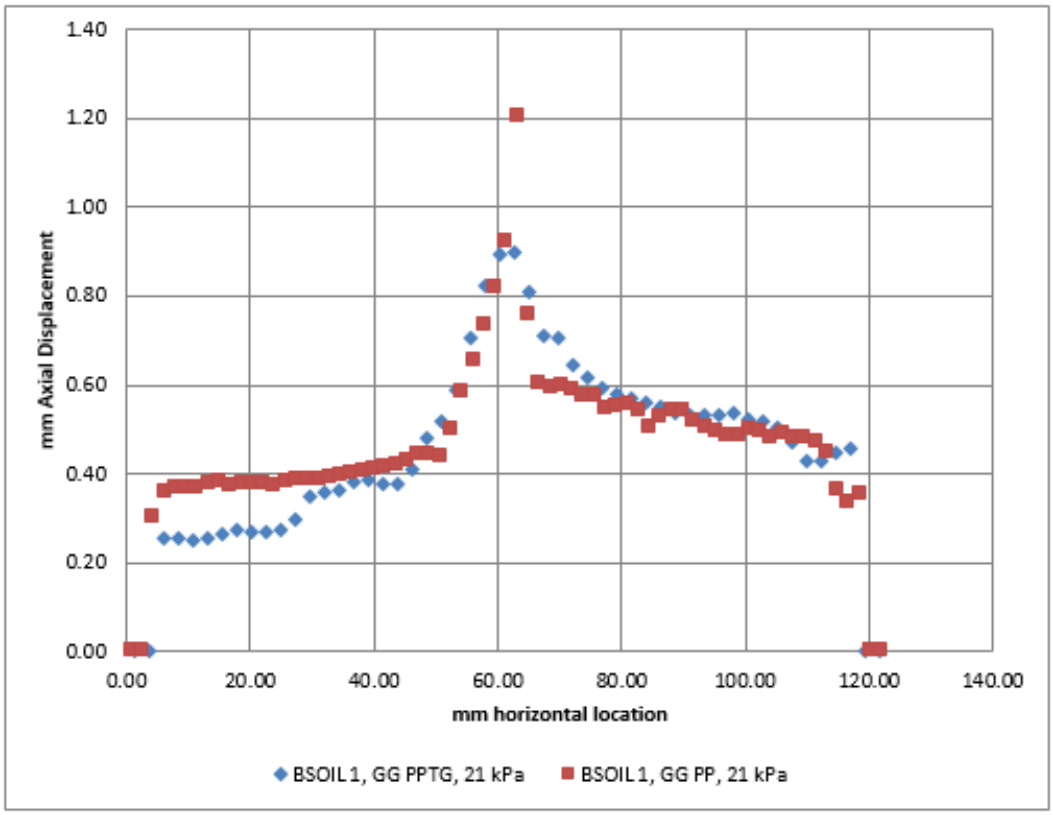

Figure 4.16. BSOIL 1- GG PP vs GG PPTG at 21kPa (Nominal).

As seen in Figure 4.16, shear band thickness is slightly larger for GG PP compared to GG PPTG mainly due to geometrical characteristics'. Wider and thicker ribs of GG PPTG contribute to a larger frictional surface area compared to GG PP in other words shear strength developed at GG PPTG is higher. Another reason is the distance between the neighboring ribs is closer for GG PPTG resulting with better confinement and interlocking. Those findings are in line with Fannin (1993), Bao (2006) and Ruiken (2012).

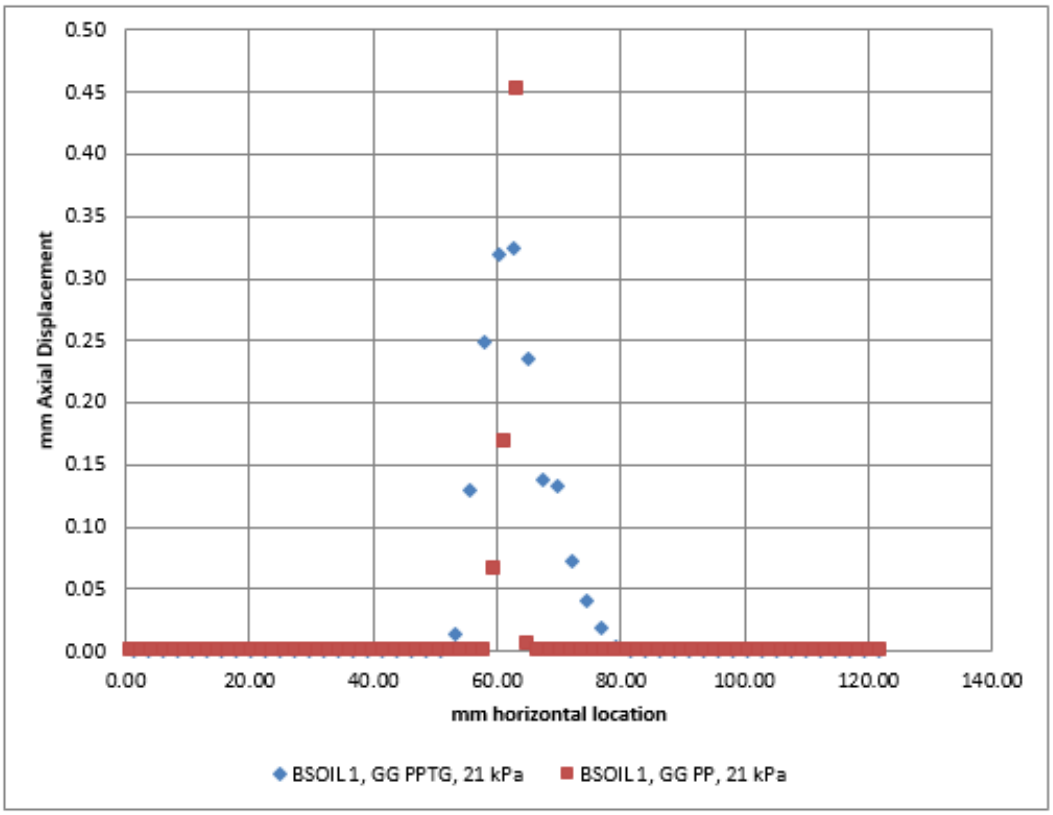

Figure 4.17. BSOIL 1- GG PP vs GG PPTG at 21kPa (Normalized).

Nominal axial displacement values are normalized, by mean value between maximum and minimum axial displacement to define boundaries of shear band, for further investigation. As seen in Figure 4.18, peak behavior observed with normalized values is in the similar manner with nominal axial displacement findings in Figure 4.17.

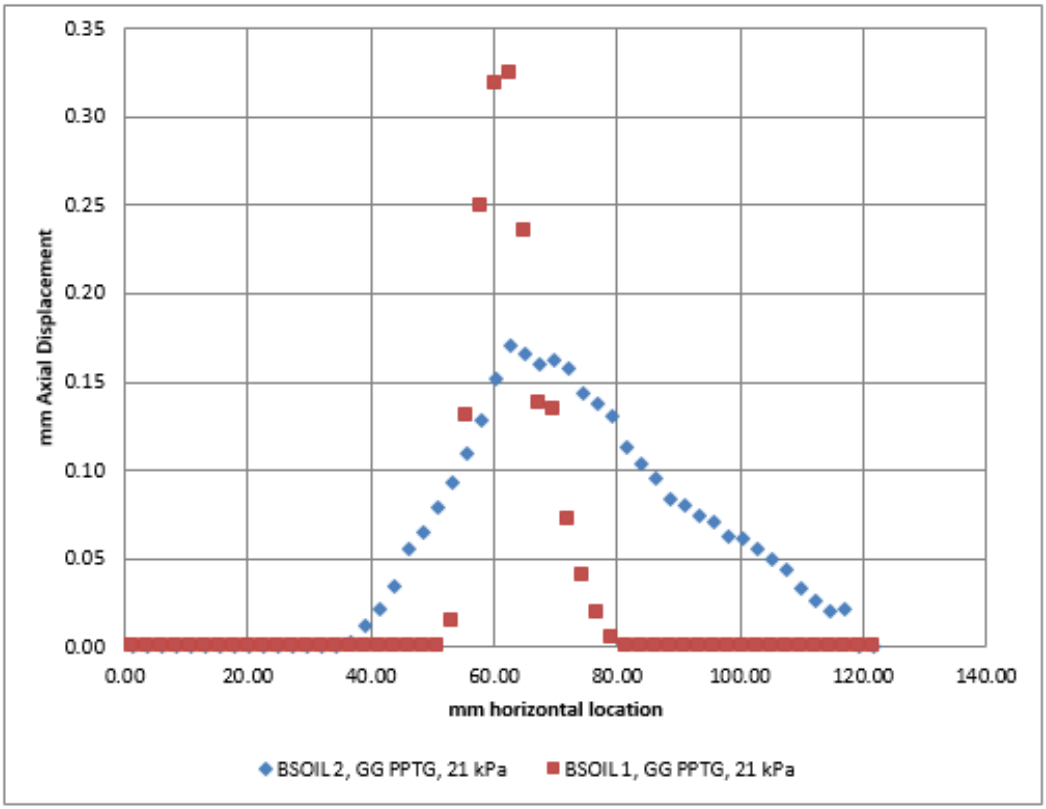

Figure 4.18. GG PPTG - BSOIL1 vs BSOIL2 at 21kPa (Normalized).

Nominal axial displacement values are normalized, by mean value between maximum and minimum axial displacement to define boundaries of shear band, for further investigation. As seen in Figure 4.18, peak behavior observed with normalized values is in the similar manner with nominal axial displacement findings in Figure 4.17.

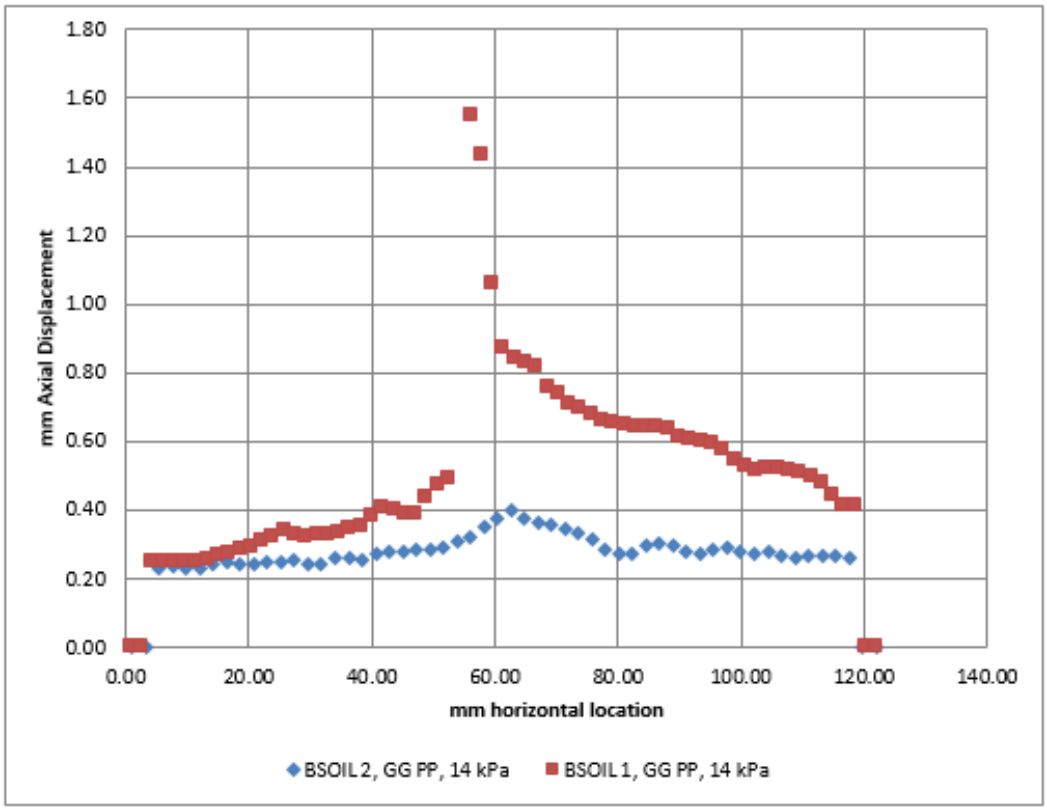

Figure 4.19. GG PP - BSOIL1 vs BSOIL2 at 14 kPa (Nominal).

Similar to findings with GG PPTG, as seen in Figure 4.19 Shear band thickness is larger for BSOIL 1 compared to BSOIL 2 due to particle size and geometry. Several studies have estimated the thickness of the shear band with particle size (d_{50}). Average particles size of BSOIL 1 is considerably higher that BSOIL 2, resulting with thicker shear band. Those findings are in line with Muhlhaus and Vardoulakis (1987), Bariether *et al.*, (2008).

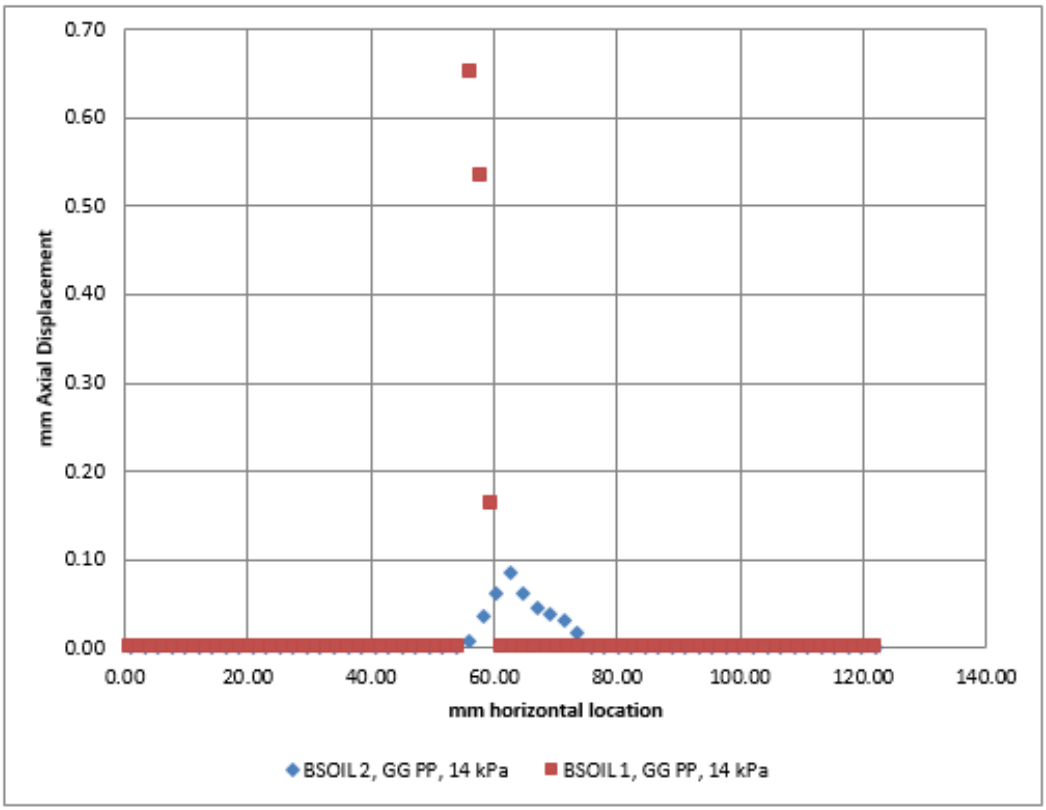

Figure 4.20. GG PP - BSOIL1 vs BSOIL2 at 14 kPa (Normalized).

Nominal axial displacement values are normalized, by mean value between maximum and minimum axial displacement to define boundaries of shear band, for further investigation. As seen in Figure 4.20, peak behavior observed with normalized values is in the similar manner with nominal axial displacement findings in Figure 4.19.

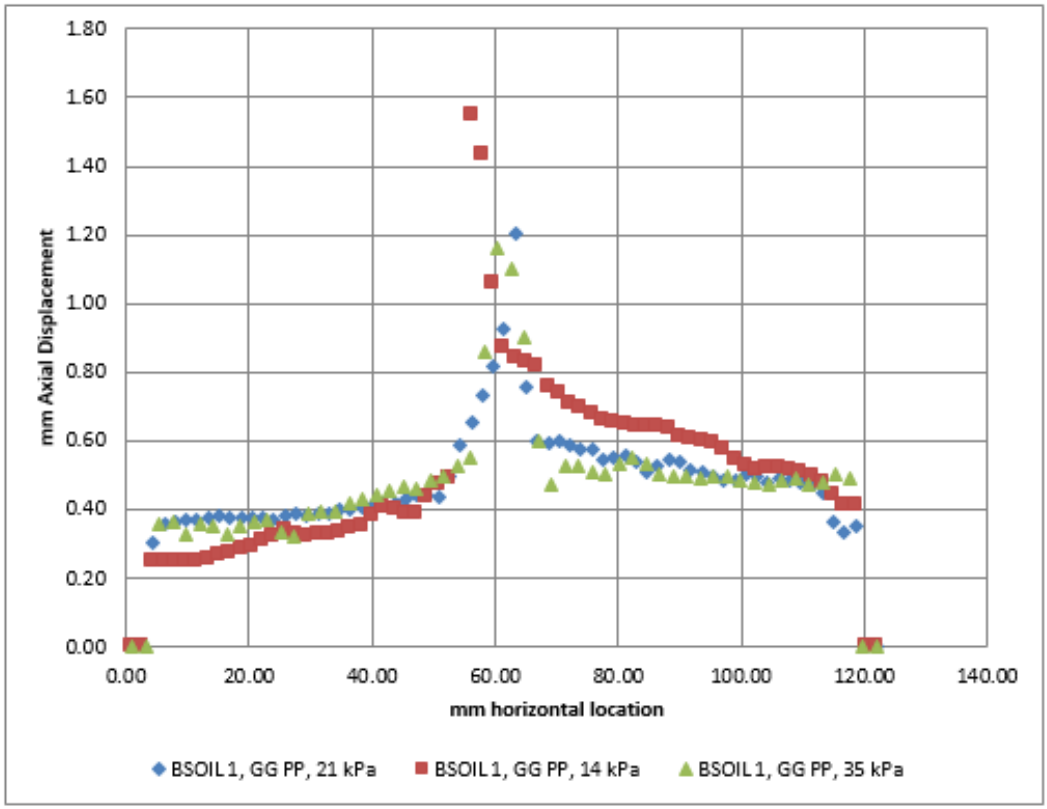

Figure 4.21. GG PP - BSOIL1 at 14, 21 and 35 kPa (Nominal).

As seen in Figure 4.2, shear band thickness is larger for lower overburden pressures in other words less confinement and less dilatant. Many studies have shown that the most significant factor affecting the shear band thickness is the dilatancy. Those findings are in line with restrained dilatancy concepts presented by Goilloux *et al.*, (1979), Alfaro *et al.*, (1995), Moraci and Gioffre (2006), Kitsabunnarat *et al.*, (2008), Ruiken *et al.*, (2011).

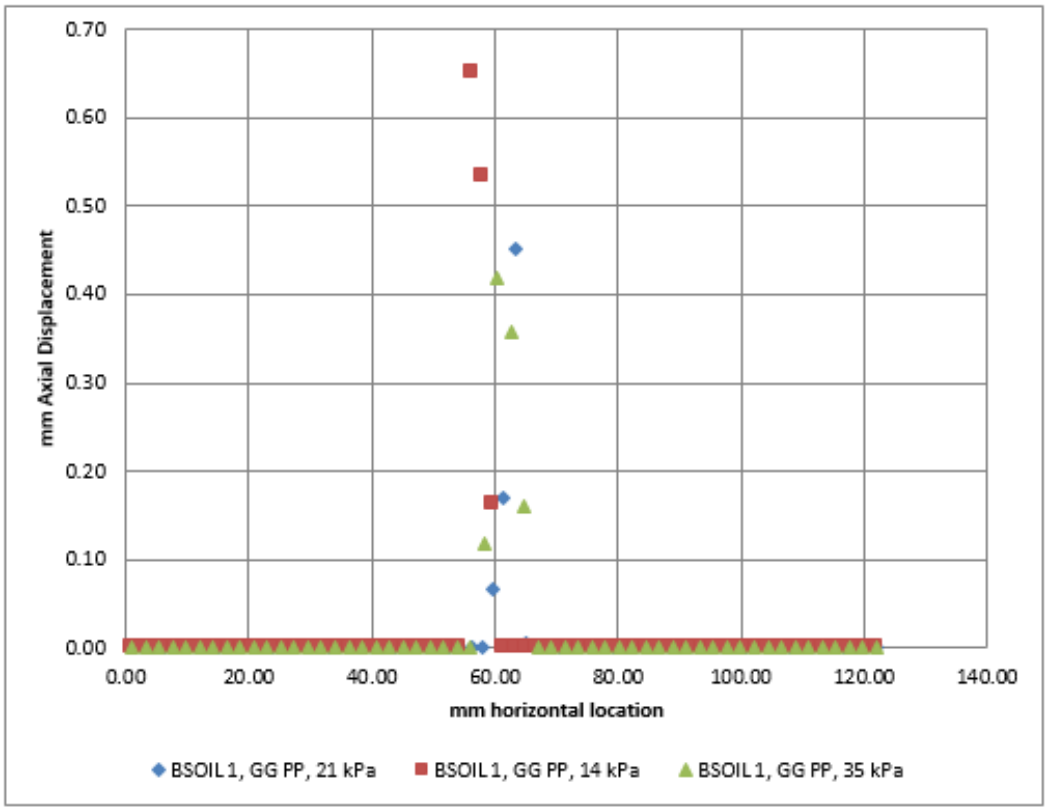

Figure 4.22. BSOIL1 at 14, 21 and 35 kPa (Normalized).

Nominal axial displacement values are normalized, by mean value between maximum and minimum axial displacement to define boundaries of shear band, for further investigation. As seen in Figure 4.22, peak behavior observed with normalized values is in the similar manner with nominal axial displacement findings in Figure 4.21.

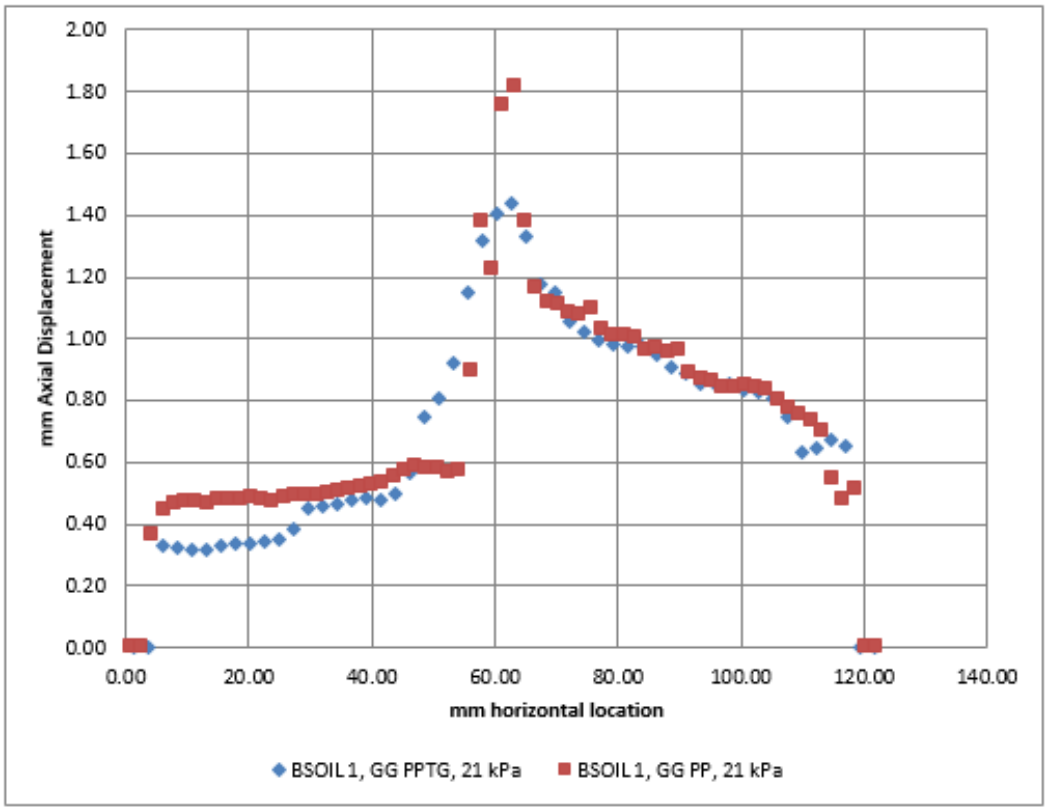

Figure 4.23. BSOIL 1- GG PP vs GG PPTG at 21kPa (Nominal).

As seen in Figure 4.23, shear band thickness is larger for GG PP compared to GG PPTG mainly due to geometrical characteristics'. Wider and thicker ribs of GG PPTG contribute to a larger frictional surface area compared to GG PP in other words shear strength developed at GG PPTG is higher. Another reason is the distance between the neighboring ribs is closer for GG PPTG resulting with better confinement and interlocking. Those findings are in line with Fannin (1993), Bao (2006) and Ruiken (2012).

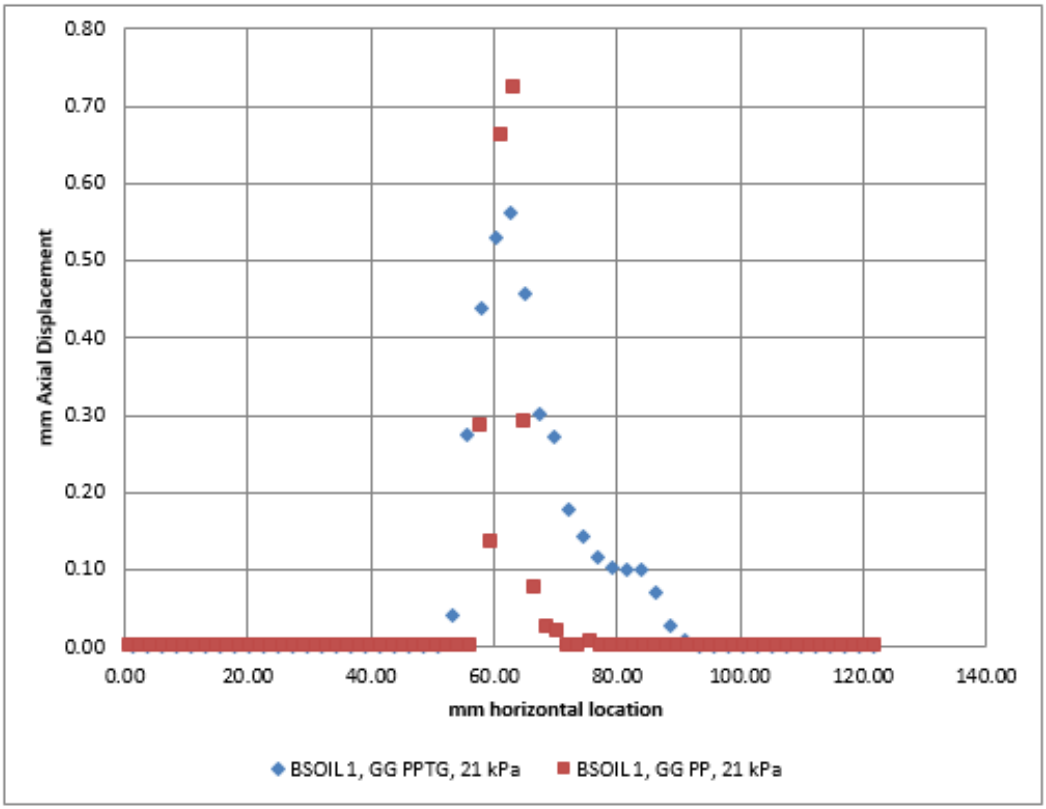

Figure 4.24. BSOIL 1- GG PP vs GG PPTG at 21kPa (Normalized).

Nominal axial displacement values are normalized, by mean value between maximum and minimum axial displacement to define boundaries of shear band, for further investigation. As seen in Figure 4.24, peak behavior observed with normalized values is in the similar manner with nominal axial displacement findings in Figure 4.23.

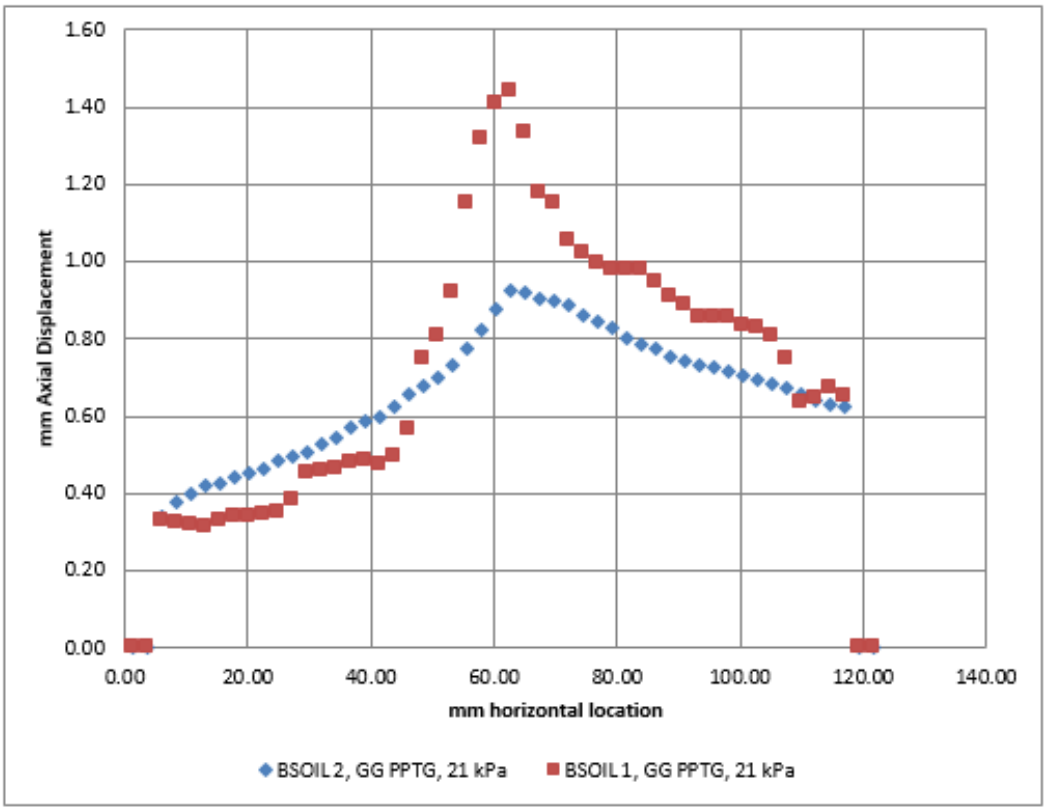

Figure 4.25. GG PPTG - BSOIL1 vs BSOIL2 at 21kPa (Nominal).

As seen in Figure 4.25, Shear band thickness is larger for BSOIL 1 compared to BSOIL 2 due to particle size and geometry. Several studies have estimated the thickness of the shear band with particle size (d_{50}). Average particles size of BSOIL 1 is considerably higher that BSOIL 2, resulting with thicker shear band. Those findings are in line with Muhlhaus and Vardoulakis (1987), Bariether *et al.*, (2008).

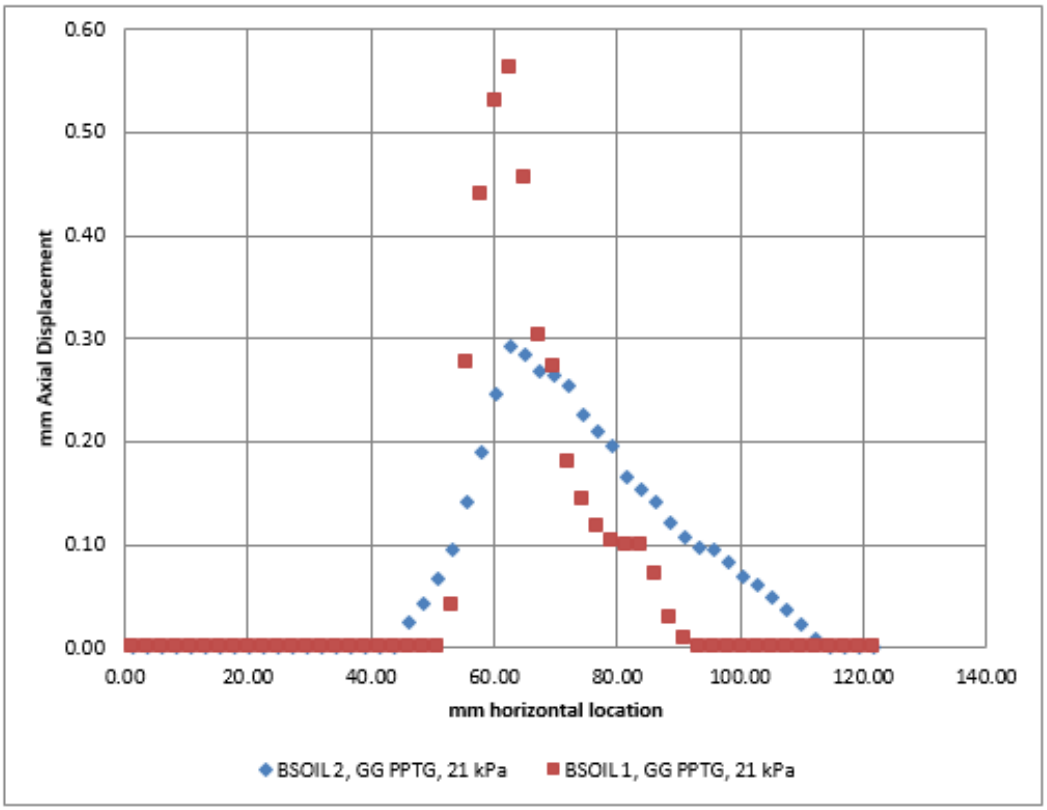

Figure 4.26. GG PPTG - BSOIL1 vs BSOIL2 at 21kPa (Nominal).

Nominal axial displacement values are normalized, by mean value between maximum and minimum axial displacement to define boundaries of shear band, for further investigation. As seen in Figure 4.26, peak behavior observed with normalized values is in the similar manner with nominal axial displacement findings in Figure 4.25.

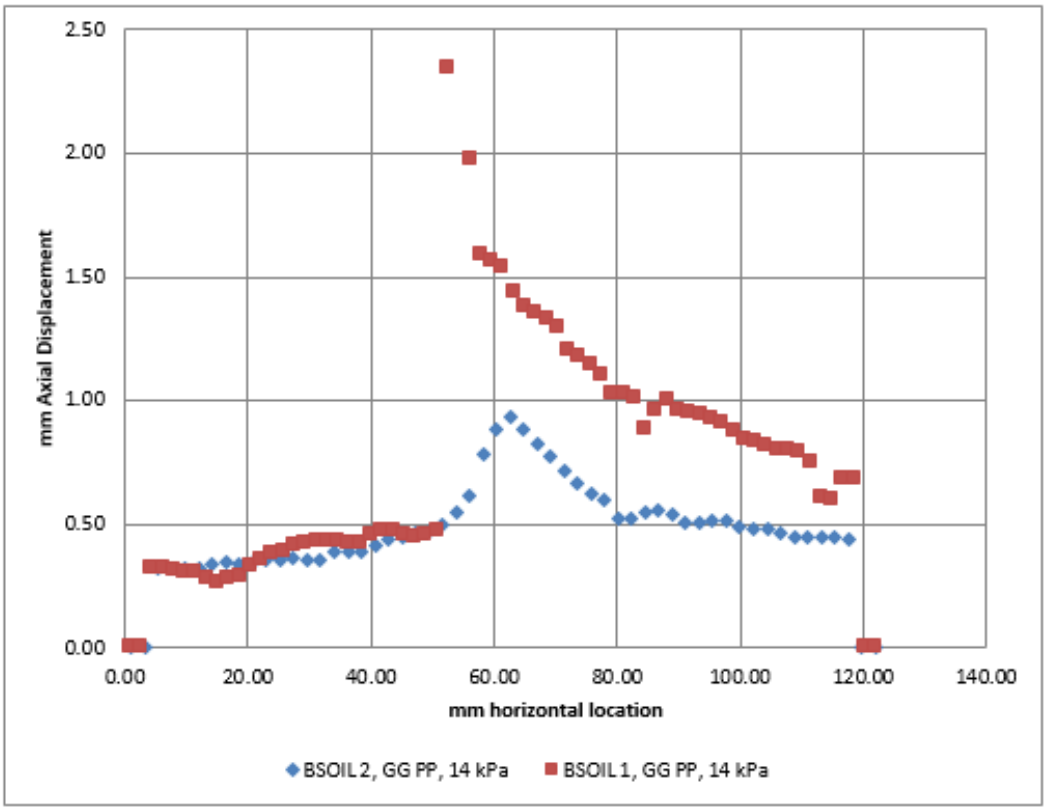

Figure 4.27. GG PP - BSOIL1 vs BSOIL2 at 14 kPa (Nominal).

Similar to findings with GG PPTG, as seen in Figure 4.27 shear band thickness is larger for BSOIL 1 compared to BSOIL 2 due to particle size and geometry. Several studies have estimated the thickness of the shear band with particle size (d_{50}). Average particles size of BSOIL 1 is considerably higher that BSOIL 2, resulting with thicker shear band. Those findings are in line with Muhlhaus and Vardoulakis (1987), Bariether *et al.*, (2008).

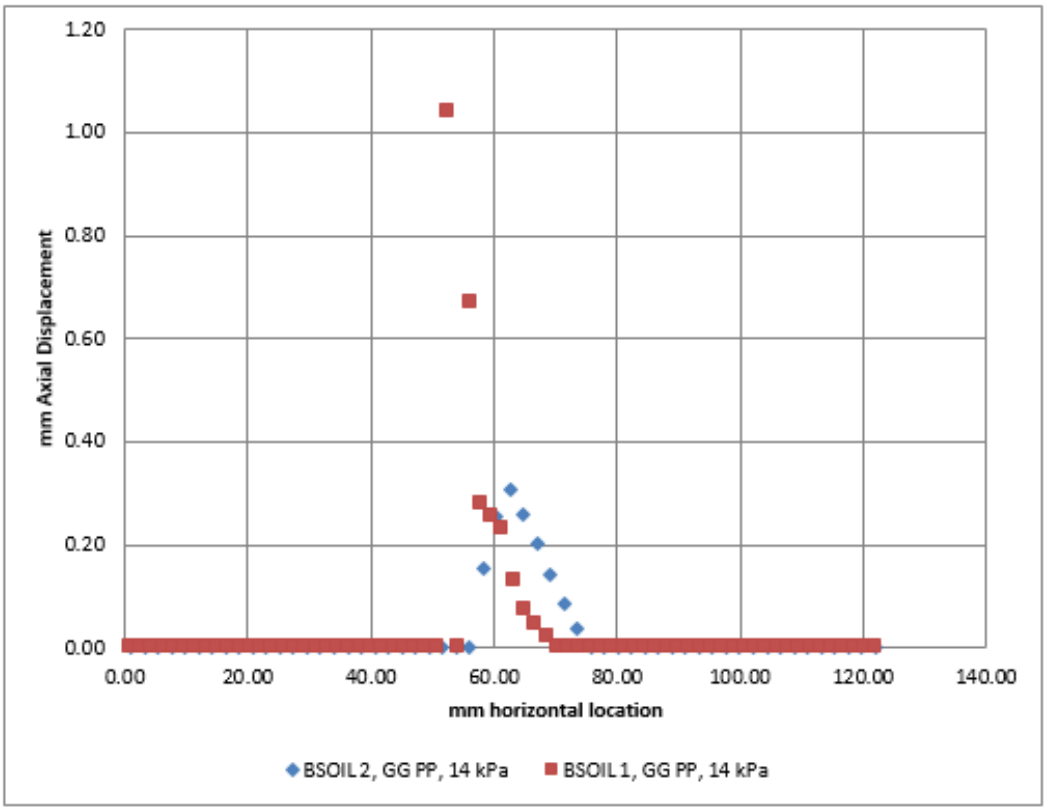

Figure 4.28. GG PP - BSOIL1 vs BSOIL2 at 14 kPa (Normalized).

Nominal axial displacement values are normalized, by mean value between maximum and minimum axial displacement to define boundaries of shear band, for further investigation. As seen in Figure 4.28, peak behavior observed with normalized values is in the similar manner with nominal axial displacement findings in Figure 4.27.

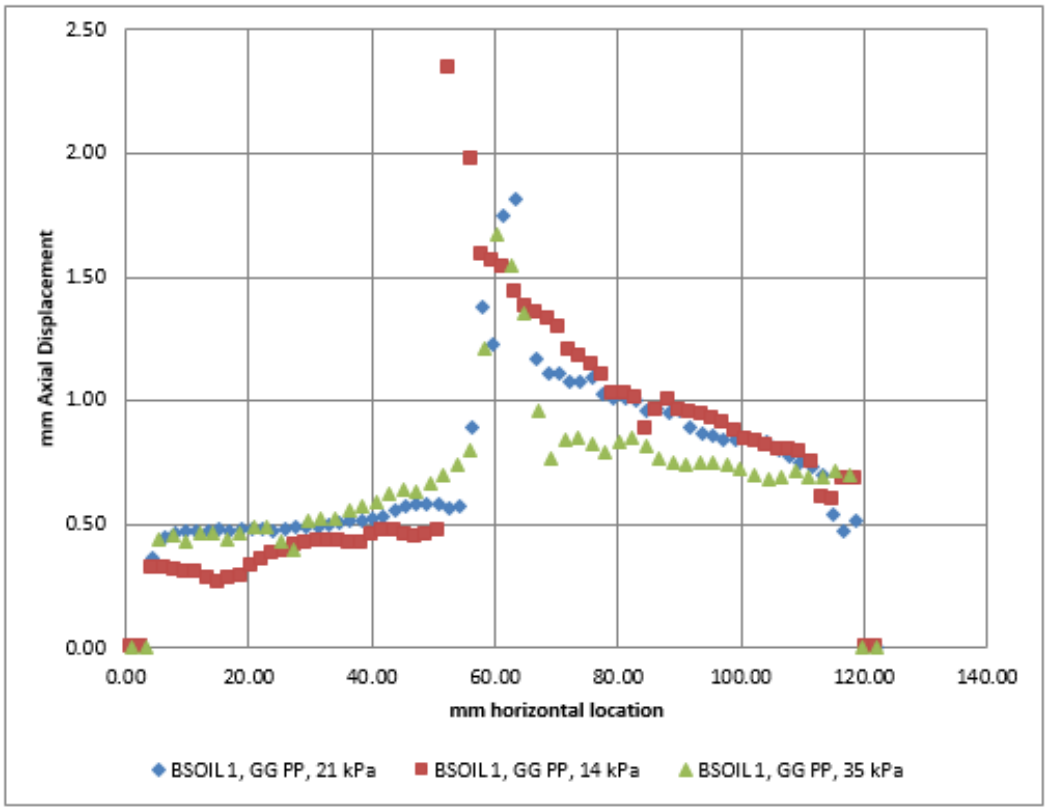

Figure 4.29. GG PP - BSOIL1 at 14, 21 and 35 kPa (Nominal).

As seen in Figure 4.29, shear band thickness is larger for lower overburden pressures in other words less confinement and less dilatant. Many studies have shown that the most significant factor affecting the shear band thickness is the dilatancy. Those findings are in line with restrained dilatancy concepts presented by Goilloux *et al.*, (1979), Alfaro *et al.*, (1995), Moraci and Gioffre (2006), Kitsabunnarat *et al.*, (2008), Ruiken *et al.*, (2011).

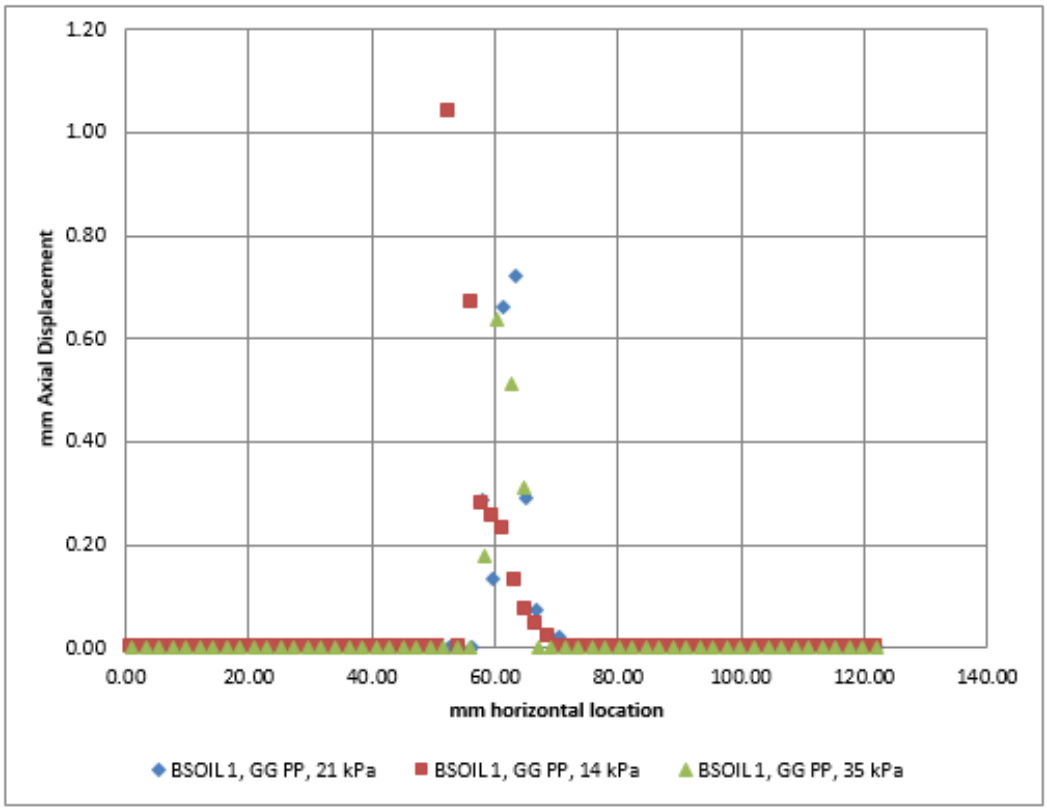

Figure 4.30. BSOIL1 at 14, 21 and 35 kPa (Normalized).

Nominal axial displacement values are normalized, by mean value between maximum and minimum axial displacement to define boundaries of shear band, for further investigation. As seen in Figure 4.30, peak behavior observed with normalized values is in the similar manner with nominal axial displacement findings in Figure 4.29.

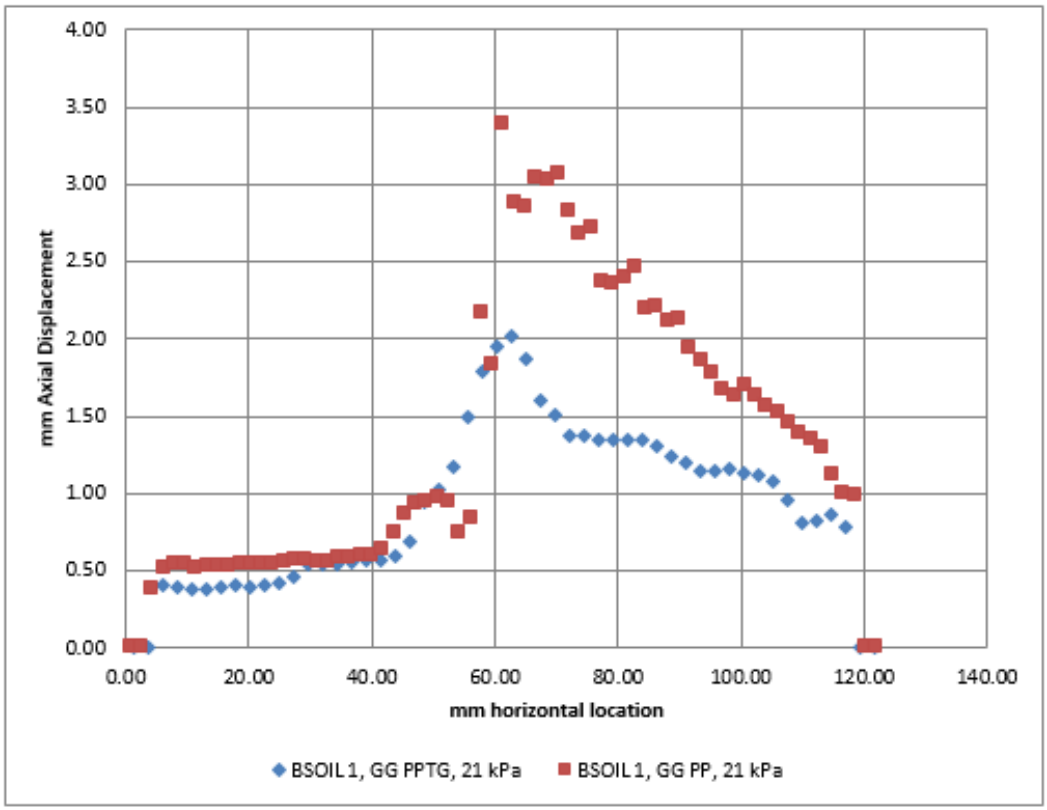

Figure 4.31. BSOIL 1- GG PP vs GG PPTG at 21kPa (Nominal).

As seen in Figure 4.31, shear band thickness is larger for GG PP compared to GG PPTG mainly due to geometrical characteristics'. Wider and thicker ribs of GG PPTG contribute to a larger frictional surface area compared to GG PP in other words shear strength developed at GG PPTG is higher. Another reason is the distance between the neighboring ribs is closer for GG PPTG resulting with better confinement and interlocking. Those findings are in line with Fannin (1993), Bao (2006) and Ruiken (2012).

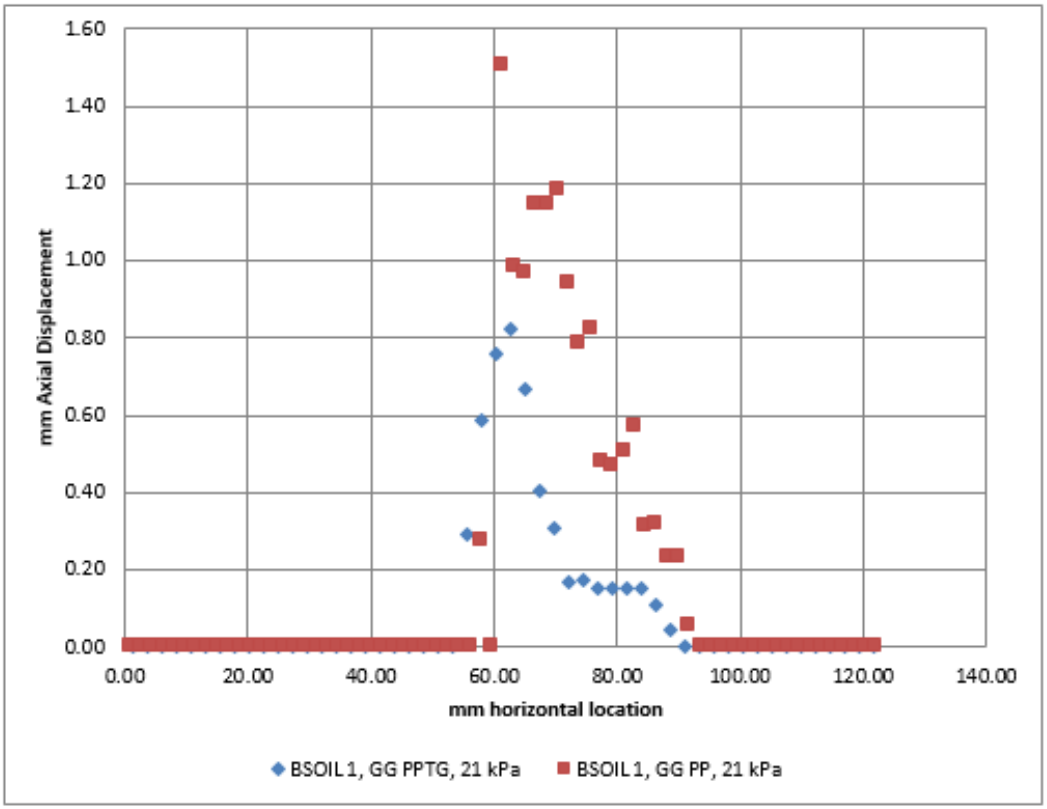

Figure 4.32. BSOIL 1- GG PP vs GG PPTG at 21kPa (Normalized).

Nominal axial displacement values are normalized, by mean value between maximum and minimum axial displacement to define boundaries of shear band, for further investigation. As seen in Figure 4.32, peak behavior observed with normalized values are in the similar manner with nominal axial displacement findings in Figure 4.31.

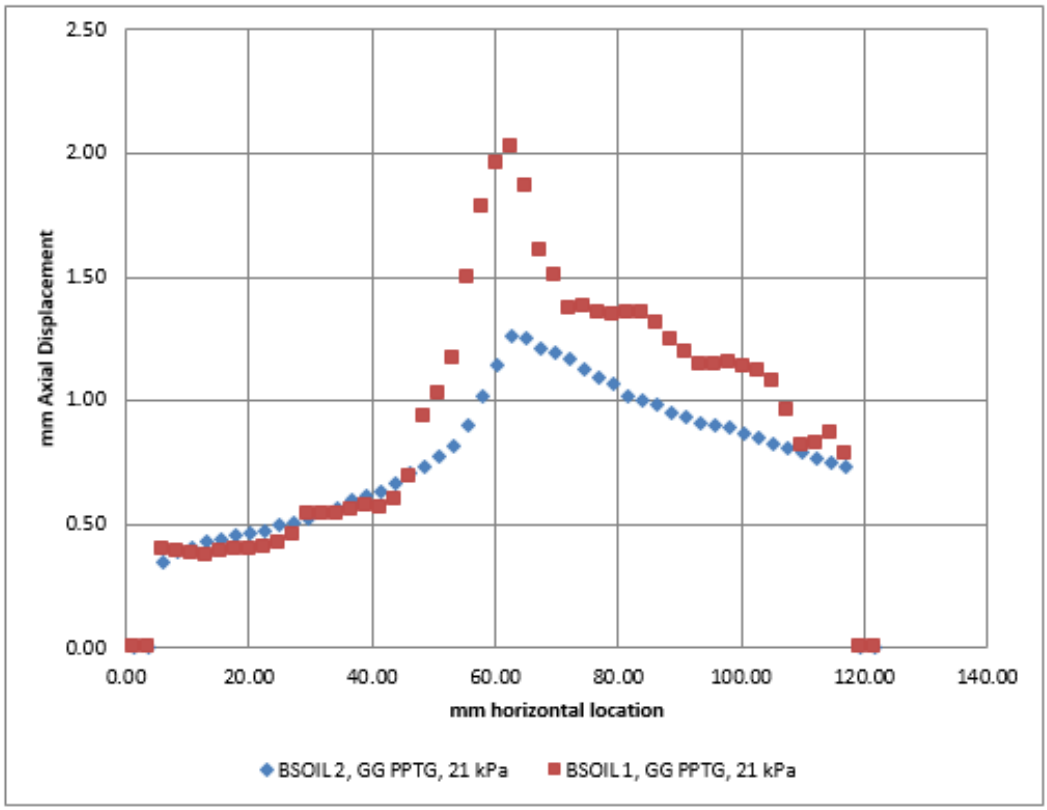

Figure 4.33. GG PPTG - BSOIL1 vs BSOIL2 at 21kPa (Nominal).

As seen in Figure 4.33, shear band thickness is larger for BSOIL 1 compared to BSOIL 2 due to particle size and geometry. Several studies have estimated the thickness of the shear band with particle size (d_{50}). Average particles size of BSOIL 1 is considerably higher that BSOIL 2, resulting with thicker shear band. Those findings are in line with Muhlhaus and Vardoulakis (1987), Bariether *et al.*, (2008).

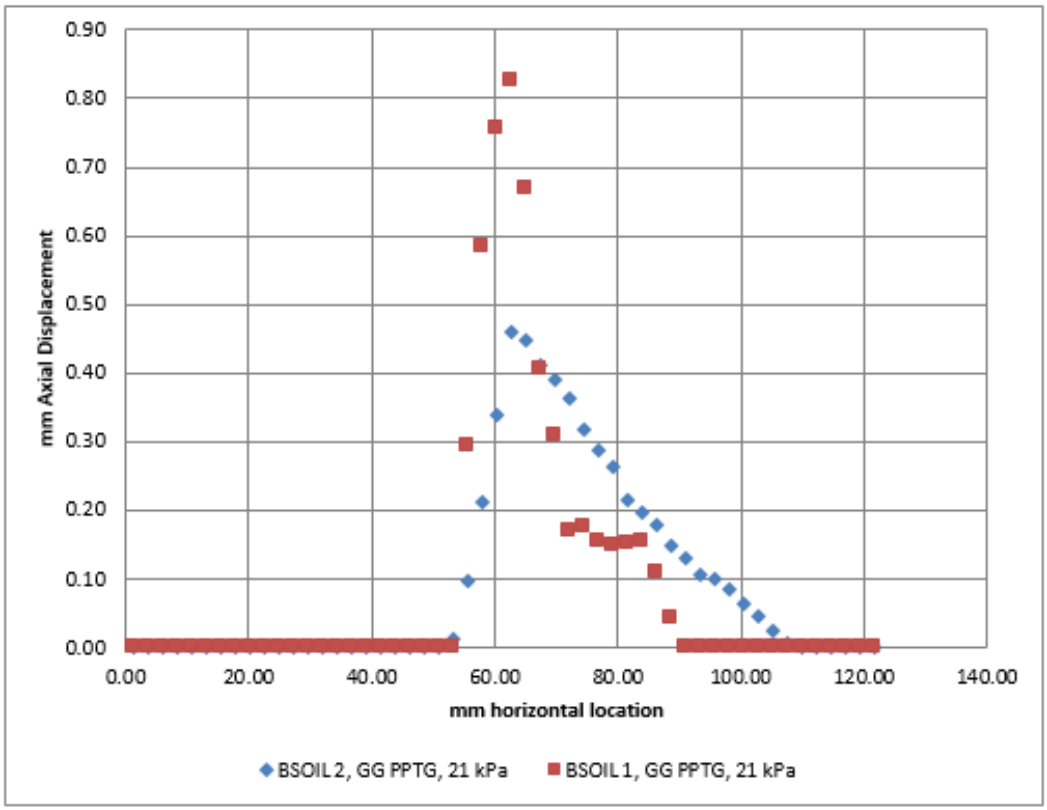

Figure 4.34. GG PPTG - BSOIL1 vs BSOIL2 at 21kPa (Normalized).

Nominal axial displacement values are normalized, by mean value between maximum and minimum axial displacement to define boundaries of shear band, for further investigation. As seen in Figure 4.34, peak behavior observed with normalized values is in the similar manner with nominal axial displacement findings in Figure 4.33.

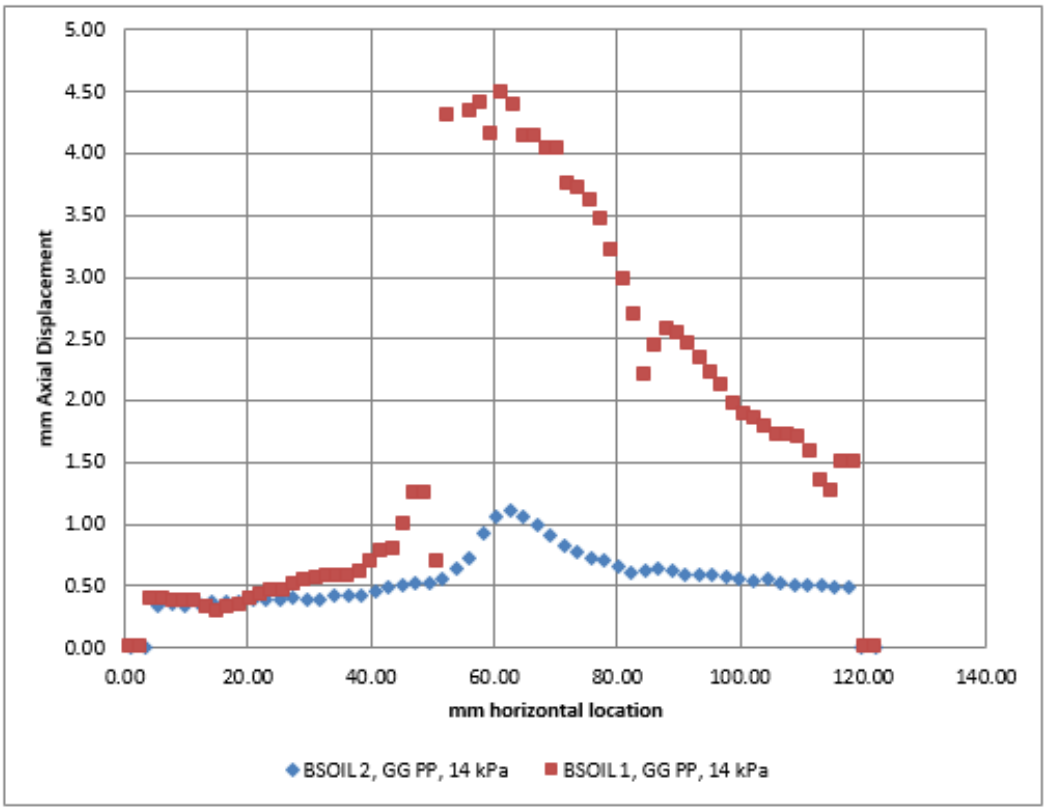

Figure 4.35. GG PP - BSOIL1 vs BSOIL2 at 14 kPa (Nominal).

Similar to findings with GG PPTG, as seen in Figure 4.35 shear band thickness is larger for BSOIL 1 compared to BSOIL 2 due to particle size and geometry. Several studies have estimated the thickness of the shear band with particle size (d_{50}). Average particles size of BSOIL 1 is considerably higher that BSOIL 2, resulting with thicker shear band. Those findings are in line with Muhlhaus and Vardoulakis (1987), Bariether *et al.*, (2008).

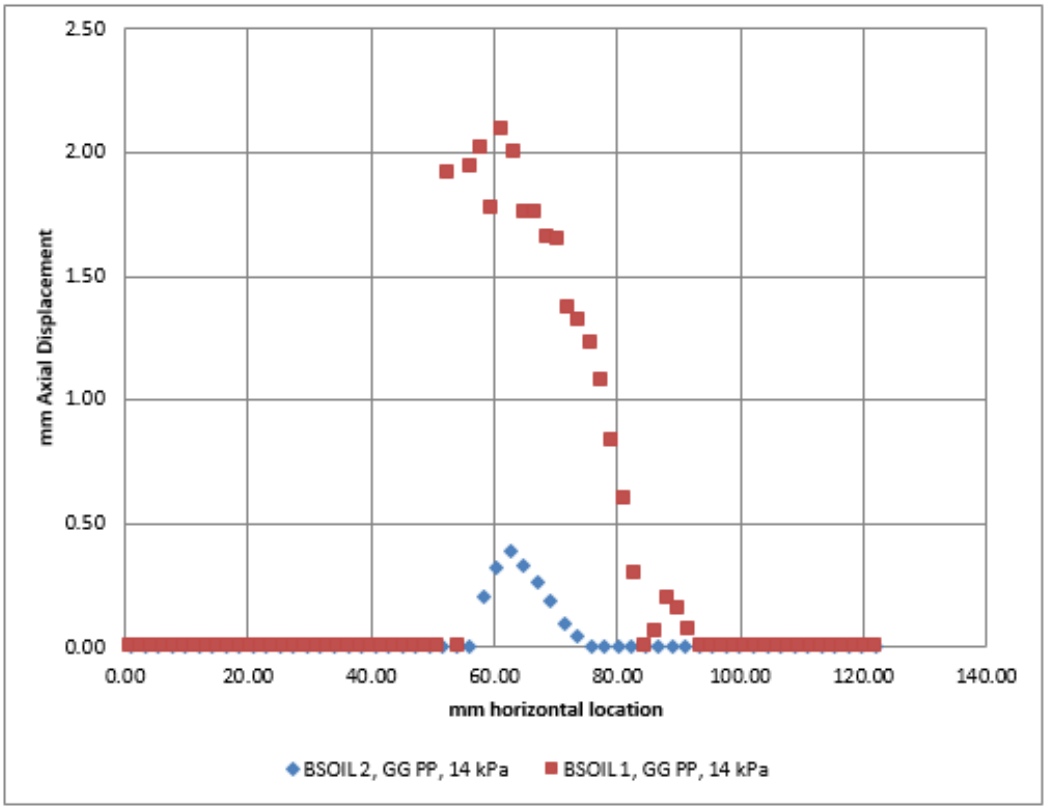

Figure 4.36. GG PP - BSOIL1 vs BSOIL2 at 14 kPa (Normalized).

Nominal axial displacement values are normalized, by mean value between maximum and minimum axial displacement to define boundaries of shear band, for further investigation. As seen in Figure 4.36, peak behavior observed with normalized values is in the similar manner with nominal axial displacement findings in Figure 4.35.

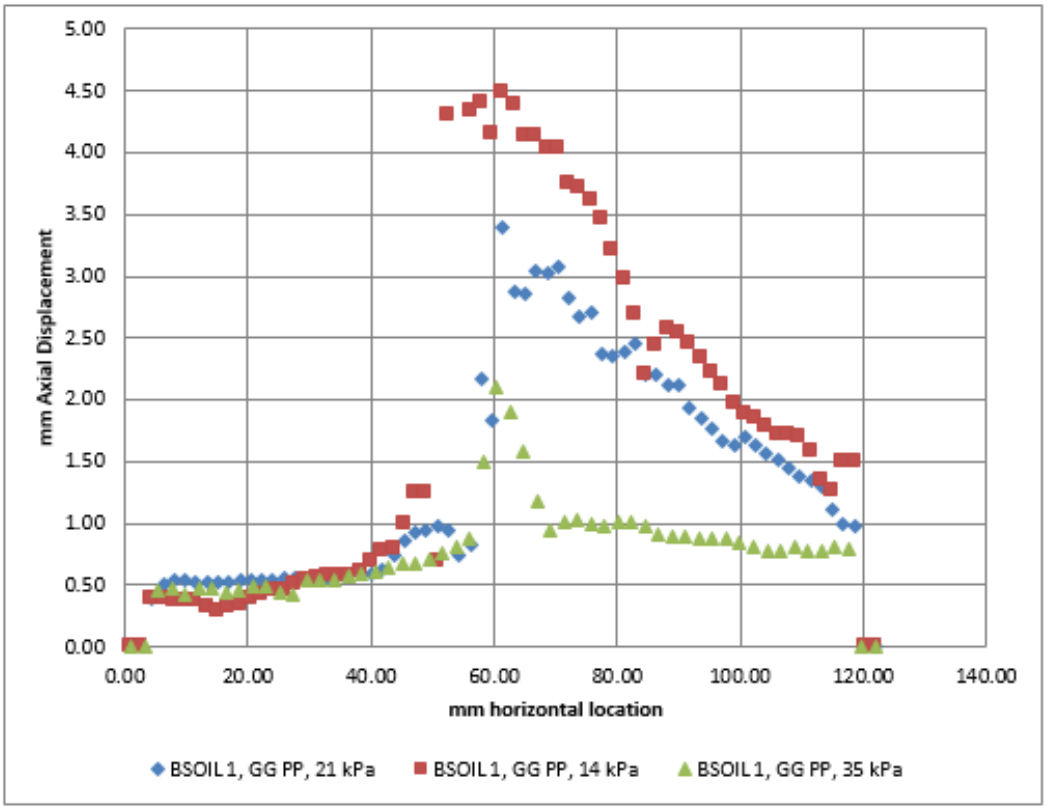

Figure 4.37. GG PP - BSOIL1 at 14, 21 and 35 kPa (Nominal).

As seen in Figure 4.37, shear band thickness is larger for lower overburden pressures in other words less confinement and less dilatant. Many studies have shown that the most significant factor affecting the shear band thickness is the dilatancy. Those findings are in line with restrained dilatancy concepts presented by Goilloux *et al.*, (1979), Alfaro *et al.*, (1995), Moraci and Gioffre (2006), Kitsabunnarat *et al.*, (2008), Ruiken *et al.*, (2011).

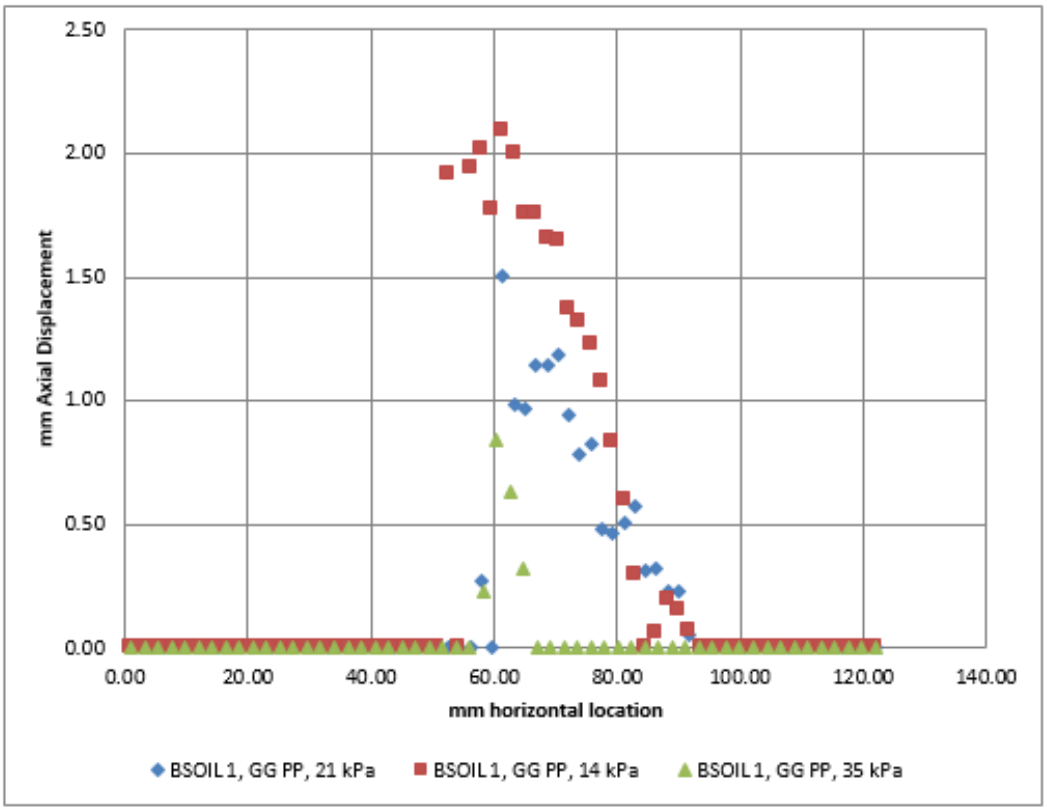

Figure 4.38. BSOIL1 at 14, 21 and 35 kPa (Normalized).

Nominal axial displacement values are normalized, by mean value between maximum and minimum axial displacement to define boundaries of shear band, for further investigation. As seen in Figure 4.38, peak behavior observed with normalized values is in the similar manner with nominal axial displacement findings in Figure 4.37.

5. CONCLUSIONS

GRS-IBS is a promising technology to reduce both cost and time of bridge construction. And its applications are in increase all around the world, especially in North America. Performance of existing GRS-IBS structures is still being observed to fully understand the complete behavior.

The objective of this study and experiments were the investigation of shear band mechanism under different conditions in geosynthetics reinforced soil; hence have a better understanding of the phenomena, especially for determination of reinforcement spacing. Complete coverage of serviceability and failure mechanisms of the reinforced soil leads to efficient guidelines for design and construction.

Experiments were run with modified small pull out box at the University of Texas at Austin. Displacements of the geogrid ribs at 5 different locations measured via LVDTs. In addition to LVDT measurements, axial displacements of the soil particles on transparent side were obtained using Digital Image Correlation technique.

Throughout the configuration of the modified test setup, many trials performed to optimize the setup and image acquisition. And, with the final configuration 6 tests run to investigate shear band mechanism and make comparison under different testing conditions. From literature review the main parameters that are affecting the thickness of the shear band are selected as: overburden pressure (confinement), soil type, and geosynthetics' geometry. Tests were run under different overburden pressures (14, 21, 35 kPa); different soil types,(BSOIL 1, BSOIL 2) and different geosynthetics (GG PP, GG PPTG).

Due to the size, shape and distinct color of the aggregate, image analysis could be done without addition of any colored markers or dye. In this research 0.15 mm latex membrane which is gridded 0.64 cm x 0.64 cm, greased on the transparent acrylic side of the box in order to get axial displacement values of the sand particles.

Magnitude of shear band is considered to be directly proportional to axial displacements of soil particles measured on the transparent side. Similar to Lesniewska *et al.*, (2012), average value of maximum and minimum axial displacement is selected as threshold to define boundaries of shear band. Normalized (thresholding applied) and nominal axial displacement values are investigated.

To make a fair comparison of shear band thickness among different tests, image analyses are compared at the time nearest to central LVDT (LVDT 3) reached three different pre-determined displacement values before pullout failure (1.00, 2.00 and 3.00 mm).

As compliant with the literature review (Goilloux *et al.*, 1979 , Alfaro *et al.*, 1995, Moraci and Gioffre, 2006, Kitsabunnarat *et al.*, 2008, Ruiken *et al.*,2011, Muhlhaus and Vardoulakis, 1987, Bariether *et al.*, 2008, Fannin, 1993, Bao, 2006, Ruiken, 2012, Zhou *et al.*, 2012) it is observed that:

- The lower the overburden pressure, the larger the thickness of the shear band for sieved aggregate.
- The larger the particle size of the soil (d_{50}), the larger the thickness of the shear band.
- The width and thickness of the ribs, affect the thickness of the shear band. The wider and thicker the ribs, the smaller the shear band thickness.

As the load reaches to pullout failure load, the distinction among shear bands among different tests becomes more obvious. Test results are appropriate to have a better understanding of the shear band mechanism and make qualitative analysis among tests.

Test results show that the axial displacement is always larger in the half of the box that is on the bladder side. Asymmetry of the displacement is caused by the rigidity difference between rear wall and front wall of the box. Front wall includes compressed air bladder which allows dilation whereas rear wall is steel and rigid. Particles do not

move symmetrically along the interface due to the different boundary conditions (Zhou *et al.*, 2012).

So, an improvement of the test setup might be the addition of the second bladder instead of the rigid steel wall. With the addition of the second bladder, it is very likely to get symmetrical axial displacement results.

Experimental results support that the modified small pull out test is reliable to investigate the shear band mechanism but in order to come up with accurate quantitative shear band thickness measurements, the larger box would be better to use.

REFERENCES

AASHTO M43, *Standard Specification for Sizes of Aggregate for Road and Bridge Construction*, American Association of State Highway and Transportation Officials, Washington, D.C., 2005.

Adams, M., J. Nicks, T. Stabile, J. Wu, W. Schlatter, and J. Hartmann, *Geosynthetic Reinforced Soil Integrated Bridge System Synthesis Report*, FHWA-HRT-11- 027, McLean, VA, 2011.

Alfrao, M.C., Miura, N., Bergado, D.T., "SoiI-Geogrid Reinforcement Interaction by Pullout and Direct Shear Tests", *Geotechnical Testing Journal*, Vol. 18, No 2, pp. 157-167, 1995.

Alshibli K.A., and S. Sture, "Sand Shear Band Thickness Measurements by Digital Imaging Techniques", *Journal of Computing in Civil Engineering (ASCE) 1999*, Vol. 2, No. 13, pp.103-109, 1999.

Archer, S., *Subgrade Improvement for Paved and Unpaved Surfaces Using Geogrids*, Contech Construction Products Inc. 2008.

ASTM Standard D 2487 - 11, *Standard Practice for Classification of Soils for Engineering Purposes (Unified Soil Classification System)*, ASTM International, West Conshohocken, PA, 2011.

ASTM Standard D 4439 - 15a, *Standard Terminology for Geosynthetics, ASTM International*, West Conshohocken, PA, 2015.

ASTM Standard D 6706 - 01, *Standard Test Method for Measuring Geosynthetic Pullout Resistance in Soil*, ASTM International, West Conshohocken, PA, 2013.

Bareither, C., T. Edil, C. Benson, and D. Mickelson, "Geological and Physical Factors.

Affecting the Friction Angle of Compacted Sands", *Journal of Geotechnical and Geoenvironmental Engineering*, Vol. 134, No. 10, pp. 1476-1489, 2008.

Bathurst, R.J., "Reinforced Soil Walls - Design and Construction", *The Bridge and Structural Engineer*, Vol. 44, No. 3, pp. 15-24, 2014.

Beckham, W.K., and W.H. Mills, "Cotton-Fabric Reinforced Roads", *Engineering News Record*, Vol. 1, pp. 453-455, 1935.

Berg, R.R., B.R. Christopher, and N.C. Samtani, *Design and Construction of Mechanically Stabilized Earth Walls and Reinforced Soil Slopes - Volume I*, FHWA-NHI-10-024, Washington D.C., 2009.

BS 8006-1:2010, *Code of Practice for Strengthened/Reinforced Soils and Other Fills*, British Standards Institution, London, 2010.

Coduto, D.P., *Foundation Design Principles and Practices 2nd edition*, Prentice Hall, Upper Saddle River, NJ, 2001.

Das, B.M., *Principles of Geotechnical Engineering 7^{th} Edition*, Cengage Learning, Stamford, CT, 2009.

Donkada, S., D. Menon, "Optimal Design of Reinforced Concrete Retaining Walls", *Indian Concrete Journal*, Vol. 86, No. 4, pp. 9-18, 2012.

EN 1997-1:2004, *Eurocode 7: Geotechnical design- Part 1: General Rules*, European Committee for Standardization, Brussels, 2004.

Fannin R.J., and D.M. Raju, "On the pullout resistance of geosynthetics", *Can. Geotech. J.*, No. 30, pp. 409-417, 1993.

Ferreira, J.A.Z., *Evaluation of Soil-Geogrid Interaction at Different Load Levels Using Pullout Tests and Transparent Soil*, Ph.D. dissertation, The University of Texas at Austin, 2013.

Giroud, J.P., "Geosynthetics in Dams: Two Decades of Experience", *Geotechnical Fabrics Report*, Vol. 10, No. 3, pp. 5, 1992.

Guilloux, A., F. Schlosser, and N.T. Long, *Etude Du Frottement Sable-Armature En Laboratoire*, International Conference on Soil Reinforcement, Paris, 1979.

Jewell, R. A., "Reinforcement bond capacity", *Geotechnique*, Vol. 40, No. 3, pp. 513-518, 1990.

Kitsabunnarat, A., M. Alsaleh, and S. Helwany, "Capturing strain localization in reinforced soils", *Acta Geotechnica*, Vol. 3, No. 3, pp. 175-190, 2008.

Koerner, R.M., *Designing With Geosynthetics, 6th Edition*, Xlibris Corporation, New Jersey, 2012.

Kramer, S.L., *Geotechnical Earthquake Engineering, Prentice Hall*, Upper Saddle River, NJ, 1996.

Lesniewska, D., Z. Mroz, "Limit equilibrium approach to study the evolution of shear band systems in soils", *Geotechnique*, Vol. 50, No. 5, pp. 521-536, 2000.

Lesniewska, D., M. Niedostatkiewicz, and J. Tejchman, "Experimental Study on Shear Localisation in Granular Materials within Combined Strain and Stress Field", *Strain*, Vol. 48, pp. 430-444, 2012.

Liu X., A. Papon, and H. Muhlhaus, "Numerical study of structural evolution in shear band", *Philosophical Magazine*, Vol. 92, No.28-30, pp. 3501-3519, 2012.

Lo, S. C., "Pullout Resistance of Polyester Straps at Low Overburden Stress", *Geosynthetics International*, Vol. 5, No. 4, pp. 18-30, 1998.

Moraci, N., and D. Gioffre, "A Simple Method to Evaluate the Pullout Resistance of Extruded Geogrids Embedded in A Compacted Granular Soil", *Geotextiles and Geomembranes*, Vol. 24, No. 2, pp 116-128, 2006.

Muhlhaus, H., and I. Vardoulakis, "The thickness of shear bands in granular materials", *Geotechnique*, Vol. 3, No. 37, pp. 271-283, 1987.

OECD, "Infrastructure Investment Indicator", 2016, https: //data.oecd.org/transport/infrastructure-investment.htm, accessed at December 2016.

Palmeira, E.M., "Soil-geosynthetic interaction: Modelling and analysis", *Geotextiles and Geomembranes*, Vol. 27, No. 5, pp. 368-390, 2009.

Palmeira, E.M. and G.W.E. Milligan, "Scale and other factors affecting the results of pull-out tests of grids buried in sand", *Geotechnique*, Vol. 39, No. 3, pp. 511-524, 1989.

Pardi, L., P.L. Bourdeau, and E. Recordon, "The use of X-Ray Technique in the Study of Soil-Reinforcement Interaction", *Rivista Italiana di Geotecnica*, Vol. 24, No. 3, pp 117-126, 1990.

Roodi, G.H., Analytical, "Experimental and Field Evaluations of Soil-Geosynthetic Interaction under Small Displacements", Ph.D. Thesis, Dissertation, The University of Texas at Austin, 2016.

Ruiken, A., and M. Ziegler, *Large Scale laboratory Element Testing of Geogrid Reinforced Soil*, GIGSA GeoAfrica 2009 Conference, Cape Town, 2009.

Ruiken, A., F. Jacobs, and M. Ziegler, *Large Scale Biaxial Compression Testing of Geogrid Reinforced Soil*, 5^{th} European Geosynthetics Congress, Valenci , 2012.

Ruiken, A., M. Ziegler, L. Vollmert, and S. Hohny, "Investigation of the Compound Behavior of Geogrid Reinforced Soil", 15^{th} European Conference on Soil Mechanics and Geotechnical Engineering, Amsterdam, 2011.

Senn, M., C. Eberl, "Digital Image Correlation and Tracking", http://www.mathworks.com/matlabcentral/fileexchange / 50994-digital-image-correlation- and- tracking?

requestedDomain = www.mathworks.com & requestedDomain =www. mathworks. com, accessed at March 2016.

Shukla, S.K., J.H., Yin, *Fundamentals of Geosynthetic Engineering*, Taylor and Francis/Balkema, Leiden, 2006.

SCDOT *South Carolina Department of Transportation* (SCDOT, SCDOT Geotechnical Design Manual, SCDOT, Columbia, SC), 2010.

Staff, C.E., "The Foundation and Frowth of the Geomembrane Industry in the United States", *Proceedings of the International Conference on Geomembranes*, Denver, Vol. 1, pp. 5-8, 1984.

Sugimoto, M., A.M.N. Alagiyawanna, and K. Kadoguchi, "Influence of rigid and flexible face on geogrid pullout tests", *Geotextiles and Geomembranes*, Vol. 19, No. 5, pp. 257-277, 2001.

Tang, Z.Z., J. Liang, C. Guo, and Y.X. Wang, "Photogrammetry-Based Two-Dimensional Digital Image Correlation with Nonperpendicular Camera Alignment", *Optical Engineering*, Vol. 1, No. 51, pp. 2, 2012.

Tatsuoka, F., D. Hirakawa, M. Nojiri, H. Aizawa, H. Nishikiori, R. Soma, M. Tateyama, and K. Watanabe, "A New Type of Integral Bridge Comprising Geosynthetic-Reinforced Soil Walls", *Geosynthetics International*, Vol. 16, No. 4, pp. 301-326, 2010.

White, D.J., W.A. Take, and M.D. Bolton, "Particle Image Velocimetry (PIV) Software for Use In Geotechnical Testing", *Geotechnique*, Vol. 53, No. 7, pp 619-631, 2003.

Wolf H., D. Konig, and T. Triantafylldis, "The Influence of the Stress-Strain Behavior of Non-Cohesive Soils on the Geometry of Shear Band Systems under Extensional Strain", *Engineering Structures*, No. 28, pp 1760-1773, 2005.

Wu, J.T.H., and P.S.K. Ooi, *Synthesis of Geosynthetic Reinforced Soil (GRS) Design Topics*, FHWA-HRT-14- 094, McLean, VA, 2015.

Zhou J., J.F. Chen, and J.F. Xue, "Micro-Mechanism of the Interaction Between Sand and Geogrid Transverse Ribs", *Wang Geosynthetics International*, Vol. 1, pp. 6, 2012.

Zornberg, J.G., J.A.Z. Ferreira, and G.H. Roodi, "Geosynthetic-Reinforced Unbound Base Courses: Quantification of the Reinforcement Benefits", *Center for Transportation Research (CTR), FHWA/TX*, Vol. 10, No. 5, pp. 4829, 2013.

Zornberg, J.G., J.A.Z. Ferreira, R. Gupta, R.V. Joshi, and G.H. Roodi, "Geosynthetic-Reinforced Unbound Base Courses: Quantification of the Reinforcement Benefits", *Center for Transportation Research (CTR)*, Vol. 10, No. 5, pp. 4829, 2012.